CONTROLS ON MID-CRETACEOUS MARINE SEDIMENTATION IN THE TARFAYA BASIN, SOUTHERN MOROCCO

by

KATE RAVILIOUS

A thesis presented for the degree of
Doctor of Philosophy of the University of London

Department of Geological Sciences
University College London
Gower Street
London
WC1E 6BT
United Kingdom

AUGUST 2002

ProQuest LLC
789 East Eisenhower Parkway
P.O. Box 1346
Ann Arbor, MI 48106-1346

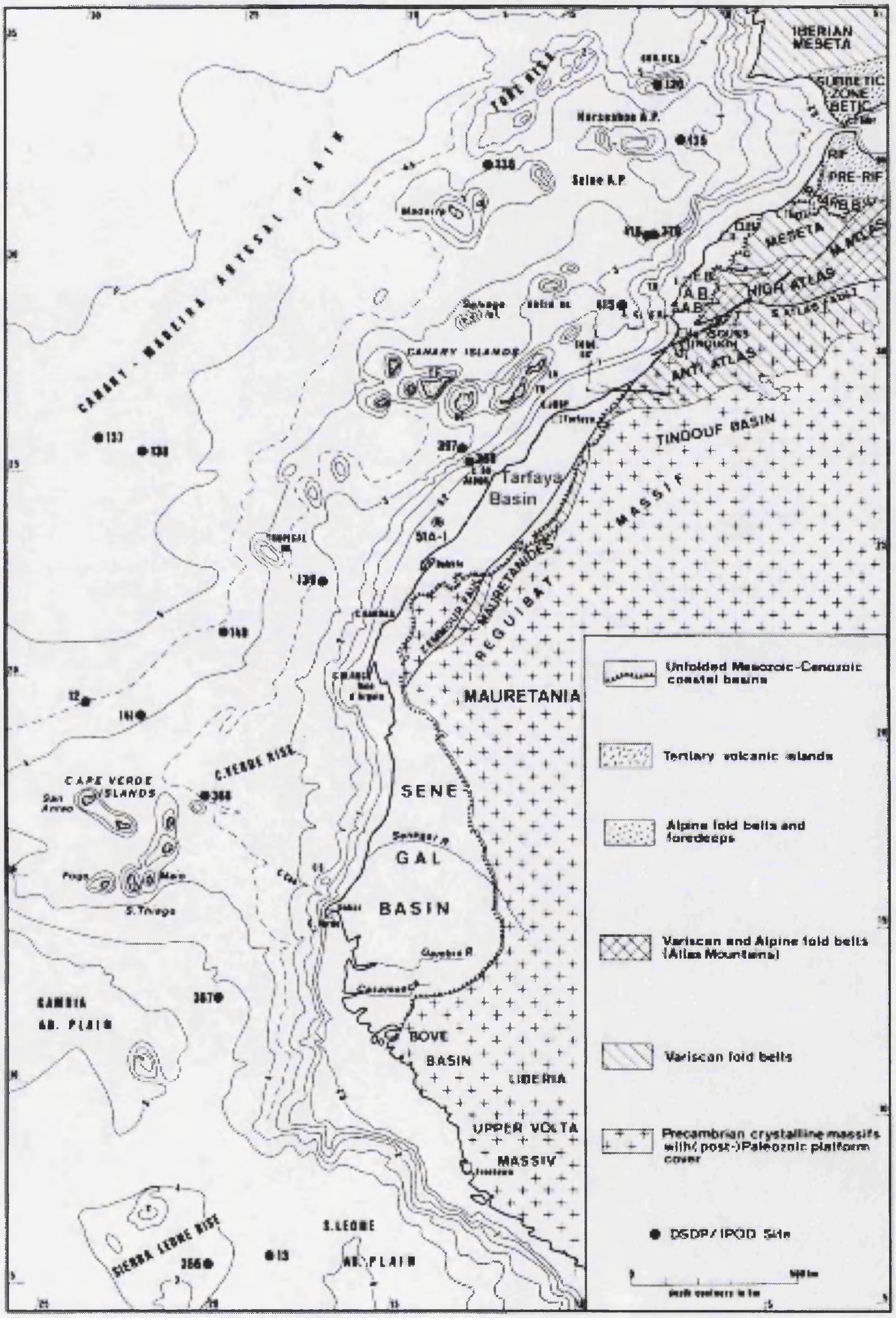

Figure 1: Geological sketch map of Northwest Africa and its continental margin. Indicates the location of the Tarfaya Basin, a marginal basin on the NW African craton, which preserves a record of Mesozoic upwelling conditions, analogous to those of the modern NW African shelf. Modified after Von Rad *et al* (1982)[185] and Luderer (1999) [105].

Abstract

Cenomanian marine sedimentation has been studied in sediments from the Tarfaya Basin, Southern Morocco. A continuous section of just under ten metres in length, composed from overlapping slabs of limestone, was cut from a disused quarry near the town of Tarfaya. Cutting and polishing the rock and then scanning it provided a digital record of sediment colour variation. Carbonate, organic carbon and calcareous nannofossils were studied at intervals throughout the section. Time series analysis was carried out on the sediment colour data but revealed no significant cyclicity at the sub-Milankovitch time scale. Combined results from variations in sediment colour, carbonate, organic carbon and calcareous nannofossils hint at the existence of different productivity regimes. Two productivity regimes are interpreted to alternate on a Milankovitch time scale. Regime 1 is characterised by extreme productivity induced by very strong upwelling conditions. It is characterised by dark coloured sediment, a high percentage of organic carbon, low nannofossil diversity and an abundance of the species *Eprolithus floralis.* Regime 2 is characterised by a less extreme environment and provides evidence for moderate to high productivity under coastal upwelling conditions. It is characterised by light coloured sediment, a lower percentage of organic carbon and a more diverse nannofossil assemblage. In particular *Sollasites horticus* and *Tranolithus* spp. become important, while *E. floralis* decreases in abundance. The change in intensity of oceanic upwelling required to produce these two different productivity regimes is likely to have been controlled by the strength of the trade winds. Few places in the world exhibit such extreme upwelling conditions today. One possible explanation is that the trade wind intensity during the Cenomanian greenhouse conditions was much stronger than Holocene trade winds and that these sediments were deposited during a climatic extreme.

Acknowledgements

I would like to thank the following people. First my supervisor Jürgen Thurow for coming up with the project and providing me with so many kilos of rocks! To Paul Bown for his patience in reading innumerable drafts of this thesis and improving it greatly, and for his support and guidance whilst carrying out the research. I also greatly appreciated the discussions I have had with Sandra Nederbragt, Chris Street, Graham Weedon and Carl Wunsch.

Thanks to Jim Davy for help with nannofossil preparations and unravelling the mysteries of how to use the SEM, Sean Houlding and Arthur Beer for rock cutting advice and thin section preparation, Tony Osbourn and the Wolfson Laboratory for Environmental Geochemistry for geochemical preparations and Toby Stiles for all things photographic.

To all my friends and family for keeping me sane and providing alternative perspectives on life, and to members of Imperial College Outdoor Club for helping me escape from London from time to time!

A special thanks to my partner, Jamie Wood, for being patient and giving me encouragement and confidence all along.

I wish to acknowledge the financial support received from the Natural Environment Research Council.

I am grateful to Nigel Lawrence for the style file for this thesis.

Table of contents

List of Figures

List of Tables

1

Introduction

The mid-Cretaceous represents an interesting time period from a geological point of view. The Earth experienced a *greenhouse* climate with very high levels of atmospheric carbon dioxide (as much as 3 to 12 times modern pre-industrial levels) [18], and a general absence of ice at the poles. Ocean surface waters were warm [194], and it was a period of intense oceanic volcanism [85]. Sea levels were extremely high; probably encouraged by the warm temperatures and the decrease in volume of oceanic basin due to volcanism and sea floor spreading [97]. Many parts of the world ocean experienced deposition of sediments anomalously rich in organic carbon. These periods of sequestration of organic carbon are termed *oceanic anoxic events* (OEA) and there are three such events during the mid Cretaceous (see section 2.7.3). They occur from the late Barremian through Albian, late Cenomanian through early Turonian and Conacian through Santonian [78].

The Cenomanian/Turonian (C/T) OAE occurred around 93 million years ago and is the most extensive of the mid-Cretaceous OAEs. It is characterised by an extreme positive global carbon isotope anomaly in both carbonate and organic matter, probably due to an increase in burial of organic matter in black shales [5]. In addition a significant extinction event occurred around the Cenomanian/Turonian (C/T) boundary, which was particulary severe for deep dwelling marine organisms [24].

The geological processes that brought about these enormous differences from today's world are still poorly understood, despite extensive research in this area.

In particular the cause of OAEs has still not been resolved and there are a number of competing hypotheses (explained in detail in section 2.7.3). Understanding the mechanisms and driving forces behind a *greenhouse* climate are pertinent to predicting and managing climate in the future on Earth. Increases in anthropogenic carbon dioxide emissions could lead to a global warming situation, changing our present *ice house* climate into a *greenhouse* one. The mid-Cretaceous, in particular the C/T, represents a natural climatic experiment in Earth history that may provide key information on the functioning of the global biogeochemical cycles and possible feedback mechanisms during a *greenhouse* climate.

The aim of this research was to investigate high frequency climate variability (sub-Milankovitch) during a *greenhouse* mode climate system.

1.1 Background and rationale

The Northwest African Atlantic margin is thought to have been especially sensitive to climatically driven fluctuations in marine productivity, and numerical circulation models predict unusually high mid-Cretaceous coastal upwelling intensities [89]. Close to the northern edge of this potential upwelling zone is the Tarfaya Basin (Morocco), which contains an exceptional, expanded sedimentary succession of C/T age. Figure 1 shows the location of the Tarfaya Basin. This 200m thick sequence is composed of laminated sediments, of at least decadal resolution, which were deposited in a high productivity, open marine, but anoxic basin. Individual lamina couplets consist of a simple alternation between well preserved coccoliths (light) and organic carbon (dark) (see figure 1.1). Sediments deposited within this oxygen minimum zone were largely protected from bioturbation and thus provide ideal records of past oceanic and associated climate signals.

Previous research carried out on Tarfaya Basin sediments has shown that the basin was influenced by Milankovitch cyclicity during the mid-Cretaceous (see section 2.4). Time control in the Tarfaya C/T sediment is provided by a strong obliquity cycle throughout.

During a previous field campaign in spring 1997, Jürgen Thurow sampled the material necessary for this study. Using a concrete saw he cut overlapping slabs of rock from a disused quarry (cut for oil prospecting purposes). Figure

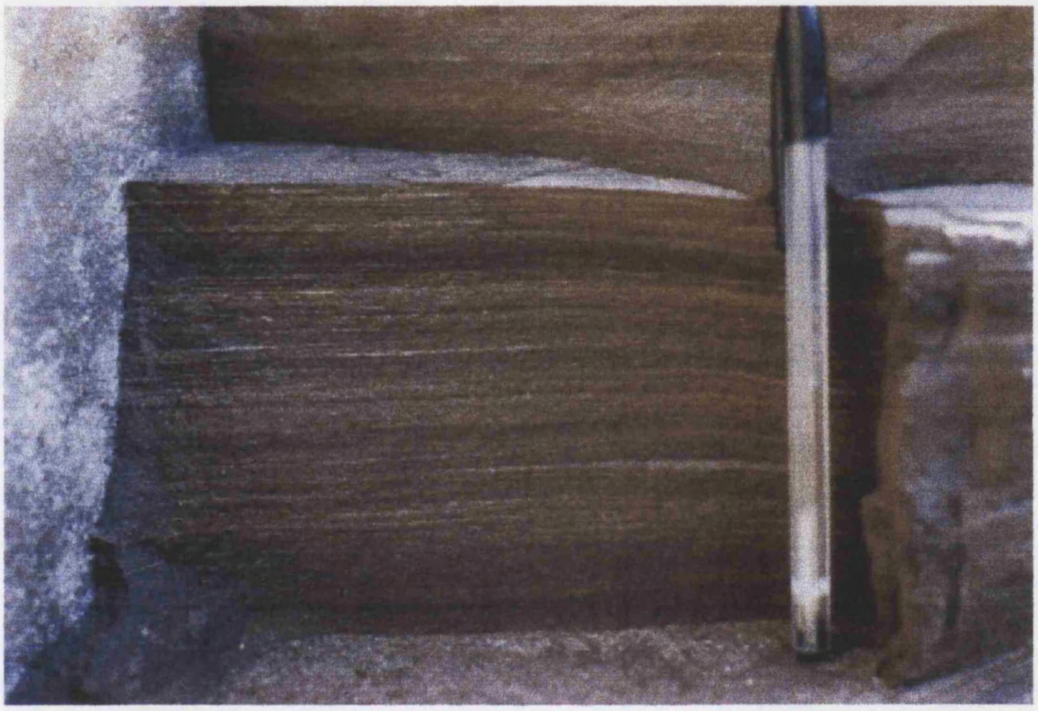

Figure 1.1: Photo of the laminations in the Tarfaya sediment, a pen provides the scale.

2.1 shows the location of the quarry within the Tarfaya Basin. Although the lower levels of the quarry are now flooded with sea water, it was still possible to sample approximately ten metres of rock from above this level. Figure 2.5 is a photograph of one of the quarry walls. A gently sloping path leads down into the quarry and this allowed access to the entire cliff face from sea level upwards. Nodular concretions were avoided in the sampling as they tend to disrupt the laminations. The facies succession is described fully in section 2.1.3. Figure 1.2 is a photo of one of the slabs that was cut from the quarry.

The sample interval for this study was chosen because it was relatively easy to access, and contains a high resolution record of an important time in Earth's history. The stratigraphic age of the Tarfaya quarry sediments is discussed fully in section 4.5. They lie within the *Whiteinella archaeocretacea* Zone, above the $\delta^{13}C$ excursion and below the Cenomanian/Turonian boundary, which dates them to around 94 million years old. The entire section covered approximately three obliquity cycles (see section 4.4).

1.2 Objectives

The general aim of this research was to *zoom in* and focus on the detailed changes in biogenic carbonate production during an OAE.

One aim was to identify periods of cyclicity at the sub-Milankovitch scale, with the hope being that seasonal cycles would become evident. To investigate cyclicity a digitised, greyscale record was made of the sediment by scanning polished sections of the rock.

Another important objective was to record the changes in calcareous nannofossils and foraminifera, to see how they responded to differing oceanic conditions and to try and link these changes into any cyclicity in the sediment. Nannofossils were analysed on both the light microscope and scanning electron microscope, while foraminifera were analysed from thin sections.

1.3 Thesis structure

This thesis is divided into 7 chapters including this introduction.

Figure 1.2: Photo of one of the slabs of rock cut from the quarry near Tarfaya. The entire block is approximately 1.6metres in length.

Chapter two reviews previous work and introduces background material relevant to the research. It starts by looking at the geological and tectonic setting of the Tarfaya basin. The recent political history is then briefly mentioned before providing a historical overview of the previous research done at this location. The middle of the chapter provides an introduction to subjects that were important to this research, namely; atmospheric circulation, the Cenomanian/Turonian climate, oceanic upwelling, organic rich sediments, sediment preservation, calcareous nannofossils, and recognising cyclicity. The text is purposely selective during this discussion and the reader is referred to any one of a number of excellent review articles, cited in the text, for further reading on those topics. Finally the technique of digital sediment colour analysis (DSCA) is introduced since it is an important tool in this research.

Experimental procedures and statistical analyses are outlined in chapter three. The experiments are described in sufficient detail to be reproduced if necessary.

The results for everything except the time series analysis are presented in chapter four. Many of the results were best presented in graphic or tabular form and so the reader is frequently referred to appendices to view the full set of results.

Chapter five is devoted to time series analysis of the DSCA data, since this was a major part of the research and deserves an in depth discussion. The first half of the chapter gives a background to the subject of time series analysis, while the second half of the chapter details the results from time series analysis on the Tarfaya basin sediments.

A discussion on all the results from this thesis is presented in chapter six. Oceanic productivity scenarios are suggested with the reasoning behind their suggestion. The resulting environmental implications are also outlined.

The final chapter briefly summarises the findings from this research and indicates some future possibilities for further research.

2

Reviews

2.1 Geological Setting

2.1.1 Location and background

The Tarfaya Basin lies in the Moroccan Western Sahara, along the Northwest African Atlantic margin between the latitudes of 20°N and 30°N, (see Fig 1). The onshore part of the basin stretches for approximately 700km in the North-South direction and 100 to 250km in the East-West direction [137]. The basin has a total area of around 460000km^2, over 80% of which is under the present continental shelf, slope and uppermost rise [137].

The basin has a Hercynian basement, composed from folded Precambrian and Palaeozoic crystalline rocks [72], [99], [137], and [193]. The Mesozoic basin fill on this basin is unconformably overlain by a seaward thickening wedge of Cenozoic continental to shallow marine sediments [99], [137], and [193].

A number of oil exploration wells have been drilled in the Tarfaya area and their locations are shown in Fig 2.1(S5, S13, S20, S21, S25 and S75).

2.1.2 Cenomanian palaeolatitude

During the Cenomanian the Tarfaya Basin lay closer to the equator than it does at the current time. Fig 2.2 shows a reconstruction of the continental positions for

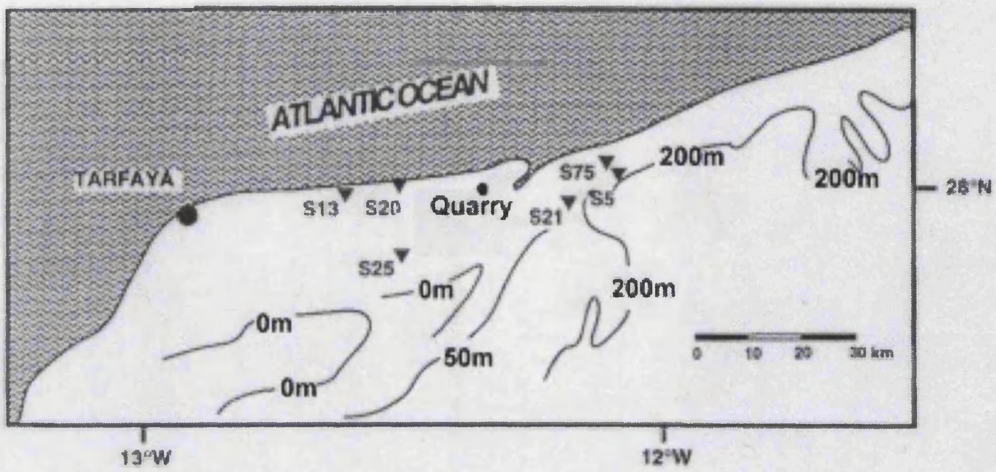

Figure 2.1: Location of the oil exploration wells in the Tarfaya basin. Contour lines show height above sea-level in metres. Site of quarry where the samples were taken from is indicated. Modified after Kuhnt *et al* (1997) [92].

90Ma and Fig 2.3 shows a more detailed reconstruction of the Tarfaya Basin region for that time. These reconstructions were computed using the Ocean Drilling Stratigraphic Network Plate Tectonic Reconstruction Service based at the Research Centre for Marine Geosciences at the University of Kiel [66], [125].

2.1.3 Facies succession

Two distinct Cretaceous depositional environments are observed in the Tarfaya region: one dating from upper-Albian to mid-Cenomanian, and the other from upper-Cenomanian to Campanian times. The former is dominated by terrigenous silici and bioclastic sediments, with low organic matter content [93]. Clay mineral assemblages indicate erosion of crystalline rocks from the Anti Atlas mountains [93]. The latter environment is characterized by pelagic chalks and limestones with a high content of marine organic matter [93]. It was this kind of environment that the sedimentary section studied in this thesis came from.

In the studied section, dark grey laminated kerogenous chalks alternate with non laminated lighter coloured limestones with a lower kerogen content [99]. Sediments consist almost exclusively of organic matter and biogenic carbonate. The

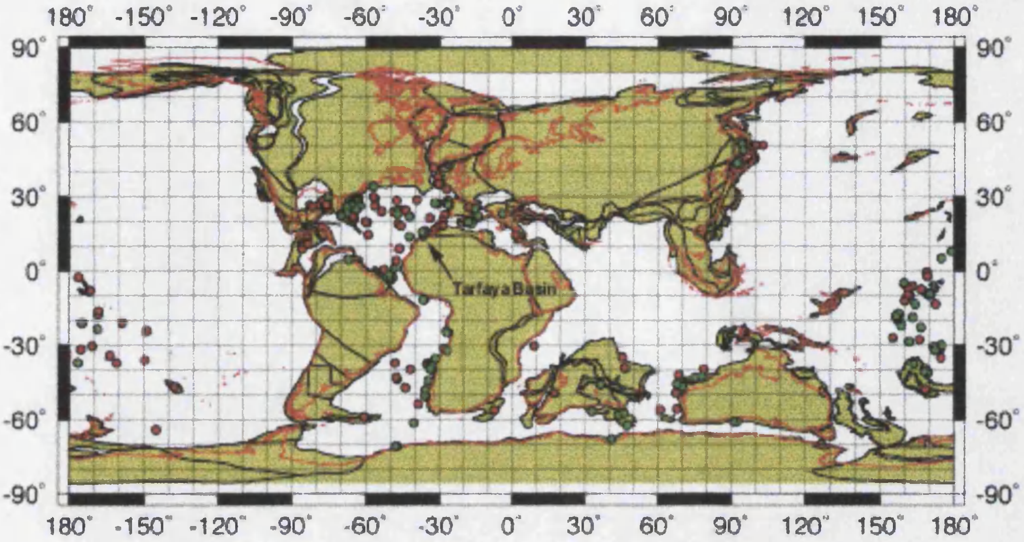

Figure 2.2: World reconstruction for 90Ma. Plate fragments - ochre, Present day shorelines - black, 90Ma shorelines - red, ODP sites - green dots, DSDP sites - red dots. This reconstruction was computed using the Ocean Drilling Stratigraphic Network Plate Tectonic Reconstruction Service [125].

organic content is very high, especially enriched in the dark layers (up to 18%). The biogenic carbonate content reaches up to 93% in light layers and is composed mainly of foraminifera (mostly *Heterohelicids*) and calcareous nannoplankton. An average 1cm of section contains between 125 and 225 light/dark couplets (laminae). These laminae are more distinct and continuous in the darker, organic rick sediment and can be traced laterally over the order of centimetres. By contrast the laminae in the lighter areas of sediment tend to change in thickness laterally and are not as well defined.

Sometimes the limestones are nodular with concretions and lenses of chert and siliceous limestone [99]. Marls and clays occur occasionally as intercalcations, but generally terrigenous input was very low [99]. Bioturbation is rare but some short bioturbated areas do exist (see section 4.3). Table 2.1 lists the stratigraphy and lithology of the Cretaceous in the Tarfaya area. Figure 2.4 illustrates a typical section from the current Northwest African coast, showing the Mesozoic basin fill overlain by unconformable Cenozoic shallow marine sediments. Figure 2.5 shows the same section in the Tarfaya quarry where the sediments for this thesis were

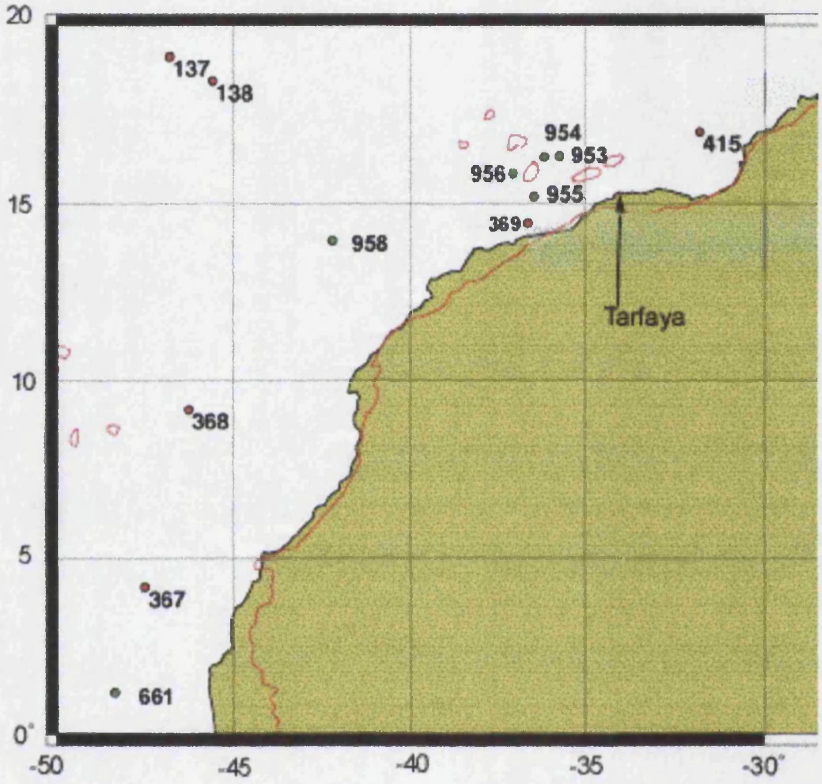

Figure 2.3: Detail of Tarfaya continental configuration 90Ma. Plate fragments - ochre, Present day shorelines - black, 90Ma shorelines - red, ODP sites - green dots, DSDP sites - red dots. This reconstruction was computed using the Ocean Drilling Stratigraphic Network Plate Tectonic Reconstruction Service [125].

Age	Thickness/m	Lithology
Plio-Pleistocene (Moghrebian)	0-45	Sandstones
Late Campanian	40	Oil shale sequence (chalks with varying kerogen contents)
Cenomanian to Early Santonian	700	Chert and siliceous limestones, becoming silt/clay rich towards top
Albian to Early Cenomanian	300	clays, marls and fine grained sandstones
Early Cretaceous	1350	Red and green sandstones, siltstones, coal fragments

Table 2.1: Stratigraphy and lithology of the Cretaceous in the Tarfaya area, double lines represent a hiatus. Modified after Leine (1986) [99].

collected.

2.2 Tectonic Setting

2.2.1 Pre-rift phase

The basement of the Tarfaya Basin was shaped during the Hercynian orogeny. Metamorphosed Paleozoic rocks were uplifted and eroded and a pervasive north-northeast to south-southwest structural fabric was established which was to influence later structural deformation during the Alpine orogeny [72].

2.2.2 Rift phase

The early North Atlantic was opened during the Late Triassic by normal dip-slip displacement to form half grabens [72], [137]. Triassic doleritic flood basalts are observed in the base of some of the exploration wells in the area and are thought to have been erupted during the tensional stages of the graben formation [137]. As extension progressed, marine waters encroached into the half grabens, probably from the east (Tethys) and north (proto-Atlantic) [137]. Marine circulation was restricted and this encouraged the deposition of thick evaporite sequences [72], [137]. This continued until the Early Jurassic time when continued extension and

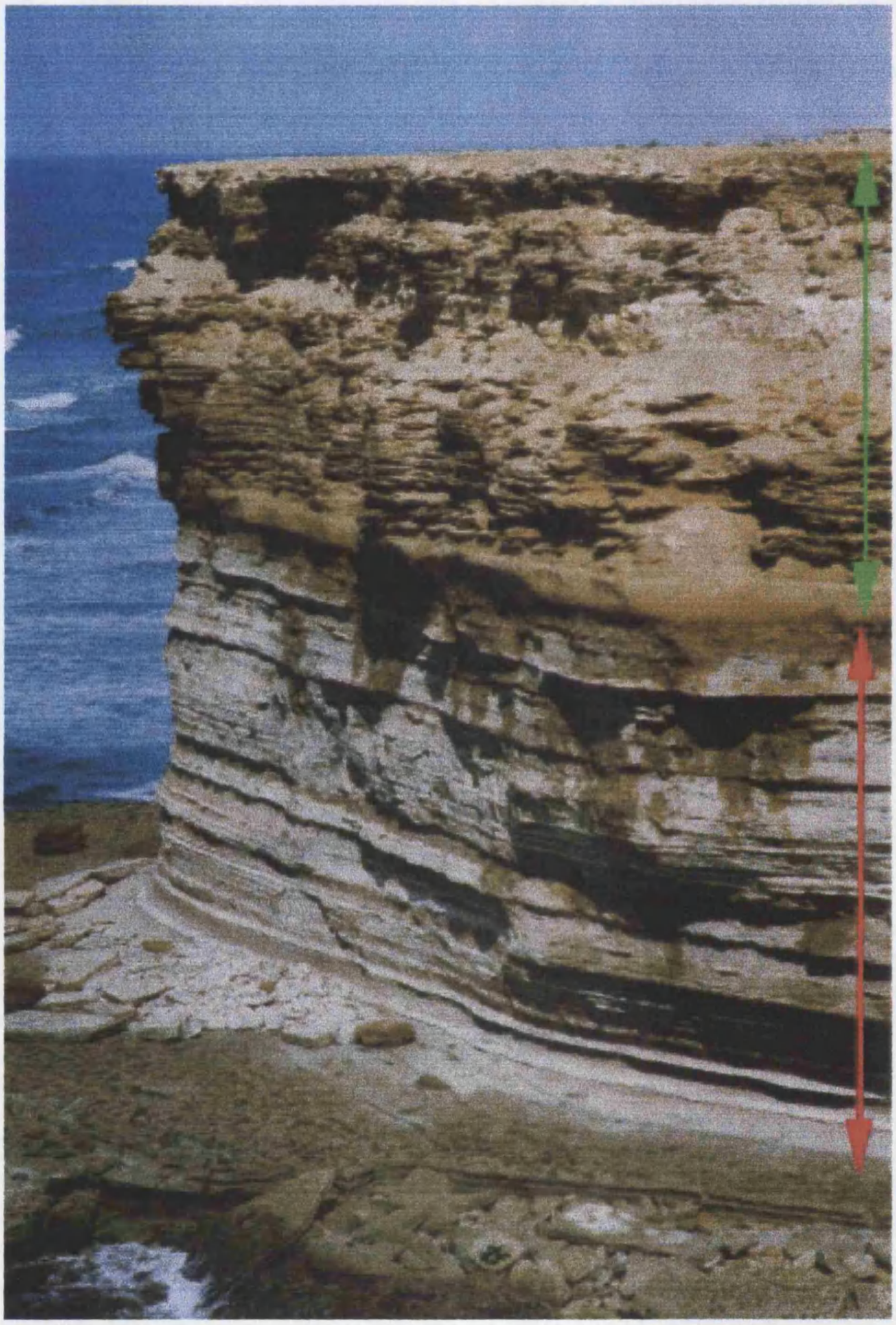

Figure 2.4: A typical section from the Northwest African coast near Tarfaya. The lower part of the photo is Mesozoic basin fill (red arrow), while the upper part is the unconformable Cenozoic shallow marine sediments (green arrow).

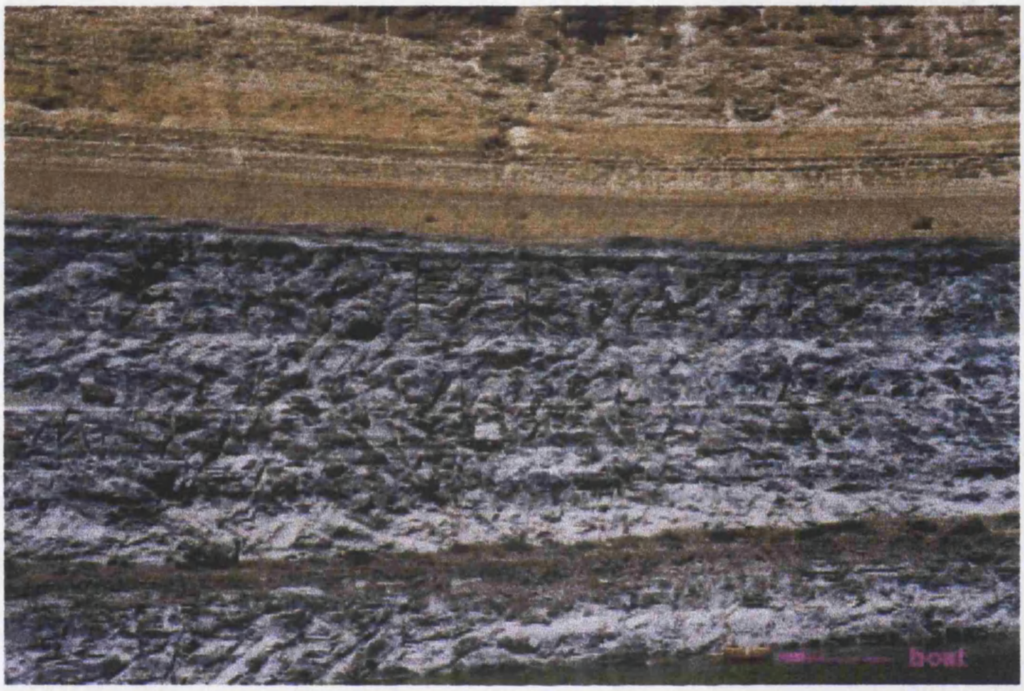

Figure 2.5: Photo of the quarry near Tarfaya where the sediments for this thesis were taken from. The sharp unconformity between the grey Mesozoic sediments and the orange Cenozoic sediments can be identified. A dinghy can be seen in the bottom right of the photo for scale.

subsidence resulted in open communication with the Tethys Sea [72], [2]. Exposed Precambrian and Paleozoic highlands shed clastic debris into the rapidly subsiding half grabens [72]. This was interfingered with thinly bedded marine limestones, shales and dolomites, resulting in more than 2km thickness of syn-rift sediments [72], [99], [137].

2.2.3 Post-rift phase

Open marine conditions were established in the Late Jurassic as waters from the proto-Atlantic flooded the rift basins of Morocco [72], [137]. Deep water carbonates were deposited far offshore while a widespread carbonate platform developed in the nearshore region [72], [137]. During the Early Cretaceous global sea level fall terminated the build up of the carbonate platform and a sequence of continental to marine sediments were deposited [72], [137]. By mid to Late Cretaceous marine transgression occurred and water depth increased continuously [42], [137]. During Cenomanian to Turonian times water depth reached a maximum of around 200m on the shelf and an expanded oxygen minimum zone and/or regional upwelling generated laminated kerogen rich chalks [99], [42]. During the Late Cretaceous waters shallowed again leading to emergence of the area by the end of the Cretaceous [72]. In early Miocene times the Mesozoic strata were locally tilted and domed and an anticline was formed [99]. Erosion truncated the Upper Cretaceous sediments and a thin layer of Upper Tertiary/Quaternary, belonging to the Moghrebian Formation, was deposited on the erosion surface [99], [32].

2.3 Political history

The Moroccan Western Sahara was inaccessible for conducting geological fieldwork from the early 1970s until the early 1990s due to political conflict over the future of the former Spanish Sahara [93].

Nonetheless two oil shale exploration campaigns were carried out by The Office National de Recherches et d'Exploitations Pétrolieres (ONAREP) and Shell Oil Company in the mid 1970s and early 1980s [93], [99].

Results from these borehole drillings remained confidential until the late 1990s. Following the release of the data and sample material, an international team from the Université de Marrakech, the Universität Kiel, the Universität Bremen, University College London and Université de Poitiers started a new field expedition in 1997 [93]. The rock samples that provide the data for this thesis were gathered on that field expedition.

2.4 History of Tarfaya Basin research

Geologists first began to study the Tarfaya basin sediments during the 1960s. Viotti *et al* (1966) studied the Jurassic stratigraphy [184], while Choubert *et al* (1966) focused on the late Cretaceous carbonate shelf deposits [32]. Political conflict prevented fieldwork during the 1970s, (see section 2.3), but by the 1980s various oil companies began to carry out preliminary investigations into developing the oil shale.

An intensive study of the Northwest African continental margin was carried out during the early 1980s. Ranke *et al* (1982) provide a comprehensive background to the evolution of the basin [137], while Wiedmann *et al* (1982) looked at the Cretaceous stratigraphy, environment and subsidence history of the continental margin [193]. Einsele & Wiedmann (1982) focused in on the Cenomanian black shales and the potential palaeo-environments that they may represent [42]. They conclude that these black shales may represent the first occurrence of oceanic upwelling in the newly formed Atlantic Ocean [42].

Leine (1986) summarizes the geology of the oil shale deposit and its potential for oil extraction [99]. Since the 1980s, interest in developing the area for oil extraction has waned, but a number of studies have made use of the cores drilled by oil companies. Luderer, Kuhnt and Nederbragt have done extensive research into the faunal assemblages and cyclicity observed in the sediments [92] [104] [105]. They observe a pronounced cyclicity of Milankovitch frequency, controlled by fluctuations in organic carbon and pelagic carbonate contents [92] [104]. Additionally Kuhnt *et al* (1990) carried out research into the organic carbon distribution in the Western Mediterranean and along the adjacent Atlantic margin [91]. A detailed stratigraphic framework is constructed using planktonic formainiferal, radiolarian and cephalopod zonations [91].

More recently El Albani *et al* (1999) have studied sea level fluctuations during the late Cretaceous by interpreting the structures seen in the pelagic, organic rich sediments [44]. They observe calcareous tempestites, hummocky cross stratification, bioclastic limestones and limestone channels in the late Cenomanian/early Turonian sediments [44]. They interpret this to mean that water depth fluctuated frequently and ranged from below, but near to storm wave base, to fair weather wave base, averaging at a depth of around 200 metres [44]. Most recently Kuhnt *et al* (2001) reviewed the research in the Tarfaya Basin so far and discussed the potential for the future [93].

2.5 Atmospheric circulation

2.5.1 Current atmospheric circulation

Between 30°N and 30°S (the tropics) the climate is dominated by the Hadley circulation (see Fig 2.6) [108], [11]. Close to the equator air masses from each hemisphere converge creating an area known as the Intertropical Convergence Zone (ITCZ). The air rises and heat is carried up into the troposphere (15km), producing large cumulonimbus clouds and frequent storms [108]. Air warmed by the cumulonimbus populations of the ITCZ drifts poleward in the high troposphere and then completes its cooling and descent in the subtropical high pressure zone [108]. At low levels the air flows equatorwards again in the form of *trade winds* [108].

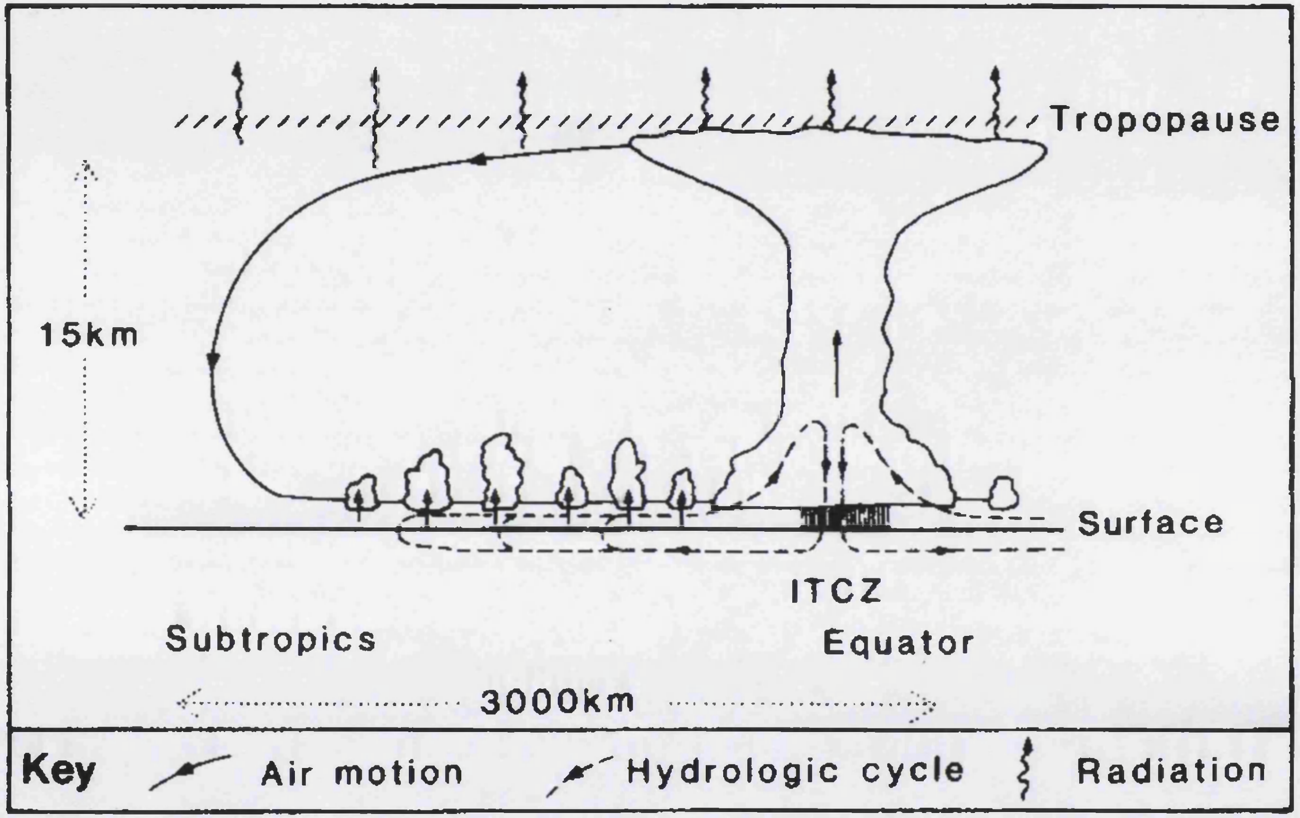

Figure 2.6: A vertical meridional section of the Hadley cell in one hemisphere. Modified after McIlveen (1995) [108].

The ITCZ shifts north and south of the equator seasonally with the sun, reaching its northernmost position in July and August and its southernmost position in January or February [49]. Over the interior of continents the movement of the ITCZ is most marked as the landmass responds quickly to the changing angle of the Sun [49]. In contrast the movement of the ITCZ over central oceans is perhaps only between 10°N and 10°S due to the slow response time of the ocean [49]. Fig 2.7 shows the movement of the ITCZ and the corresponding tropical rainy zone over the African continent today.

Due to the Earth's rotation the trade winds are deflected from running north-south. In the northern hemisphere the trade winds are given a westward twist and become the northeast trade winds. Similarly a mirror image pattern occurs in the southern hemisphere producing the southeast trade winds [49].

2.5.2 Factors effecting the atmospheric circulation

A number of factors can effect the intensity and size of the Hadley circulation. In turn this effects the strength of the trade winds and the degree of coastal upwelling. However, there is a limit within which the Hadley cell can change and, to some extent, it can be considered a self regulating system. The pace of the Hadley circulation is governed by the rate at which the returning low level air can pick up moisture [28]. Global models predict an optimum speed of circulation. The more moisture that is fed into the tropics, the faster the cell circulates, but above a certain speed the time of the return leg is cut too short to pick up enough moisture, so the energy input into the cycle is reduced and it slows down [28]. This means that the current Hadley cell has a characteristic circulation time of around 50 days and it tends to oscillate around this natural period.

One of the main parameters, thought to be an important influence on Hadley cell intensity, is the global latitudinal temperature gradient. An increased temperature gradient (with higher tropical sea surface temperatures and lower polar sea surface temperatures) is thought to occur with a decrease in global mean temperature [138]. This effect is most likely to have occurred in glacial times due to the snow/ice albedo feedback effect at high latitudes. Independent climate models all indicate that an increased global latitudinal temperature gradient will tend to

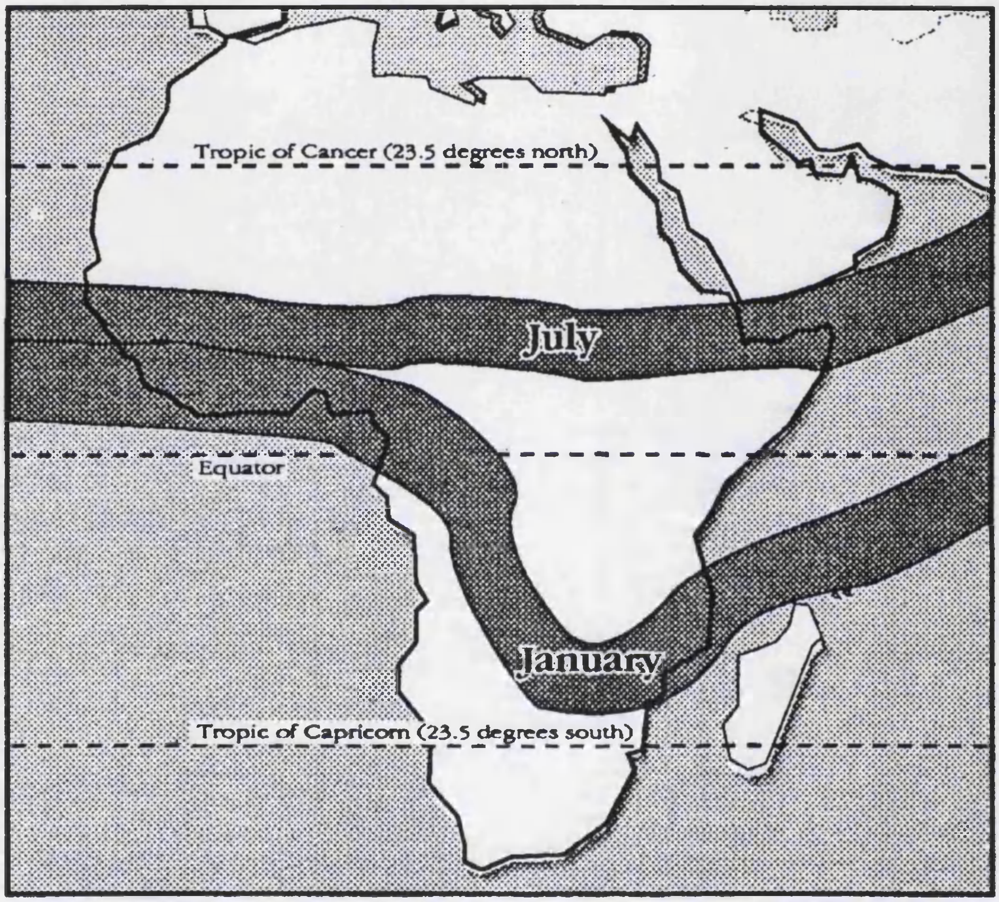

Figure 2.7: The movement of the ITCZ over the African continent today. Modified after File (1996) [49].

intensify the Hadley circulation [138], [3]. The increased thermal gradient drives the circulation faster [138]. Anderson (1995) [3], models a 40% increase in upwelling in the Eastern equatorial Atlantic during glacial periods with an increased latitudinal temperature gradient.

Changes in atmospheric carbon dioxide are also thought to have an effect on the Hadley circulation. However, the mechanism for change is not clear and there are two contradicting theories. In their doubled atmospheric carbon dioxide model, Rind *et al* (2001) [139], find a reduction in the Hadley circulation. They postulate that this is caused by a greater leakage of energy in the tropical transport from the troposphere to the stratosphere [139]. By contrast Manabe & Bryan (1985) [107], suggest that the greenhouse effect from increasing atmospheric carbon dioxide causes the Hadley cell to intensify and become taller. This effect is suggested to be caused by enhanced evaporation in the sub-tropics and increased delivery of moisture to the tropical atmosphere. It also implies a significant increase in the mean velocity of the trade winds, leading to increased oceanic upwelling along the equatorial divergence and in the eastern boundary currents [129].

Solar radiation is another factor that has a direct influence on the Hadley circulation. It is not easy to estimate the precise effect in different regions of the world as landmass distribution is strongly linked to the effect of solar radiation. Anderson (1995) showed that in general an increase in solar radiation would be expected to produce an increase in the intensity of the Hadley circulation [3]. This is hypothesised to be due to the large thermal and pressure gradients resulting from the differing heat capacity of the land and oceans [3]. However the effect is highly spatially dependent and his model indicates that over the Eastern equatorial Atlantic the current land/ocean distribution would actually serve to reduce the intensity of the Hadley cell if there was an increase in solar radiation, and potentially this would reduce coastal upwelling there by up to 50% [3].

Land distribution is obviously an important factor due to the differing heat capacities and response times of land and ocean surfaces. The annual movement of the ITCZ is greatest over the land because of the quick terrestrial response to changes in solar radiation. Equally it is likely that the ITCZ and Hadley cell movement respond to changes in solar radiation over longer timescales such as Milankovitch cycles. The changing configuration of landmasses over time, mean that the ITCZ will have moved in a different way in the past. During the Cenomanian there was a greater concentration of landmasses than today (see Fig 2.2) and possibly this means the ITCZ and Hadley circulation would have covered a greater range of latitudes than today.

2.6 The Cenomanian-Turonian climate

During the late Cenomanian and Turonian the Earth is thought to have supported an extreme greenhouse climate [74] [10]. Oxygen isotope analyses from well preserved foraminifera suggest that no significant ice sheets existed at this time [121], [74], [122]. Tropical sea surface temperatures are estimated to have been 4 – 7°C warmer than the highest modern mean annual temperatures (with mean tropical sea surface temperatures as high as 33°C) [122], [195], while middle bathyal water temperatures were also higher than at present, reaching up to 20°C in the Blake Nose area of the North Atlantic [74].

Many authors have found evidence for enhanced volcanic outgassing and high sea floor spreading rates at this time [10], [97] [83], [82], [83]. Although such activity would have increased levels of atmospheric carbon dioxide, it is not clear that this was the driving factor behind climate change at this time. Poulsen *et al* (2001) calculate that changing atmospheric carbon dioxide concentrations by up to four times present day levels alters global circulation very little [134]. Instead they suggest that climate and oceanographic changes around the Cenomanian/Turonian (C/T) boundary were driven by the initiation of a connection between the North Atlantic and northern South Atlantic oceans.

Other authors believe that atmospheric carbon dioxide levels will have decreased at this time due to the widespread burial of organic matter in black shales during the C/T oceanic anoxic event (see section 2.7.3) [6], [94]. Kuypers *et al* (1999) found evidence for a sudden change in the plant communities of the North African continent, suggesting that atmospheric carbon dioxide levels fell abruptly over a short time period of just 60,000 years [94]. Falling atmospheric carbon dioxide levels are indirectly supported by oxygen isotope data from high latitude locations indicating an 8 – 13°C cooling [6], [79], and an incursion of boreal fauna into low latitude seas [90].

It is still not clear what mechanisms were driving the C/T climate, nor exactly what the climate was like. However the C/T does seem to represent a climatic extreme in the Earth's history and hence it is an important period to study if we wish to further our understanding of global climate.

2.7 Oceanic upwelling

2.7.1 Upwelling along the Northeast African margin

Coastal upwelling occurs along the Northeast African margin in response to the surface winds [153], [56], [21], [144]. Offshore Ekman transport of surface water is generated by the interaction of trade winds and the Earth's rotation [56], [166], [144]. The surface waters are replaced by the cooler, more nutrient rich, subsurface waters from the Canary Current [153], [56]. At present upwelling is most strongly developed and occurs year round between 20°N and 25°N. Seasonal variations in upwelling are caused by the latitudinal shift of the subtropical high pressure system, known as the Azores High and of the tropical deep pressure system related to the ITCZ [55]. In the northern hemisphere winter upwelling is enhanced in the south (between 10°N and 25°N) towards Sierra Leone. During summer upwelling is enhanced in the north (between 20°N and 32°N) up to Morocco and Portugal [56], [153].

Off the coast of Morocco the strongest upwelling occurs during the summer and autumn. It occurs in a coastal band about 50km wide, mostly on the shallow (less than 100m) continental shelf [181]. In addition areas of upwelled water stretch out as far as several hundred kilometres offshore as filaments of cold, nutrient rich, coastal waters created by the interaction of the Canary Current, coastal upwelling and morphological features [80]. Upwelling in these filaments is also dependant upon the strength and duration of trade winds, although the most intense filaments of upwelled water often lag behind the timing of the maximum trade winds [123].

Coastal upwelling along this continental margin is thought to have started during the mid-Cretaceous as the early North Atlantic began to establish and open marine circulation started [42]. Although long distance, cold bottom currents probably did not exist at this time, the surface waters were still cool as evidenced by the occurrence of a northern temperate fauna [42].

One possibility is that the cool surface waters were formed by vigourous upwelling, due to the strong trade winds operating at that time (see section 2.5).

2.7.2 Sedimentation in upwelling regimes

Upwelling introduces new nutrients into the euphotic zone and so enhances biological productivity [75]. The high productivity can increase fluxes of organic matter, which in turn can cause bottom waters to become locally anoxic as organic matter decomposes on the sea floor [173]. The formation of low oxygen to anoxic water is a key factor in minimising bioturbation and allowing deposition of laminated sediments [75]. Preservation of the upwelling signature is further discussed in section 2.9.

2.7.3 The Cretaceous ocean and Oceanic Anoxic Events (OAEs)

The mid-Cretaceous (120 - 80Ma) was a time of unusually warm polar temperatures, repeated reef drowning in the tropics, and a series of oceanic anoxic events [194]. Many parts of the world ocean experienced deposition of sediments anomalously rich in organic carbon, probably due to the presence of oxygen deficient conditions in the ocean and/or high fluxes of organic matter to the sea floor [129], [158]. Three major OEAs can be identified in the mid-Cretaceous stratigraphy as follows [78].

OAE1 late Barremian through Albian

OAE2 late Cenomanian through early Turonian

OAE3 Coniacian through Santonian

The climatic causes and effects of OAEs are still not clear and a range of competing hypotheses have been proposed.

Erbacher *et al* (2001) [46] present evidence for increased thermohaline stratification as a possible cause of OAEs. Stable isotope data suggests that the increase in surface water temperatures during OAE1b led to decreased bottom water formation and elevated carbon burial in the restricted basins of the western Tethys and North Atlantic.

In contrast Pedersen & Calvert (1990) [129] dispute the sluggish circulation hypothesis and suggest instead that Cretaceous bottom waters were more prone to oxygen depletion due to warmer waters. Based on Manabe & Bryan's (1985) [107] coupled ocean-atmosphere model they argue that the intensity of thermohaline circulation was the same, or even higher than today. They reason that the co-efficient of thermal expansion of sea water is greatly increased by higher temperatures, so maintaining, or even increasing, the meridional density contrast at the ocean surface compared to today [129]. However the relatively warm, newly formed deep waters would have had a reduced dissolved oxygen content, since the saturation oxygen concentration of seawater is less at higher temperatures. This effect would have meant Cretaceous bottom waters were more prone to oxygen depletion, especially if there was a large flux of settling organic matter.

2.7.4 Extreme climates

Throughout Earth's history the Earth has experienced a *greenhouse* climate on a number of occasions. These intervals of elevated temperatures and transient events, where climate changed abruptly on time scales of several thousand years or less, may provide interesting parallels to how the Earth's climate may behave in the future. The OEAs described in the previous section are all examples of carbon cycle perturbations linked to climate change. Another major global warming period was the Paleocene/Eocene thermal maximum. This is thought to be associated with a rapid injection of greenhouse gases, most probably methane hydrates from the deep sea. However the mechanism that triggered the release of gases from the deep sea is still not clear and theories ranging from asteroid impacts to submarine landslides have been proposed.

2.8 Conditions for the accumulation of organic rich sediments

There are three main factors controlling the accumulation of organic matter in marine environments: production rate of marine organic matter, preservation rate of marine organic matter and supply of terrigenous organic matter. Figure 2.8 is a flow chart indicating how each of these factors dominate in different marine environments. The following subsections discuss each of these factors in turn.

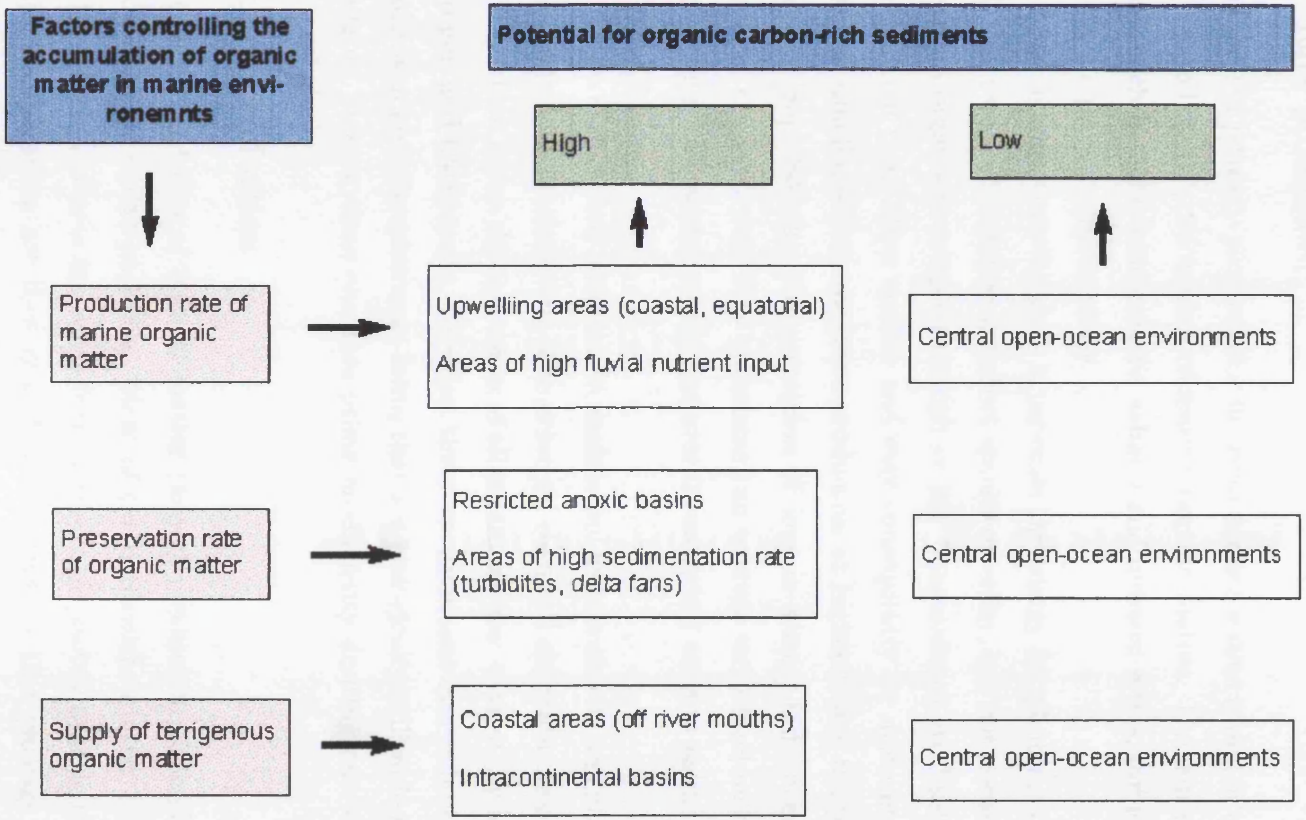

Figure 2.8: Factors controlling the accumulation of organic matter in marine environments. Modified after Stein (1991) [169].

2.8.1 Production of marine organic carbon and flux to the sea floor

Primary productivity

The level of primary productivity in ocean surface waters is one of the key factors in controlling the production of marine organic matter. Certain oceanic conditions, such as light, temperature, salinity and nutrient levels, influence the levels of marine primary productivity.

Light is important because it provides the energy for photosynthesis to occur [86]. Extremes of temperature affect species diversity, but not necessarily productivity, as organisms adapted to high or low temperatures are likely to have less competition from other species and may consequently be more productive. For example dinoflagellates are more productive at higher water temperatures than diatoms [86]. Salinity (concentration of ions in water) influences the primary producer communities. Few organisms can tolerate large fluctuations in salinity (eg. where fresh water meets seawater in estuaries) or very saline (hypersaline) conditions.

Levels of dissolved nutrients in surface waters can also be an extremely important control on productivity. The principal chemical elements making up organic matter which forms the soft tissue of all organisms are: oxygen, hydrogen, carbon, nitrogen and phosphorus. The first three are abundant everywhere, but supplies of nitrogen and phosphorus in forms that are biologically utilisable are not always available, making these elements prime productivity limiting nutrients.

Export production

The downward flux of organic matter (export production) is highly dependent upon the size of the particles. Most of the particulate matter falling from the surface layers of the ocean is produced initially by photosynthetic phytoplankton. The phytoplankton are then grazed by zooplankton that package most of their waste products into faecal pellets, which in turn are consumed and decomposed by other organisms including bacteria. As the particles fall through the water column, the organic matter in them provides food for successive populations of filter feeders and other animals, so that it is re-packaged several times *en route* to the sediment. A small proportion (less than 1% on average) of the organic matter survives in particles that sink to the sea bed [14].

Marine particulate matter can be subdivided according to size and biological origin. The smallest particles (less than $1\mu m$ up to a few tens of μm) comprise bacteria and algal cells and other fine organic detritus; coccoliths, diatom skeletons and inorganic particles. The medium size range (from tens to hundreds of μm) is represented by larger detritus and faecal pellets. Finally, the largest particles which are easily visible (macroscopic), are aggregates known as *marine snow*. They consist of detritus, living organisms (including bacteria) and some inorganic matter. Typically they are several mm across and can even reach dimensions of several cm.

A range of physical mechanisms lead to particle aggregation and marine snow. Interactions between the smallest (μm-sized) particles are dominated by Brownian motion. Differential settling and turbulence in the water column lead to collisions between the particles and capture of small particles by large ones. The most important biological mechanism aggregating small particles together is feeding, creating faecal pellets.

Marine snow is most abundant in surface waters. Most marine snow is disaggregated and/or eaten and re-packaged into faecal pellets within the upper 500 to 1000m of the water column. Below 1000m it is faecal pellets that provide the main component of the sinking particle flux [14]. However in certain circumstances the rate of production of marine snow can exceed the rate of disaggregation and/or consumption in the upper water column. One such situation is a strong seasonal bloom of phytoplankton. In this case marine snow may form in such large quantities that significant amounts reach the sea-bed more or less intact.

Marine environment

Water depth, oceanic circulation, water velocity and local bottom water currents are all important factors in determining how much of the export production reaches the sea floor. The deeper the water, the longer the particles spend reaching the bottom and the more likely they are to degrade. Generally the amount of organic material reaching the bottom decreases by a factor of ten for every tenfold increase in water depth [86].

Larger particles, such as zooplankton faecal pellets, settle more quickly through the water column than smaller particles, such as phytoplankton remains (an average of 160 metres per day for faecal pellets compared to 0.15 metres per day for coccolithophore cells) [86]. Hence the size of the particle can be a crucial factor in whether it will reach the sea floor or not. Suess estimated that faecal pellets with a diameter greater than $200\mu m$ are the most important in the formation of organic rich sediments [172].

Central ocean gyres are characterised by low productivity because of their limited nutrient supply. Conversely the most productive regions tend to be the coastal upwelling areas such as off Northwest and Southwest Africa, Arabia and Peru, where upwelling brings nutrients to the surface. Shallow seas and coastal areas generally benefit from river borne nutrient supplies from adjacent landmasses, and so tend to have higher productivity than the open ocean, but lower productivity than upwelling regions.

2.8.2 Preservation of organic carbon

The preservation rate of organic carbon in the marine environment is controlled by several factors including oxygen content of bottom water, bulk sedimentation rate, extent of bioturbation, and composition of organic matter [169].

Oxygen depleted environments (anoxic) can be developed in two different ways: a reduced vertical circulation (density stratification) or extremely high productivity. The Black sea is a good example of density stratification anoxia. The reduced vertical circulation prevents sufficient ventilation of the deep water. By contrast extreme high productivity upwelling environments (such as that seen off Namibia) create bottom water anoxia from the high oxygen demand due to the decomposition of large amounts of organic matter produced in surface waters.

In oxic environments respiration is the main mechanism decomposing organic matter, whereas in anoxic environments sulphate reduction becomes the most important mechanism.

Once organic carbon reaches the seal floor the efficiency of burial is related to the bulk sedimentation rate [69]. At low sedimentation rates burial efficiency tends to be higher for anoxic sediments than oxic sediments [29].

2.8.3 Supply of terrigenous organic carbon

Compared to the amount of organic carbon produced by marine organisms, the supply of terrigenous organic carbon to the world's ocean is small [143]. Terrestrial organic carbon can be transported to the sea by rivers and by winds in particulate forms, and by rivers in dissolved forms.

2.9 Preserving the productivity signature in the sediment record

When trying to interpret the environment of deposition of a sedimentary record it is fundamental to question how representative that sediment is of its original environment. Various studies have been conducted in modern day oceanic areas to ascertain how much of the particle flux is converted to the sediment record [4], [56], [87], [167], [186].

Re-suspension and lateral advection have been found to strongly influence sediment accumulation [4], [56], [167], [186]. If the bottom water currents are strong enough they can completely wipe out any seasonal pattern in the coccolithophore flux [4]. Another important factor is coagulation. Kiorboe (1994) found that the rate of aggregate formation by physical coagulation in spring diatom blooms depends upon the concentration of suspended particles, the turbulent shear making the particles collide and increase their likelihood of sticking together [87]. Rapid deposition signals are often buffered and greatly modified by mid and deep water zooplankton communities [186].

Of particular relevance to this thesis is the recent CANIGO (Canary Islands Azores Gibralter Observations) study. This looked at current and Quaternary upwelling patterns over an area that included the Tarfaya Basin [127]. Sediment trap work revealed that coccolith fluxes were highly seasonal, predominantly occurring in an annual bloom [168]. Dust input from the Sahara was important in providing nutrients (especially Iron) to the ocean surface and triggering the annual bloom. Typically dust storms (of 3 to 8 days duration) were most frequent in the early winter [179]. However there is high interannual variability in both the frequency and intensity of the dust storms. The underlying sediment was not always very representative of the surface water productivity and it is thought that bottom water currents play a part in redistributing material [56] [168], [1]. In addition Abrantes *et al* (in press) noticed that generally opaline organisms such as diatoms were poorly preserved in comparison to carbonate organisms such as coccoliths [1]. In contrast other modern upwelling areas such as those off Oregon or Peru do exhibit shallow water upwelling facies in their sediments [56]. This is thought to reflect the lack of a strong sea floor current off Oregon or Peru.

Glacial to interglacial variations in productivity could be seen in the underlying sediment in the Canary Basin. During the last glacial maximum higher values of total organic carbon and higher sedimentation rates were observed, while interglacials exhibited enhanced carbonate accumulation and lower sedimentation rates [68] [55]. However local variations were also seen, sometimes with a completely reversed glacial/interglacial signal [68]. Freudenthal *et al* 's (in press) Canary Basin reconstruction reveals that during glacial times trade wind intensity was increased and showed strong variability with frequencies related to both obliquity and precession [55]. However, there was also high spatial variability in productivity during glacial times indicating different forcing mechanisms at work. Two processes were identified to influence the productivity record: global sea level changes controlling the size of the upwelling zone, and the strength of the summer NE trades determining the upwelling intensity [55]. Fütterer (1983) suggests that the continental shelf becomes narrower during glacials (as sea level falls) and that perhaps a narrower shelf is better able to preserve its upwelling signature [56].

Other factors that can influence the preservation of an upwelling facies include; rate of upwelling and nutrient input and the subsequent productivity, rate of particulate settling, rate of dissolution in the water column, sea floor oxygenation, remineralisation in the sediments, and reactivity and solubility of biogenic silica at the sea floor [77].

Many of these factors are interlinked. For example sea floor anoxia can be encouraged by a high rate of sedimentation. The situation is complex and there is no one ideal environment which preserves upwelling facies.

2.10 Calcareous nannofossils

2.10.1 Calcareous nannofossils as palaeoenvironment and palaeoclimate indicators

Using calcareous nannoplankton as palaeoceanographic and palaeoclimate indicators is a relatively new and growing science. McIntyre (1967) was one of the first people to realise their potential and he used coccoliths as palaeoclimate indicators of Pleistocene glaciation [109]. Following this research the CLIMAP (Climate: Long-range Investigation, Mapping and Prediction) group was established and calcareous nannoplankton were again utilised to provide estimates of oceanic surface water temperature [34]. Since then numerous studies have utilised coccoliths as indicators of palaeoenvironment and palaeoclimate and the following references represent just a few of those [7], [13], [19], [24], [45], [48], [51], [53], [60], [70], [36], [95], [100], [106], [114], [128], [147], [148], [154], [174], [177], [187].

Calcareous nannoplankton form an important phytoplankton group in the oceans, both in terms of diversity and productivity. Their tests constitute about half the calcium carbonate in modern deep sea sediments and are usually the principal constituent in pelagic chalk sequences [15]. During the Late Cretaceous large areas of northern continents were covered by shelf seas and sediments consisted almost exclusively of pelagic chalk [178]. Present day coccolith rich material is deposited in subtropical and tropical regions, underlying waters with moderate and low organic productivity. They are fewest in sediments from subglacial waters where productivity and preservation conditions are unfavourable [26].

Due to their particular light, nutrient and temperature requirements, coccolithophores inhabit a limited number of environments. Most calcareous nannofossils appear to show a marked temperature dependence; a higher diversity is found in the tropics and they are rare or absent in the higher polar latitudes [196]. In modern nannoplankton assemblages higher densities occur in nutrient rich waters such as on continental shelves or areas of oceanic upwelling [196]. Most species of calcareous nannoplankton are also light limited and live in the upper 200m of the water column [60]. Since calcareous nannofossils are planktonic rather than free swimming, their distribution is dependent upon ocean currents [196].

Most organisms can be separated into groups defined using ecological and morphological criteria. Young (1994) [197] applied the concept of ecological strategy grouping to coccolithophores and distinguished three commonly accepted groupings as follows.

The first group are known as r-strategists, responding to nutrient enrichment with enhanced growth rates or productivity. This group tends to live in equatorial waters, high latitudes and upwelling areas where the nutrient supply is often pulsed or seasonal. Often these species are bloom forming. The second group are known as K-strategists, adapted to low nutrient conditions at subtropical latitudes, especially the oligotrophic mid-ocean gyres. The third group is especially adapted to live below the mixed layer in low light intensity but with relatively high nutrient levels. They are found in low to mid latitude locations. Identifying analogs of these three categories of coccolithophores within fossil coccolith assemblages can provide valuable palaeoenvironmental information.

One advantage of calcareous nannofossils is that they are often well preserved in sediments where other potential productivity indicators, such as diatoms, have succumbed to diagenesis and dissolution [115] [1].

Generally the distribution patterns of living coccoliths is reflected in the bottom sediments [109], but some distortion occurs due to selective destruction and/or dissolution [152]. Section 2.9 discusses this further and looks at the transformation of a living coccolith community into a fossilised coccolith assemblage in the sediment.

2.10.2 Mesozoic palaeoceanographic studies

A number of quantitative studies, looking at the preservation and biogeographic distribution of calcareous nannofossils in Mesozoic sediments, have provided palaeoceanographic interpretations for Mesozoic oceans.

Mesozoic calcareous nannofossil species have been extensively studied by biostratigraphers and are relatively well documented [23], and this has enabled interpretations of the environmental preferences for selected taxa. An extensive study of Early Cretaceous palaeobiogeography of calcareous nannoplankton was carried out by Street and Bown (2000) [170]. They assessed Early Cretaceous nannoplankton biogeography by studying a series of sites with locations throughout the world's oceans. The Upper Cretaceous has been studied in depth by Burnett and a comprehensive guide to Upper Cretaceous nannoplankton palaeobiogeography can be found in Burnett (1998), [27].

The Ocean Drilling Program (ODP) has provided (and continues to provide) a globally distributed data set of Mesozoic nannofossils. In the early 1980s, Roth and Bowdler carried out extensive research on Atlantic sediments to establish the palaeoceanographic evolution of the Atlantic [147]. They were able to recognize three different coccolith assemblages; boreal and austral assemblages at latitudes greater than 40°, neritic assemblages along the continental margin of the eastern Atlantic and over the Walvis-Rio Grande Ridge, and oceanic assemblages in areas far removed from continents [147]. A few years later Roth and Krumbach modified this study by correlating nannofossil dissolution with organic carbon content and consequently they were able to postulate the location of upwelling oceanic areas [148].

Since then a number of studies have identified coccolith assemblages relating to a particular environment [36], [117], [187]. Thomsen carried out a detailed lamina by lamina study of the calcareous nannofossils in the lower Cretaceous 'Munk Marl' bed and managed to identify seasonal fluctuations in the nannofossil assemblages [177], [178].

In addition specific nannofossil species or groups of species have been recognized as being indicators of a particular palaeoenvironment. Correlation of nannofossil data with independent geochemical, sedimentological and paleontological evidence of increased fertility of surface waters has produced the following interpretations. *Biscutum constans* has been suggested as an indicator of a fertile environment [45], [51], [147]. *Zeugrhabdotus erectus* is a eutrophic species that indicates a moderately fertile environment [51], while *Watznaueria barnesae* suggests a low fertility environment [45], [51]. *Eprolithus floralis* may indicate a cold water and/or high latitude, high productivity environment [95], [148], while *Broinsonia* spp. is thought to be a shallower, cold water taxon [95], [147]. Scarparo Cunha recognised *Tranolithus* spp. and *Retecapsa* spp. as probable indicators of nutrient enrichment in shallow waters [154].

By analogy with extant coccolithophores it has been inferred that high nannofossil diversity assemblages tend to correlate with areas that were thought to be of low productivity, while low diversity assemblages tend to occur in regions that were thought to be high productivity [48], [187]. Probably the extreme conditions during high productivity favour certain taxa and suppress nannofossil diversity [48]. Eshet and Almogi-Labin (1996) use the ratio between high productivity and low productivity nannofossil groups (the Nannofossil Index of Productivity) as a productivity proxy [48]. Gale *et al* used faunal and geochemical changes as a measure of productivity and identified a marked drop in surface water productivity in the Eastbourne Late Cenomanian/Early Turonian sediments [58].

Lastly some nannofossils are good indicators of carbonate preservation. In particular *Watznaueria barnesae* is thought to be dissolution resistant and high percentages of this species in an assemblage can indicate poor preservation [51], [95]. However using calcareous nannofossils as preservation proxies needs to be carried out with care since nannofossils also respond to primary environmental signals. For example *Watznaueria barnesae* sometimes responds to oceanic productivity conditions and has been recorded as an indicator of low fertility conditions [51], [95]. Other species that may express the level of carbonate preservation include *Eprolithus floralis* and *Broinsonia* sp., dissolution resistant species, [24], while *Biscutum constans* is thought to be susceptible to dissolution [30]. Calcareous nannofossil populations that have been largely unaffected by primary environmental signals can be good indicators of carbonate preservation.

2.11 Recognizing cyclicity in sediments

Some sedimentary sequences can provide an excellent record of cyclic changes of the environment in which they were deposited. Over one hundred years ago Gilbert (1895) [61] suggested that there was cyclic repetition in the limestone/marl alterations in the Late Cretaceous of North America's Western Interior Seaway. In the early 1940's Milankovitch advanced the theory that low frequency variations in the Earth's orbit cause minor variations in insolation patterns and hence may drive the waxing and waning of continental ice sheets [113]. One of the first geologists to realize the potential of cyclic changes was Wells (1962), who recognised daily and annual banding in Devonian rugose corals and was able to estimate the number of days in the Devonian year to over 400 [192]. Soon after Scrutton recognised lunar effects and was able to estimate periods of Earth-Moon orbits for the Devonian [161]. However it wasn't until the 1970s that the potential of sediments for recording orbital forcing was truly realized. Ocean drill cores documented evidence of temperature changes that really established orbital forcing theories indisputably [67], [76], [37].

The ocean record sampled by ocean drilling [171] [188], has great potential to record cyclicity in sediments. Cores can be sampled and analyzed in a number of ways including microfossil biostratigraphy [22], magnetostratigraphy [65], carbonate analyzes [150], oxygen isotope stratigraphy [162] and digital sediment colour analysis [155].

Since the 1970s computers have been getting more powerful and the development of efficient mathematical programs has meant that spectral analysis of large amounts of data has become a practical proposition.

Many sedimentary records from all geological time periods have been analyzed for signs of cyclicity. In particular there has been much success with Cenozoic sediments in identifying both Milankovitch cycles and higher frequency millennial to decadal scale variability, eg. [163], [50], [132], [31], [88]. Further back in the sediment record it is more difficult to find pristine examples of high resolution sedimentation. Sediment diagenesis, compression and dissolution have taken their toll, while the fossil species are different to those of today. Nonetheless there have been many notable successes in identifying Milankovitch cycles in Mesozoic and even Paleozoic sediments and the following references represent just a few of those [126], [191], [57], [71], [103], [159], [189].

2.11.1 Cyclicity or Chaos?

Regular sedimentary cycles are commonly explained using the Milankovitch hypothesis: orbitally controlled variations in incoming solar energy have a measurable input on the stratigraphic record. However there is also an alternative way of explaining sedimentary cycles using non linear dynamics (Chaos theory). This predicts complex, non random output from natural systems where feedback mechanisms are important [165]. Most natural systems can be described as non-linear or *chaotic.*

In principal one would like to imagine that the sedimentary response to climate cycles is entirely linear. In such an environment the analysis of sedimentary cycles would simply involve careful removal of noise to reveal a direct proxy for the underlying climate system. The sedimentary system is highly unlikely to respond in such a linear way to global climate changes. In practise local and internal effects (such as channels and eddies in shallow water systems and turbidites, flocculation of particles and water turbulence in deep water systems) are likely to play a significant, if not dominant role.

The effects discussed in the previous paragraph mean that the system can be described as a non-linear coupling to the external environment. A non-linear system can resonate to an incoming signal, or damp it out completely, the stronger the coupling, the greater the range of frequencies over which the system will lock onto the incoming signal and amplify it [9]. Non-linear dynamics and chaos theory were put into a geological context by Middleton [111]. Chaotic systems in particular are ones which are exceptionally sensitive to the fine details of the system's configuration. The paradigm example for such systems is the driven double pendulum, where the simple driving force produces a whole range of responses and behaviour from the double pendulum [116]. Importantly these responses are not random in the strictest sense, but merely a complex amalgam of recurring simpler states.

Another class of such systems which have been more recently discovered are those that exhibit so called *Self Organised Criticality* (SOC). The applicability and universality of this effect if still contentious, but the underlying principles are undoubtedly real. Current consensus is that systems likely to exhibit the hallmarks of SOC are those which are *slowly* driven and interaction dominated. Given the time frames and scales of sedimentary processes it seems unlikely that this effect will be completely absent in sediments. Self similarity is one of the hallmarks of non linear dynamical systems that is often demonstrated in sedimentary cycles. Stratigraphic sections show repetitions of similar conditions on all scales from millimetres to many hundreds of metres, that represent time intervals from seconds to many millions of years [160]. A SOC system internally drives itself to a given state and this is characterised by power law Fourier series. Pelletier demonstrated that atmospheric temperature as recorded in ice core records shows just such a power law Fourier series [130]. He found that from 40ka to 1Ma a flat spectrum is observed, from 2ka to 40ka the spectrum is proportional to $f^{(-2)}$, where f is the frequency, and below time scales of 2ka the power spectrum is proportional to $f^{(-1/2)}$.

It is perhaps evidence of how important Milankovitch forcing is, that we see numerous examples of sedimentary rhythms with periodicities matching extremely closely with the predicted orbital frequencies [76], [67], [37]. The problem is that the mechanism by which the orbital signal is encoded in the sediment generally remains obscure [165]. In addition some stratigraphic records such as the Lias of southern Britain exhibit a Milankovitch signal that appears to increase and decrease in intensity [190]. Non linear dynamics can provide a convincing explanation for this kind of behaviour in a system.

The above material is well described by Smith (1994) [165] and he suggests that non linear dynamics and the Milankovitch hypothesis both play an important part. At some points in time parts of the sedimentary process are phase locked with the incoming orbital signal, while at other times it is damped out completely. This can be compared to the behaviour described by the driven double pendulum mentioned above. This of course raises a fundamental problem with all such analysis - if Milankovitch cyclicity is suppressed can we differentiate between local damping due to the inherent non-linearities in the system and global suppression when the atmosphere as a whole is acting independently of the underlying Milankovitch cyclicity?

Bailey (1998) takes this idea one step further and describes Smith's stratigraphy machine as a chaotic global system, combining the operations of the atmosphere, hydrosphere, lithosphere and asthenosphere, which everywhere tends to self organise towards a critical state in which continuous loading of the system with rock waste over time, is balanced by the unloading which creates the record [8]. He goes on to say "it is dangerous to assume that any perceived cyclicity provides an unambiguous chronicle of process cyclicity, whether eustatic, climatic or tectonic" [8].

The idea of a non-linear stratigraphy machine is applicable to biogenic environments as well as clastic ones. In the case of a biogenic environment, such as the Tarfaya Basin, the local internal effects that may over-ride an external signal include processes such as particle flocculation, bottom water currents and eddies and water turbulence.

2.12 Digital sediment colour analysis

2.12.1 Advantages of digital sediment colour analysis

In order to study high frequency climate variations in the rock record it is necessary to generate high resolution data sets. Varved and laminated sediments may record semiannual to annual changes in climate but it is usually difficult and highly destructive for the sediment, to take geochemical or palaeontological samples at this resolution. The advent of high resolution digitizing systems and image analysis software has enabled digitization of the colour of a sediment. Digital sediment colour analysis (DSCA) provides a fast and non-destructive way of generating a high resolution time series of sediment colour variation. The spacing of the data is much denser than would be possible with traditional sampling methods [155].

2.12.2 Disadvantages and problems with DSCA

One of the biggest problems with DSCA is reflections from water particles and mineral grains within the sediment during scanning [33]. To avoid oxidation of the sediment and salt formation on the sediment surface it is important that the sediment is scanned soon after it has been polished, but only when it is completely dry. Sometimes it is necessary to dry the sediment in an oven to speed up this process. Another problem can be the way in which a scanner or camera records colours. Often the brightest and darkest colours are registered with too low a contrast [33]. Luckily most sediment colours tend to fall within the middle range of colours (40 to 150) so this usually doesn't present too much of a problem. Finally it is important that the light used to scan or photograph the sediments under is diffuse and represents the whole colour spectrum. For this reason it is important to black out all other sources of light [33].

DSCA can't do everything and an intimate knowledge of the material under analysis is still required. It is a technique that is best used in conjunction with other techniques such as thin section analysis.

2.12.3 Sediment colour

Colour is an easily observed physical property of sediment and is often used to correlate different beds and layers in the field or in drill cores. The human eye registers colour in the visible light part of the electromagnetic wave spectrum between 380nm and 780nm wavelength.

Sediment colour is determined by the components making up the sediment and their chemical properties, such as oxidation state. Often sediment colour change can indicate change in sediment composition [43].

Computer based colour measurement can distinguish up to 2^{32} colours at its highest technological limit [156]. The majority of modern scanners have no problem scanning at a resolution greater than 1 measurement per millimetre, giving a reasonable sampling interval for most sediments. Schaaf (1995) [156], recommends converting colour measurements to greyscale for ease of processing. 256 different levels of grey are used to create a greyscale image file where 0 represents white and 255, black. Turning a colour record into greyscale removes one level of detail but it also helps to cut out some of the noise from the data.

2.12.4 Previous work

One of the first studies to utilize DSCA was that of Ripepe *et al* (1991) [141], where they used the greyscale record to measure varve thickness and identified ENSO and sunspot periodicities in the Eocene oil shale of the Green River Formation. Schaaf & Thurow (1994) refined and modified the technique of obtaining a digitized sediment colour record and managed to reduce the noise in the data and eliminate disturbances such as cracks and voids [155]. They applied DSCA to Holocene drill cores from the Santa Barbara Basin [155], [157], to yield time series with sub annual resolution. Schaaf gives a detailed explanation of DSCA in his PhD thesis [156].

Francus digitized optical and backscattered electron microscope photographs to measure grain size variation [54]. Bauch & Helmke (1999) looked at the correlation between greyscale and geochemical properties, such as total carbonate and total organic carbon [12]. They found little correlation in the glacial sediments that they were studying and concluded that carbonate corrosion in forams had a strong effect on the greyscale [12].

More recently Lindenberg & Ringberg (1999) [102], Petterson *et al* (1990) [131], and Nederbragt & Thurow (2001) [119], have used DSCA as a method of measuring varve thickness with great success. In addition Lindenberg & Ringberg (1999) [102], managed to use greyscale as a proxy for grain size. Excellent reviews of DSCA and its pitfalls and potentials have been written by Cooper (1998) [35], and Christensen & Björk (2001) [33].

3

Preparation methods and Data generation

3.1 Producing a record of sediment colour change

3.1.1 Cutting and polishing procedure

A complete 9.9m section with a polished surface was obtained using the following techniques.

Firstly the rocks were cut to provide a flat surface. An automatic saw was used which was lubricated with tap water only to avoid organic contamination. (Normally the saw is lubricated with a mixture of oil and water.) Since the rocks were fragile along their laminations it was important to cut them perpendicular to their laminations.

During the cutting process it was inevitable that some rocks broke. To maintain a continuous section the rocks were glued back together again using quick setting *Araldite*. The Araldite used contained the reactive ingredients Bisphenol A (epichlorhydrin), epoxy resin (number average molecular weight ≤ 700, alkylaminophenol and aminoether. A record was kept of all the regions that had been glued (Appendix A.1).

The next part of the preparation involved sanding the rocks to a fine finish. A hand held *Black & Decker* sander was used with three different grades of sandpaper: Coarse (60G), Medium (120G) and Fine (240G).

Finally, to get a smooth finish the surfaces were polished by hand using a method normally employed in making thin sections. A very fine powder of silicon carbide and aluminium oxide is mixed with water and made into a paste on a sheet of flat glass. The cut surface of the rock is then moved by hand in the paste, in a circular motion. The grades of powder used in this case were 600G followed by 1000G.

3.1.2 Scanning and digitisation of samples

The entire section was scanned on an ordinary flat bed scanner to produce a record of changes in colour throughout the section. Each piece was placed on the scanner glass with white card surrounding it. The scanner measures the reflection of light from the surface and gives this brightness a numerical value between 0 (white) and 255 (black). A dark cloth was placed over the lid to reduce light pollution from external sources and the rock was scanned at a resolution of 600ppi (pixels per inch). A high resolution was required because the laminae are extremely fine and very closely spaced. 600ppi was calculated to give a reasonable level of detail for this sediment and to be feasible in terms of time for scanning 10 metres of core. At the start of each scanning session a control specimen was scanned to ensure that all the results were comparable.

Image analysis was performed on a Macintosh computer using the public domain NIH Image program (developed by Wayne Rasband at the U.S. National Institutes of Health and available on the Internet at http://rsb.info.nih.gov/nih-image/). Five separate parallel greyscale profiles were extracted from each image (each of 8 pixels width to encompass a representative block of sediment) in a direction perpendicular to the laminations. Each line was chosen individually to avoid unrepresentative areas such as nodules or areas of salt precipitation. The five resulting files from each piece of rock were averaged to produce a representative greyscale for the whole piece of rock. This averaging procedure was necessary to prevent individual components (e.g. faecal pellets and forams) from dominating the greyscale signature.

3.1.3 Splicing and angle correction

To create a continuous section, the greyscale files from each piece had to be joined together. The precise amount of overlap between pieces was calculated (using lamina matching where possible) and the relevant amount of overlap was discarded. In addition some of the pieces had not been cut at exactly 90° to the lamina and consequently a simple length correction calculation was carried out before they were added to the continuous section. There were some places in the section where the exact amount of overlap could not be calculated due to bioturbation or lack of clear lamination. In these areas a best estimate of the overlap was made and the position noted. These are listed in Appendix A.2.

3.2 Producing a record of calcareous nannofossil variation

3.2.1 Nannofossil slide preparation

Samples were initially taken at 20cm intervals throughout the section to provide an overview of changes in nannofossil assemblages and preservation. In addition the first 6m of the section was sampled at 10cm intervals to see if any more information was gained from the closer sample spacing. The technique used to make the slides is as follows.

Prior to making each smear slide, the rock surface was scraped clean with a razor blade in order to eliminate any possibility of contamination from collection or storage. The sample was scraped from the fresh surface with a scalpel and approximately 0.5cm of laminae were smeared together. This method avoids sampling from only one or two faecal pellets and ensures that a representative sample is obtained for the resolution we are interested in. Sample size was measured by eye only, but an attempt was made to ensure the size of each sample was similar so that some semi-quantitative measurement of nannofossil density could be made. The sample was made into a suspension with distilled water of pH8. The suspension also contained triton, a detergent to disperse the particles and remove surface tension from the water. The suspension was put in an ultrasound bath for 2 minutes and then pipetted onto a cover slip. This was dried slowly on a hot plate at a temperature of 60°C. Finally the cover slip was glued to a slide with

Norland optical adhesive and fixed under an ultraviolet light.

3.2.2 Light microscope nannofossil counts

An Olympus BH-2 light microscope was used to observe and count the calcareous nannofossils from the slides. A DPlan 100 oil immersion objective lens and times 10 occulars were used, giving a total magnification factor of approximately 1000. For each slide the first 300 nannofossil specimens were identified along with the number of fields of view required to count 300 nannofossils. The number 300 was chosen with advice from Paul Bown and based on the sampling statistics calculated in Dennison and Hay (1967), [41]. Dennison and Hay show that for a random sample size of 300 specimens, the probability of failing to detect a species having an abundance of approximately 2 in every 1000, is 0.95 [41]. This figure was acceptable for the study being undertaken. Fragments of specimens of half or greater than their original size were included in the count. Counts were conducted in random traverses of the slide to ensure minimum bias from slide preparation. Results were recorded in an Excel spreadsheet. Nannofossil abundance was estimated using the parameter nannofossils per field of view [52].

Before counting commenced some of the species were grouped into generic classes due to the difficulty in recognising individual species, or to speed up the counting, or because of the dominance of one species. The groupings were as follows. *Biscutum ellipticum* (*Biscutum constans* of many authors) and *Biscutum salebrosum* were grouped together as *Biscutum* spp. *Eprolithus floralis*, *octopetalus* and *rarus* were grouped together under *Eprolithus floralis* as it was very difficult to recognise them individually and the vast majority of the specimens were, in any case, *Eprolithus floralis*. *Prediscosphaera cretacea*, *columnata* and *spinosa* were grouped together under the heading *Prediscosphaera* spp. Lastly all *Zeugrhabdotus* species were grouped together under the heading *Zeugrhabdotus* spp. due to the large number of very small (less than 2m in diameter) species that were very difficult to differentiate between.

3.2.3 Preservation of nannofossils

The preservation scale of Roth & Thierstein (1972) [149] as modified by Roth (1973) [145] was used. Etching was determined on a scale of 1 to 4. The majority of the Tarfaya samples fall into the well preserved category E1. This indicates there may be slightly jagged outlines of the more delicate forms, and delicate central structures may be damaged in some species, but that damage is no more significant than this. For example the delicate central bars in the species *Sollasites horticus* were almost always present in both SEM stubs and light microscope slides and exhibited very little overgrowth in either.

Evidence for good preservation throughout the section is further supported by the correlation coefficients between individual taxa. Many authors including Thierstein (1981) [176], Roth & Bowdler (1981) [147], Roth (1984) [146], and Roth & Krumbach (1986) [148] have agreed that *Watznaueria* sp. are generally solution resistant and that large percentages of *Watznaueria* sp. in an assemblage can indicate significant dissolution. Additionally Thierstein (1976) [175] considers *Eprolithus floralis* to be another solution resistant species. Hence if dissolution is significant correlations would be expected between these solution resistant species. The reverse is observed in the Tarfaya data with the correlation between *Watznaueria* sp. and *Eprolithus floralis* being negative ($\rho = -0.56$) as shown in Table 4.4.

3.2.4 SEM stub preparation

Stubs were prepared for the SEM (scanning electron microscope) by breaking off a piece of rock of approximately 1cm^3. The piece was mounted with the fresh surface facing uppermost onto an aluminium stub, using *Silver Dag* a conductive silver cement. It was coated with a gold layer using a Polaron E5000 splutter coater. The thickness of the gold layer was approximately 500 angstroms.

One of the main problems with making SEM stubs of the Tarfaya material was breaking the rock along a suitable lamina. It was extremely difficult to break the rock along a specific layer and often the rock tended to break along the more organic carbon rich layers. Many stubs were made, but it is felt that few of the stubs provided a representative cross section of the sediment due to the bias in where the rock was likely to break.

3.2.5 Quantitative techniques

Diversity analyses conducted included species richness (S), the Shannon-Weaver Diversity Index (H), and Equitability (E). Each of these are explained in the following paragraphs.

Species richness (S)

Species richness is simply the number of species recorded per sample. It is an estimate of the niche space size in the surface water phytoplankton communities [187]. In this case the species richness for each sample was number of species recorded from a light microscope 300 count. Throughout the rest of the text species richness is given the symbol S.

Equitability (E)

Equitability is a measure of the relative degree of dominance within a paleocommunity [187] and is calculated by finding the ratio between actual diversity and the maximum diversity possible given the species richness. Equitability has been viewed as the relative utilization of energy flux through the ecosystem by the organisms under consideration [187]. It is calculated using the following formula and requires prior calculation of the Shannon-Weaver diversity index which is explained in the next paragraph.

$$E = \frac{e^{(H(S))}}{S} \tag{3.2.1}$$

where E = equitability and H(S) = Shannon-Weaver diversity index.

Shannon-Weaver diversity index (H(S))

The Shannon-Weaver Diversity Index encompasses both species richness and equitability and it represents the level of uncertainty in a prediction that an individual chosen at random would belong to a particular species [164]. Therefore when H(S)

= 0 the sample is composed of only one species and H(S) is a maximum when every individual in the sample belongs to a different species. The equations for H(S) is given below.

$$H(S) = -\sum(p_i)(\ln p_i) \tag{3.2.2}$$

where $1 \leq i \leq S$, S = number of species, p = proportion (not percentage) of the i^{th} species in the slide.

The Shannon-Weaver diversity index is usually a number between 1.5 and 3.5 and is rarely above 4. It was chosen for this study for two main reasons as follows. Firstly it is quite a robust indicator with rare species having little effect on the diversity value. This tends to ameliorate the statistical problems resulting from limited (ie. ¡1000 specimens) counts. Secondly it has a sound mathematical foundation based on information theory [164].

High values of S, E and H(S) are indicative of assemblages which lived under stable conditions in which resources were efficiently and evenly divided amongst a relatively large number of species [187]. Conversely low values of S, E and H suggest unstable environmental conditions with dominance by a few taxa which utilised a disproportionately large share of the available resources [187].

Correlation co-efficients

Correlation co-efficients were calculated on an Excel spreadsheet using the CORREL function. This calculates how closely two sets of values are correlated using the formula below.

$$\rho_{xy} = \frac{\mathrm{Cov}(X,Y)}{\sigma_x \sigma_y} \tag{3.2.3}$$

where $-1 \leq \rho_{xy} \leq 1$ and

$$\mathrm{Cov}(X,Y) = \frac{1}{n}\sum(x_i - \mu_x)(y_i - \mu_y) \tag{3.2.4}$$

A more detailed explanation of this function is given in [64]. Throughout the text the correlation co-efficients are given the symbol ρ.

Nannofossil index of productivity (NIP)

A Nannofossil Index of Productivity (NIP) was computed as a proxy for productivity. It was calculated following the method of Eshet & Almogi-Labin (1996) [48] using the following formula.

$$NIP = \ln \frac{\text{High productivity regime species}}{\text{Low productivity regime species}} \tag{3.2.5}$$

A logarithmic scale is used to construct the NIP curve because it enables consistent recording of shifts in productivity at both high and low productivities. The logarithmic scale was similarly used by [135], [101], [47] and [48].

3.3 X-ray Fluorescence Spectroscopy

Two weeks were spent at the ODP core repository in Bremen, Germany, using the XRF scanning facilities there.

The basic principles of X-ray fluorescence scanning are as follows. A smooth sample surface is irradiated with X-rays at regular intervals. As the X-ray hits the sample it knocks electrons out of their orbit around the nuclei of atoms. Consequently an electron from an outer shell falls into the place of the missing electron. Outer shell electrons are more energetic than inner ones so the relocated electron has an excess of energy that is expended as an X-ray photon.

Elements have a unique X-ray signature which can be detected by the detector. The number of X-rays emitted can be counted to quantify the amount of a particular element in any one interval. Fig 3.1 illustrates the electron movement.

The specifications and procedures for the scanner are as follows. The central sensor unit consists of a molybdenum X-ray source (3 to 50kV) and a Peltier-cooled PSI detector (KEVEX^{TM}) with a 125$/mu$m Beryllium window and a multi-channel analyser with a 20eV spectral resolution. The polished rock surfaces were placed face up, all at the same height, in stratigraphic sequence inside the scanner. A very thin piece of polythene was placed over the rock surface to avoid contaminating the scanning foot with dust. The machine was programmed to take readings over an area of 4mm^2, every 2mm and the whole 10m section was processed in this way.

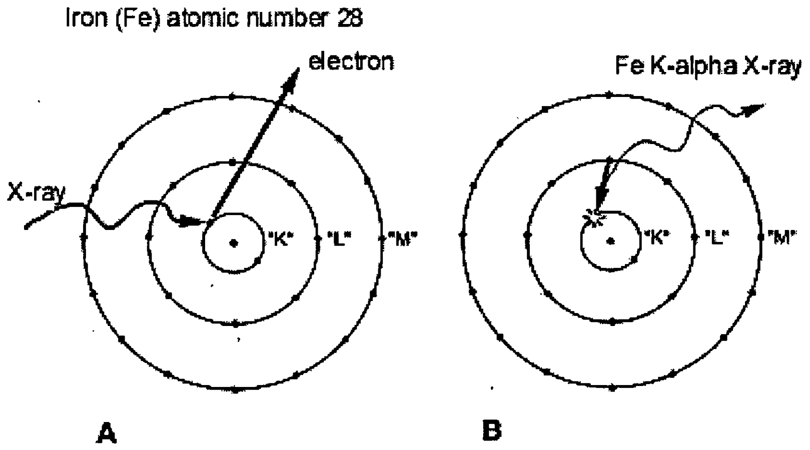

Figure 3.1: Diagram showing principle of X-ray fluorescence spectroscopy for the element Iron.

3.4 Geochemistry

3.4.1 Sample preparation

Samples were taken every 20cm throughout the section. However when the overlap between pieces was re-calculated (as explained in Appendix A.2) these samples were no longer evenly spaced. They were taken using a scalpel in the same way as the nannofossil smear slide samples and were taken from precisely the same places in the core as the nannofossil samples. Enough sample was removed to fill half a centimetre of the bottom of a standard test tube with powder. Once again the sample was homogenised over a depth of 1cm of sediment to avoid biasing the sample from individual lamina. They were processed by The Wolfson Laboratory for Environmental Geochemistry and measurements made of the percentage of total carbon, percentage of acid insoluble carbon and carbon as percentage calcium carbonate.

3.4.2 Estimating Silica content

Due to the nature of these marine sediments it was possible to make an estimate of the original Silica content. This was carried out by assuming that the sediment was originally made up from three main components: organic carbon, carbonate and silica. It was felt that this is a reasonable assumption to make as there is very little terrigenous material in the sediment. As described in section 2.1.3, the Tarfaya sediments contain strings of silicate nodules. Possibly the layers of silicified chalk may be intervals of strong radiolarian enrichment.

An estimate of original silica content was made using the measured percentages of organic carbon and carbonate. The following formula was used to calculate original silica percentage.

$$\text{Silica}\% = 100 - C_{\text{organic}}\% - C_{CaCO_3}\% \tag{3.4.6}$$

3.5 Thin section analysis

Petrographic 5cm by 7cm thin sections of the sediment were made by Dr. Christianne Street and Sean Houlding in the standard way. Three representative sampling areas were selected from the Tarfaya quarry core; an area of dark coloured sediment (from slab 11), an area of intermediate coloured sediment (from slab 4) and an area of light coloured sediment (from slab 0). Approximately five overlapping thin sections were made for each area, giving continuous coverage of around 20cm of core in each case. The thin sections are now archived at University College London, along with the Tarfaya core, in the care of Dr. Thurow. Estimates of changes in percentage of lithics, foraminifera, radiolarian, fish bone, organics and faecal pellets were obtained by carrying out point counts in thin sections. Additionally average lamina thickness relating to the colour of the sediment was estimated from the thin sections. In this instance a lamina describes a dark/light couplet comprising a layer of organics followed by a layer of faecal pellets.

4

Results

4.1 Geochemistry results

Appendix A.3 shows the values of total carbon C_{TOT}, carbon as calcium carbonate C_{CaCO_3}, and organic carbon $C_{organic}$ at various depths throughout the Tarfaya section. Note that $C_{organic}$ has a significant presence throughout and ranges in value between 1.99% and 17.8%. The down-core plot of these results is given in Fig 4.1.

Both $C_{organic}$ and C_{CaCO_3} exhibit a strong correlation with the greyscale record (Fig 4.2 and Fig 4.3) with correlation co-efficients of $\rho = 0.77$ and $\rho = -0.76$ respectively.

The contribution from Silica (Si) was estimated as explained in section 3.4.2 and these results are presented in the last column of the table in appendix A.3. Significant correlation is observed between %Si and greyscale (Fig 4.4) with a correlation co-efficient of $\rho = 0.65$.

4.2 XRF results

Unfortunately all the XRF results had to be discounted due to a problem with scan results over cracks in the rock. It was subsequently discovered that the XRF scanner foot would only work on a completely smooth surface with no cracks in it. The scanner foot required a complete 1cm sequence of rock to give accurate

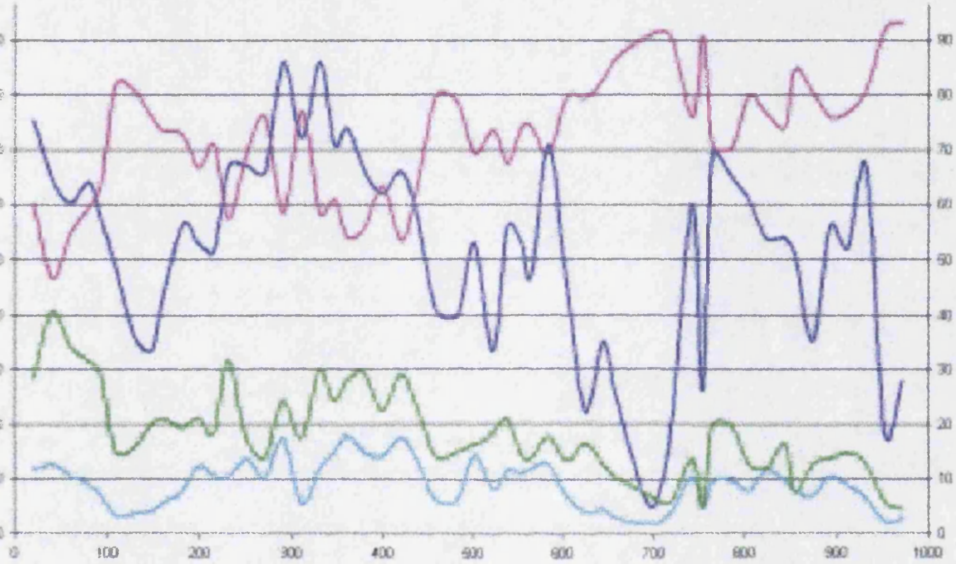

Figure 4.1: Down-core variation in geochemistry results. Bright blue = greyscale, Pink = C_{CaCO_3}, Sky blue = $C_{organic}$ and Green = %Si. x axis - depth in cm from core top, primary y axis - greyscale values, where higher numbers are darker colours, secondary y axis - percentage values of geochemistry results.

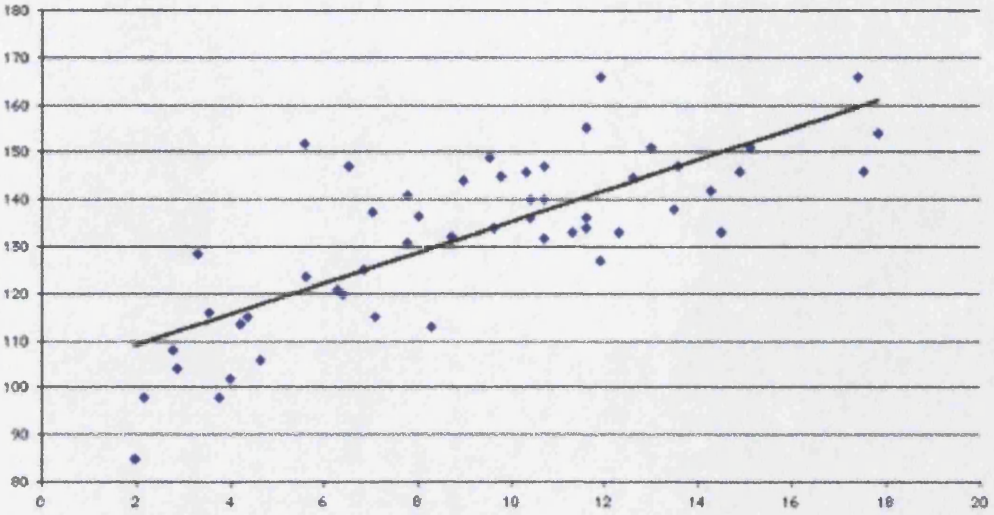

Figure 4.2: Scatter plot showing correlation between greyscale and $C_{organic}$ values, (y axis - greyscale values, where darker colours are higher numbers, x axis - % $C_{organic}$).

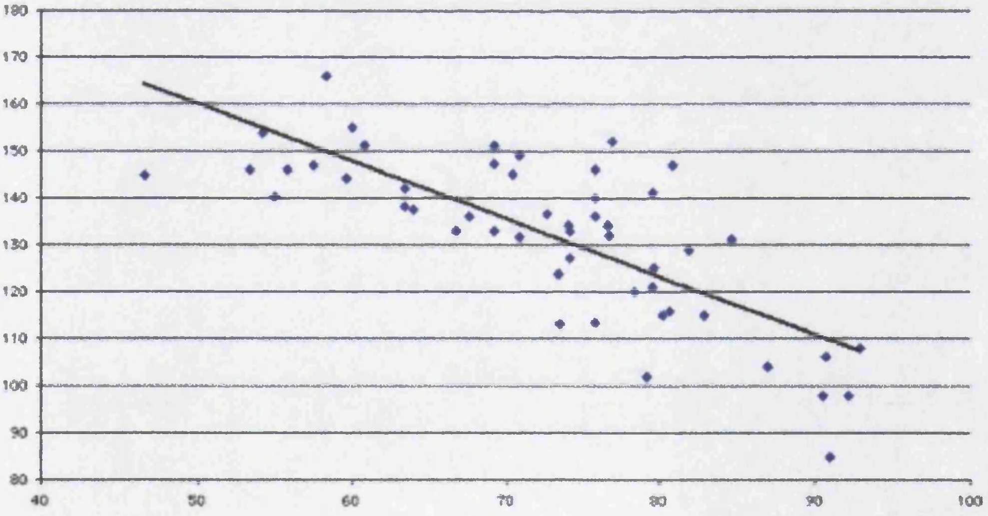

Figure 4.3: Scatter plot showing correlation between greyscale and C_{CaCO_3} values, (y axis - greyscale values, where darker colours are higher numbers, x axis - % C_{CaCO_3}).

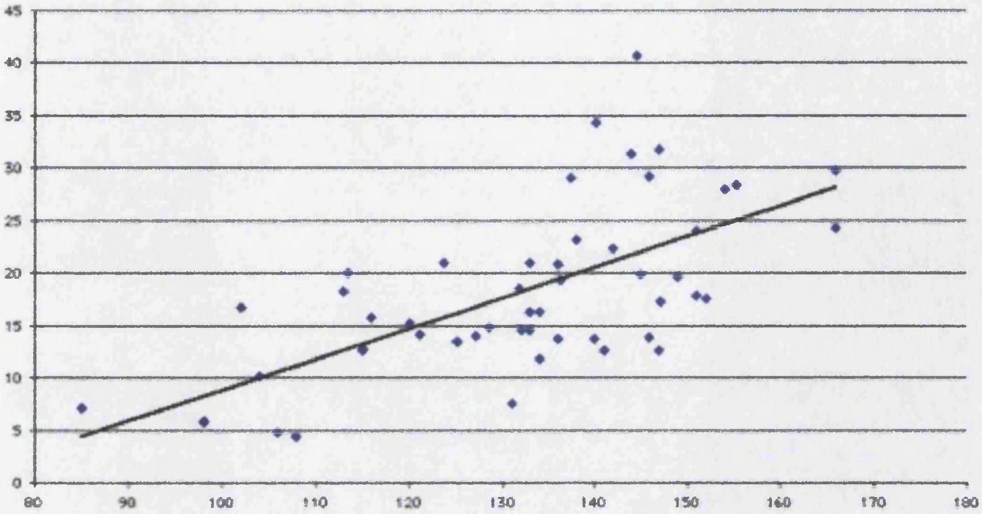

Figure 4.4: Scatter plot showing correlation between greyscale and estimated Si values, (y axis - greyscale values, where darker colours are higher numbers, x axis - estimated %Si.)

readings. This meant that the results were unreliable for 1cm either side of a crack and at the end of rock pieces. Fig 4.5 illustrates this problem by showing the calcium counts for a typical rock piece. At a number of places the calcium counts fall to zero as the scanner foot passes over a crack. Since all the rock pieces from the Tarfaya quarry are broken in a number of places it was not possible to construct a reasonable record from the XRF scan results. Simply removing the data from around the cracks, removes too much data to create a meaningful record. The data may still be useful for some high resolution analysis of the longer complete pieces, but it was not suitable for the purposes of this thesis.

4.3 Sediment colour change

There are two levels in the Tarfaya section where a small amount of bioturbation is seen. Small horizontal grazing traces are visible, indicating that the bottom waters must have become oxygenated for a short period of time. The bioturbated areas persist for a few centimetres in depth before returning to a laminated appearance. The rock pieces that the bioturbation occurs in are pieces 12D (between 231

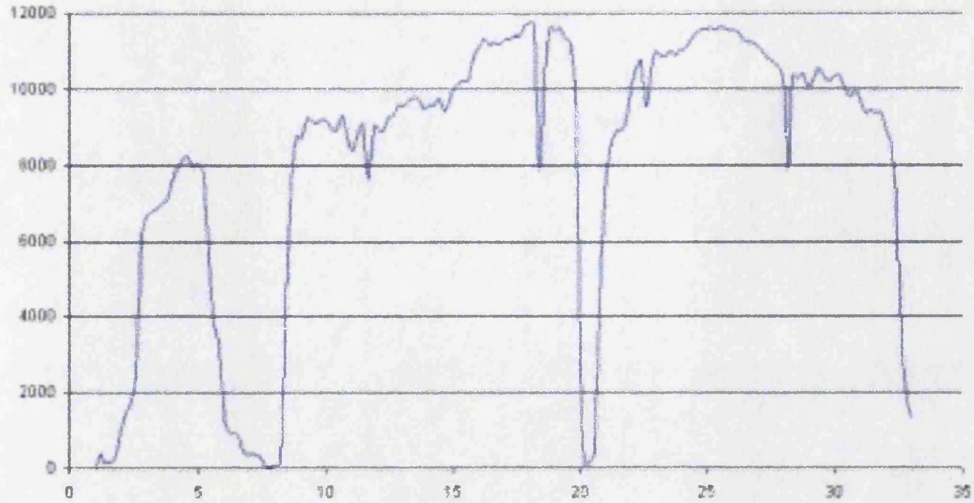

Figure 4.5: Graph of XRF Calcium counts for piece OD/E. (x axis - depth along piece in cm, y axis - Ca counts)

and 240cm depth approximately), along with the overlap between pieces 10D and 9D1/2 (between 375 and 380cm approximately). Figure C.5 in appendix C, illustrates the bioturbation in section 9D1/2.

Time series analysis was used to investigate most of the changes seen in sediment colour. However, it was also valuable to use some less sophisticated methods of analysis to get a feel for what the data represented. These are presented below.

4.3.1 Phase diagrams

Phase diagrams of the greyscale values were plotted with increasing numbers of offsets to observe the relatedness of adjacent greyscale measurements. In appendix C, figures C.6 to C.9 demonstrate the increase in disorder with increase in offsets for the greyscale values from 10cm of light sediment starting at 140cm depth. Figures C.10 to C.13 demonstrate the increase in disorder with increase in offsets for the greyscale values from 10cm of dark sediment starting at 300cm depth. Table 4.1 and Table 4.2 show the correlation coefficients for both light and dark sediment greyscale with increasing offset.

number of light greyscale offsets	coefficient, ρ
1	0.90
2	0.72
10	0.54
100	0.24

Table 4.1: Table of correlation coefficients for different light sediment greyscale offsets.

number of dark greyscale offsets	coefficient, ρ
1	0.95
2	0.86
10	0.72
100	0.48

Table 4.2: Table of correlation coefficients for different dark sediment greyscale offsets.

4.4 Matching with core S75

In 1975 BRPM (the Moroccan mining bureau) carried out a reconnaissance study of the Tarfaya oil shale deposit [99]. They drilled 26 shallow boreholes in an area stretching from Tarfaya to around 110km east. Figure 2.1 shows the location of some of these boreholes. Results from the borehole drillings remained confidential until the late 1990s. Following the release of the data Kuhnt *et al* carried out a comprehensive study of core S75 [92]. This included creating a greyscale record of the entire 94 metres of core.

For this thesis the greyscale from the Tarfaya quarry was matched with the greyscale record from core S75. The correlation interval was initially identified by trial and error matching the curves by eye.

Once the two overlapping areas of greyscale had been located, the quarry grey series had to be compressed by a factor of 20%, indicating that the sedimentation rate was 25% faster in the quarry part of the Tarfaya basin as compared to the location of core S75 (for locations see Fig 2.1). The match between the two greyscale curves is illustrated in Fig 4.6.

Kuhnt *et al* [92] found conclusive evidence for Milankovitch scale cyclicity in the Tarfaya exploration well sediments. By matching up the quarry greyscale with

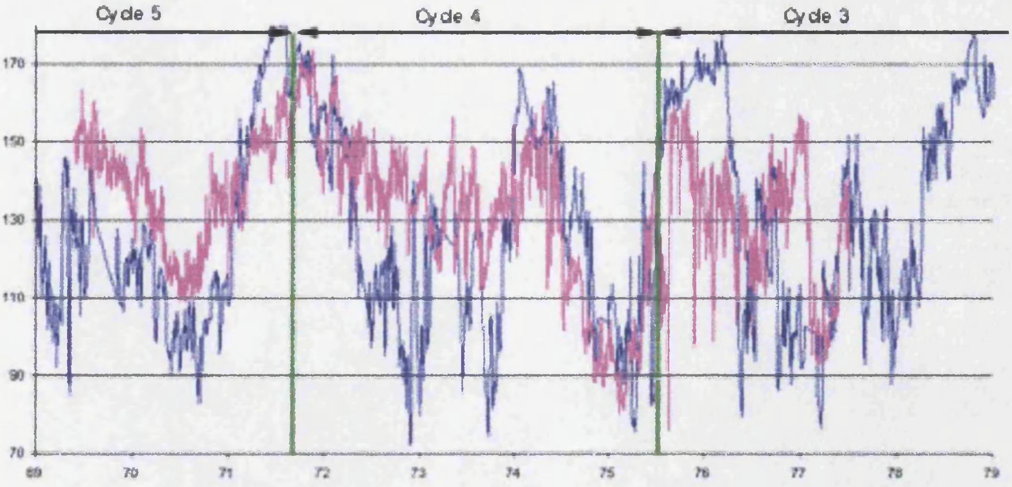

Figure 4.6: Matched greyscale for core S75 (blue) and the quarry (pink), obliquity cycles are marked using the same numbering as [105]. (y axis - greyscale values, where darker colours are higher numbers, x axis - depth in core S75 in metres.

that of core S75 it is possible to identify the Milankovitch cycles and obtain an estimate of sediment accumulation rate in the quarry sediments. The obliquity cycles are indicated on Fig 4.6. Using the same notation as Luderer 1999, the quarry sediments almost cover 3 complete obliquity cycles [105]. The upper part of cycle 3 is at the base of the sediments, cycle 4 in the middle and the start of cycle 5 at the top of the quarry. Cycle 4 covers approximately 4.5m of sediment. Rate of sedimentation for the quarry sediments can be estimated as follows.

$$\text{Quarry sediment accumulation rate} = \frac{4500mm}{39000years} = 0.115mm/year \qquad (4.4.1)$$

Table 4.3 shows the sediment accumulation rates calculated by Kuhnt et al [92], for the different oil exploration wells. The quarry sediment accumulation rate calculated above lies within the same range and indicates that it lay close to the depocentre of the Tarfaya basin in Cenomanian times.

Further calculations of sediment accumulation rates and an estimation of the amount of time represented by individual laminae can be found in section 4.7.4.

well number	sediment accumulation rate (mm/year)
S5, S21, S25, and S75	0.064 - 0.071
S20	0.087
S13	0.118

Table 4.3: Sediment accumulation rates in the different oil exploration wells.

4.5 Biostratigraphy and dating

As described in section 4.4, the quarry core was matched with core S75 using the greyscale record. Core S75 was dated using planktic foraminiferal biozonation and so it was possible to fit the quarry core into this timescale.

When dating the exploration wells Kuhnt *et al* [92] used the timescales of Obradovich 93 [124] and Gradstein et al 94 and 95 [62], [63]. S75 covers three global planktic foraminiferal zones during the interval between about 95.8 to 90.5 Million years ago. The bottom of S75 lies in the late Cenomanian *Rotalipora cushmani* Zone, next comes the *Whiteinella archaeocretacea* Zone covering the Cenomanian/Turonian boundary and finally the top of S75 lies in the early to middle Turonian *Helvetoglobotruncana helvetica* Zone. The pronounced positive $\delta^{13}C$ excursion occurs between the *Rotalipora cushmani* Zone and the *Whiteinella archaeocretacea* Zone.

The quarry core co-incides with S75 between the depths of 69.5 and 77.5m in core S75. This places the quarry core within the *Whiteinella archaeocretacea* Zone, above the $\delta^{13}C$ excursion and below the Cenomanian/Turonian boundary.

Due to the quarry core being so short there were few last occurrences and first occurrences of species and this made it difficult to place it in a nannofossil Zone. However, using the nannofossil zonation developed by Burnett [23], it was possible to determine that the quarry core lies in her nannofossil Zone Upper Cretaceous 5 (UC5). UC5 is defined by the last occurrence of *Lithraphidites acutus* to the last occurrence of *Helenea chiastia* (= *Microstaurus chiastius* of many authors). It ranges from the Upper Cenomanian to the Lower Turonian. Around the middle of UC5 the last occurrence of *Rhagodiscus asper* is observed. Since *Rhagodiscus asper* is recorded throughout the Tarfaya quarry core, this places it in the lower part of UC5.

4.6 Calcareous nannofossil counts

Light microscope counts revealed thirty two different species of calcareous nannofossil in the Tarfaya samples listed in appendix B.1. Six species are common (make up more than 1% of the nannofossil assemblage) throughout the sediment, while another six different species are periodically common in specific areas of the sediment. The remaining twenty species never make up more than 1% of the nannofossil assemblage. For the purposes of this study they are insignificant.

The six core taxa that are common throughout the sediment are *Biscutum ellipticum, Eiffellithus turriseiffelii, Eprolithus floralis, Prediscophaera* sp., *Watznaueria barnesae*, and *Zeugrhabdotus* sp.. The six species that are periodically common within the sediment are *Helicolithus turonicus, Lithraphidites carniolensis, Staurolithites laffittei, Sollasites horticus, Tranolithus orionatus* and *Tranolithus minimus.* Percentage abundances for all of the above species throughout the Tarfaya section are presented in Appendix B.2. Figure 4.7 shows the down core variation in the common species and figure 4.8 shows the down core variation in periodically common species.

A correlation is observed with greyscale values for certain species. In particular a significant correlation is seen for *S. horticus, T. orionatus* and *T. minimus.* All the correlation coefficients for common and periodically common species are presented in Table 4.4. Figures 4.9 to 4.20 show graphs of nannofossil variation with greyscale for all common and periodically common species.

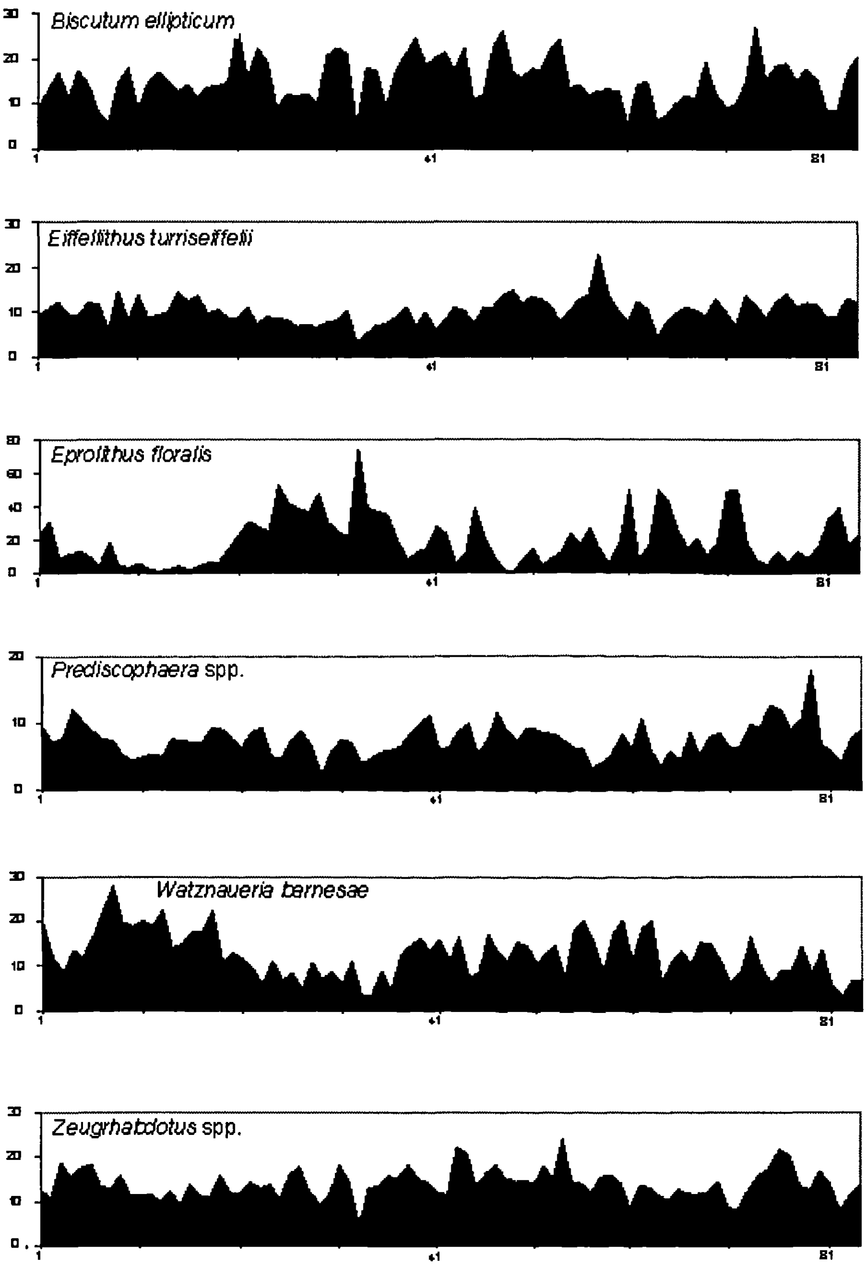

Figure 4.7: Down core variation in common nannofossil species. (y axis - percent abundance of nannofossil, x axis - sample number, where increase in number corresponds to increase in depth from top of the Tarfaya quarry)

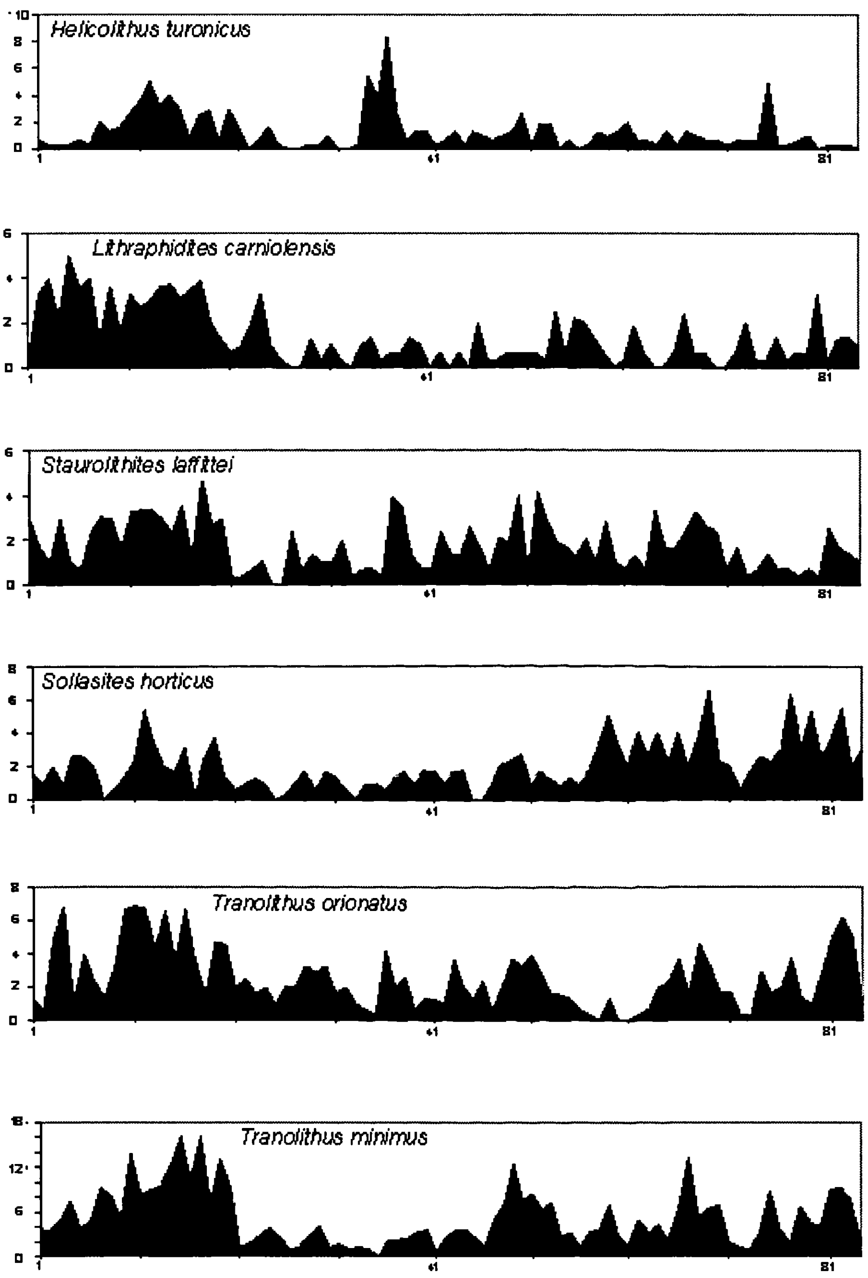

Figure 4.8: Down core variation in periodically common nannofossil species. (y axis - percent abundance of nannofossil, x axis - sample number, where increase in number corresponds to increase in depth from top of the Tarfaya quarry)

	Biscutum ellipticum	*Eiffellithus turriseiffeli*	*Eprolithus floralis*	*Helicolithus turonicus*	*Lithraphidites carniolensis*	*Prediscosphaera species*	*Sollasites horticus*	*Staurolithites laffittei*	*Tranolithus minimus*	*Tranolithus orionatus*	*Tranolithus summed*	*Watznaueria barnesae*	*Zeugrhabdotus species*
H(S)	0.22	0.56	-0.86	0.21	0.43	0.36	0.38	0.39	0.39	0.57	0.57	0.51	0.26
E	0.05	0.53	-0.80	0.28	0.41	0.36	0.42	0.48	0.41	0.62	0.61	0.53	0.22
greyscale	0.17	-0.25	0.26	-0.06	-0.06	0.03	-0.51	-0.31	-0.38	-0.53	-0.53	-0.11	0.13
organic carbon	0.41	-0.28	0.09	-0.15	-0.38	0.24	-0.28	-0.20	-0.51	-0.53	-0.58	-0.19	0.43
C as %CaCO3	-0.23	0.17	-0.05	0.07	-0.21	-0.08	0.47	0.22	0.27	0.41	0.41	0.00	-0.33
density	0.09	-0.18	0.33	-0.05	-0.12	-0.36	-0.06	-0.17	-0.25	-0.35	-0.35	-0.30	-0.04
B. ellipticum	1.00												
E. turriseiffeli	0.12	1.00											
E. floralis	-0.45	-0.61	1.00										
H. turonicus	-0.07	-0.10	-0.18	1.00									
L. carniolensis	-0.05	0.27	-0.42	0.15	1.00								
Prediscosphaera sp.	0.36	0.18	-0.45	-0.10	0.01	1.00							
S. horticus	-0.02	0.26	-0.32	-0.05	-0.02	0.15	1.00						
S. laffittei	-0.15	0.07	-0.36	0.21	0.19	-0.10	0.17	1.00					
T. minimus	-0.09	0.08	-0.34	0.23	0.30	-0.11	0.25	0.36	1.00				
T. orionatus	-0.16	0.31	-0.55	0.27	0.41	0.06	0.24	0.45	0.58	1.00			
Tranolithus summed	-0.15	0.26	-0.54	0.28	0.41	0.01	0.27	0.47	0.79	0.96	1.00		
W. barnesae	-0.09	0.27	-0.56	0.11	0.38	0.02	0.06	0.41	0.08	0.32	0.27	1.00	
Zeugrhabdotus sp.	0.48	0.26	-0.47	-0.12	0.01	0.42	0.02	-0.05	-0.02	-0.16	-0.12	-0.03	1.00

Table 4.4: Table of correlation co-efficients for all predominant and periodically predominant nannofossil species. Significance threshold for the correlation coefficient - $p < 0.05$.

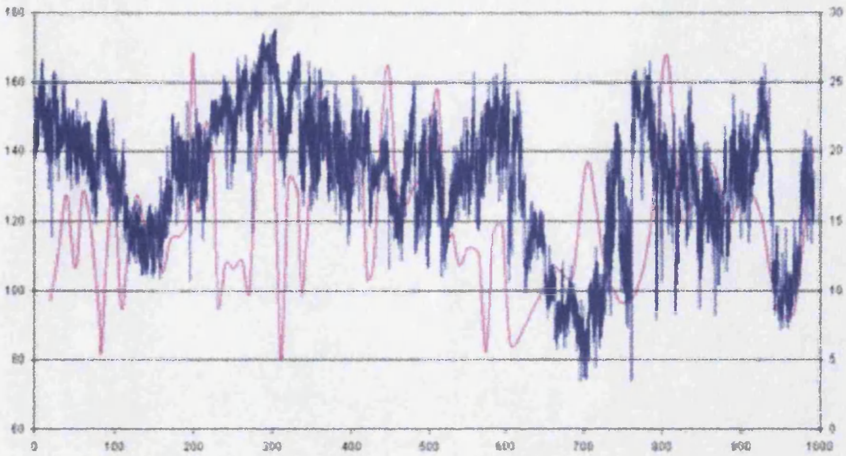

Figure 4.9: Variation in greyscale (blue) and *Biscutum ellipticum* (pink). Primary y axis - greyscale values where higher numbers are darker colours, Secondary y axis - percent abundance of nannofossil, x axis - depth/cm from top.

As explained in section 3.2.5, diversity of nannofossils was calculated using the Shannon Weaver diversity index (H(S)) and Equatability (E). Values of H(S) and E for each sample are given in Appendix B.3, along with down core plots of the values.

Correlation coefficients for each of the major nannofossil species with both H(S) and E are presented in Table 4.4. Of note are the high correlation coefficients for *E. floralis* of $\rho = -0.86$ with H(S) and $\rho = -0.8$ with E.

Productivity indicator species were interpreted from the above results. A discussion of the evidence for productivity indicator species is presented in section 6.4. *E. floralis* showed signs of being an indicator of extreme productivity conditions while *S. horticus* and *T. orionatus* appeared to correlate with moderate to high productivity conditions. The interplay between these species is shown in Fig 4.21. A Nannofossil Index of Productivity (NIP) was calculated for each sample using the method described in section 3.2.5. In this case the equation was as follows.

$$\mathrm{NIP} = \log \frac{\textit{Eprolithus floralis}}{\textit{Sollasites horticus} + \textit{Tranolithis orionatus}} \tag{4.6.2}$$

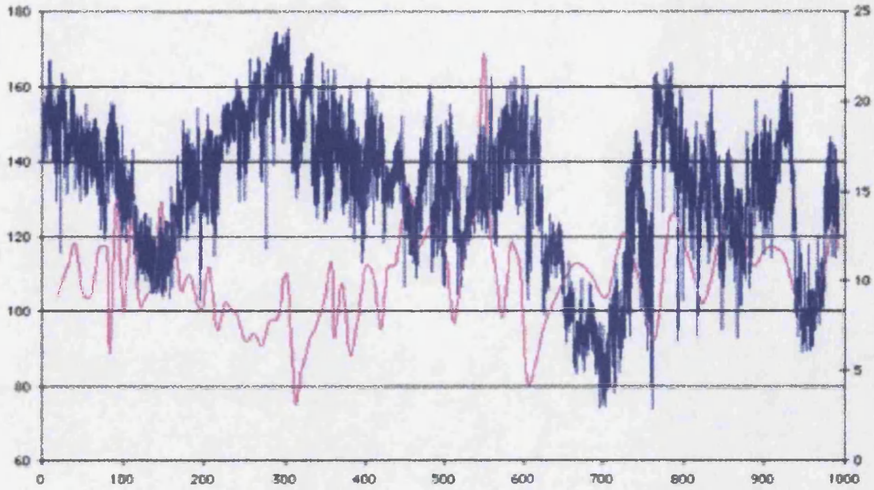

Figure 4.10: Variation in greyscale (blue) and *Eiffellithus turriseiffelii* (pink). Primary y axis - greyscale values where higher numbers are darker colours, Secondary y axis - percent abundance of nannofossil, x axis - depth/cm from top.

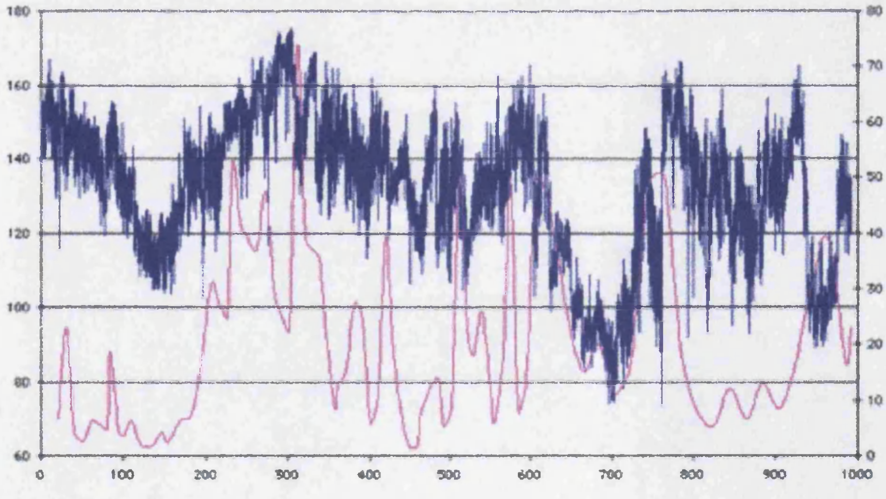

Figure 4.11: Variation in greyscale (blue) and *Eprolithus floralis*(pink). Primary y axis - greyscale values where higher numbers are darker colours, Secondary y axis - percent abundance of nannofossil, x axis - depth/cm from top.

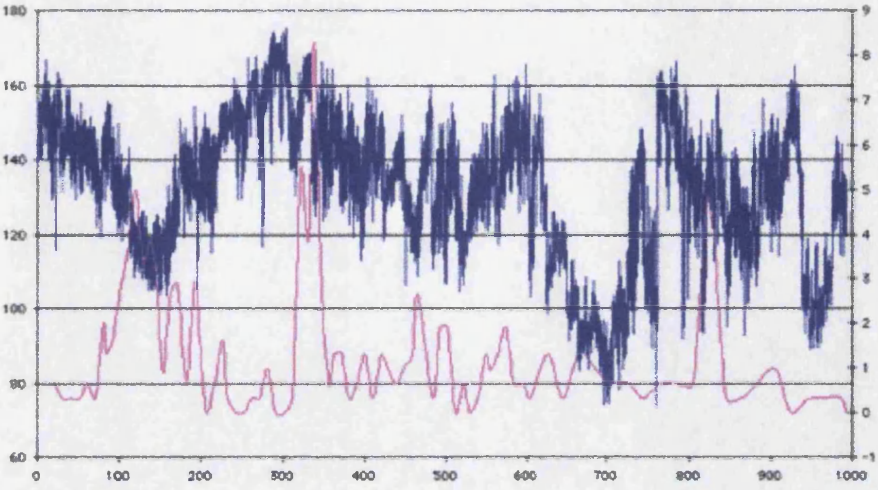

Figure 4.12: Variation in greyscale (blue) and *Helicolithus turonicus* (pink). Primary y axis - greyscale values where higher numbers are darker colours, Secondary y axis - percent abundance of nannofossil, x axis - depth/cm from top.

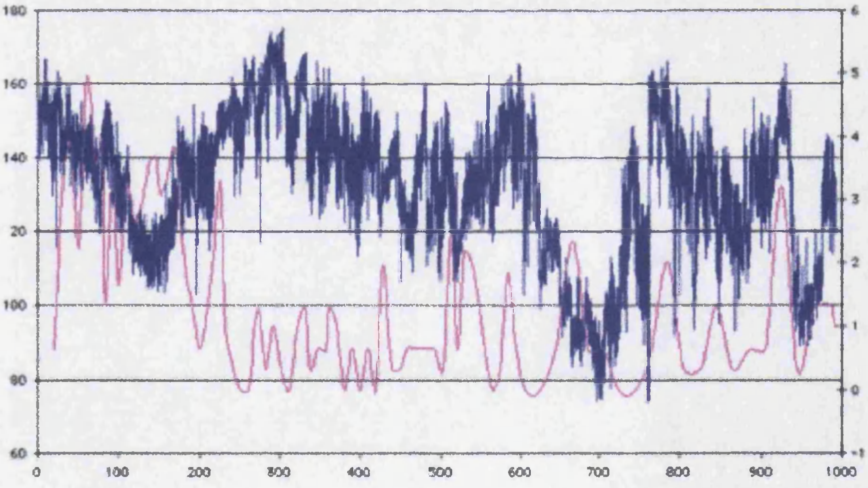

Figure 4.13: Variation in greyscale (blue) and *Lithraphidites carniolensis* (pink). Primary y axis - greyscale values where higher numbers are darker colours, Secondary y axis - percent abundance of nannofossil, x axis - depth/cm from top.

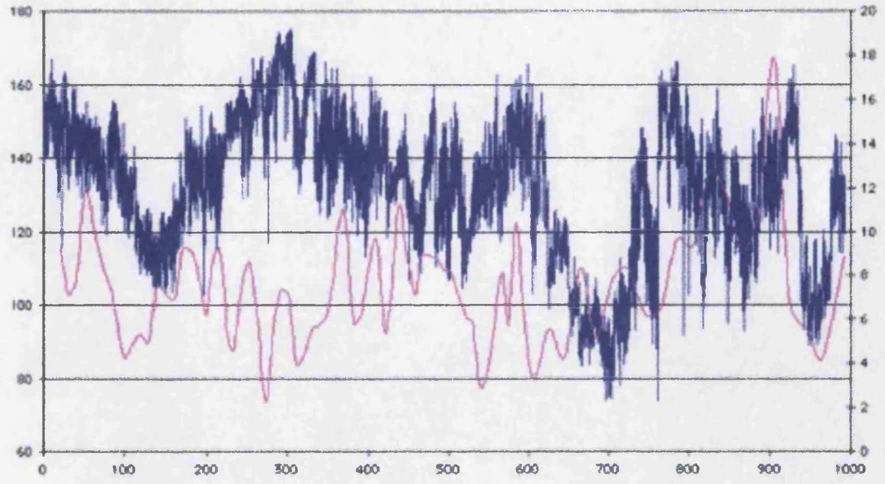

Figure 4.14: Variation in greyscale (blue) and *Prediscophaera* sp. (pink). Primary y axis - greyscale values where higher numbers are darker colours, Secondary y axis - percent abundance of nannofossil, x axis - depth/cm from top.

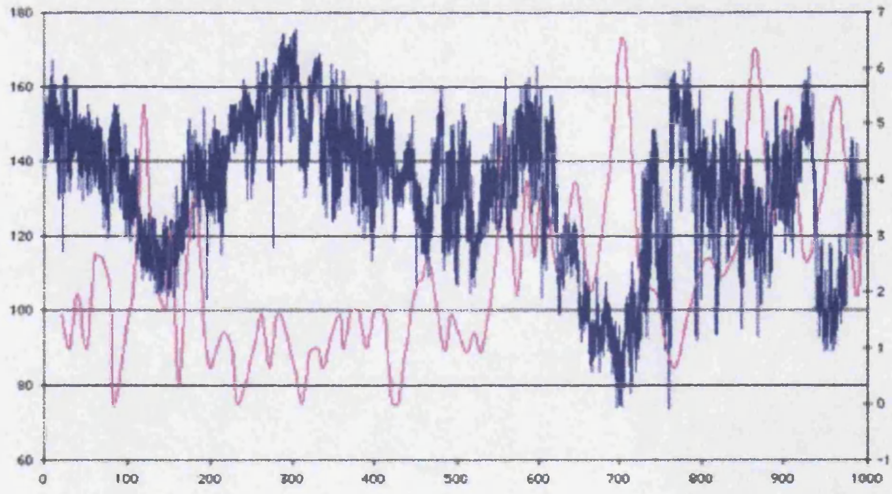

Figure 4.15: Variation in greyscale (blue) and *Sollasites horticus* (pink). Primary y axis - greyscale values where higher numbers are darker colours, Secondary y axis - percent abundance of nannofossil, x axis - depth/cm from top.

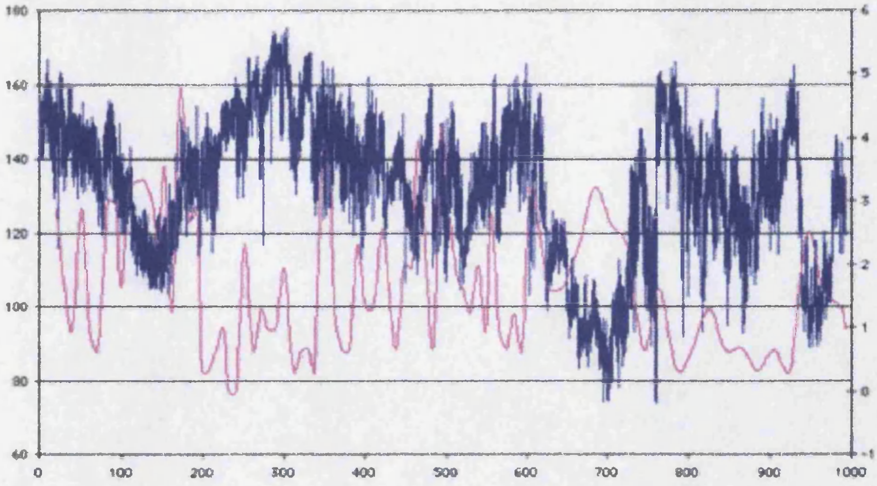

Figure 4.16: Variation in greyscale (blue) and *Staurolithites laffittei* (pink). Primary y axis - greyscale values where higher numbers are darker colours, Secondary y axis - percent abundance of nannofossil, x axis - depth/cm from top.

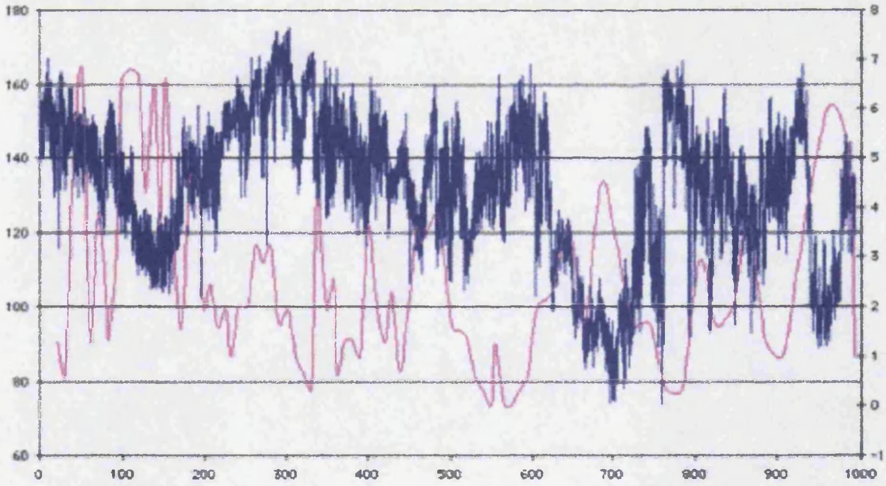

Figure 4.17: Variation in greyscale (blue) and *Tranolithus minimus* (pink). Primary y axis - greyscale values where higher numbers are darker colours, Secondary y axis - percent abundance of nannofossil, x axis - depth/cm from top.

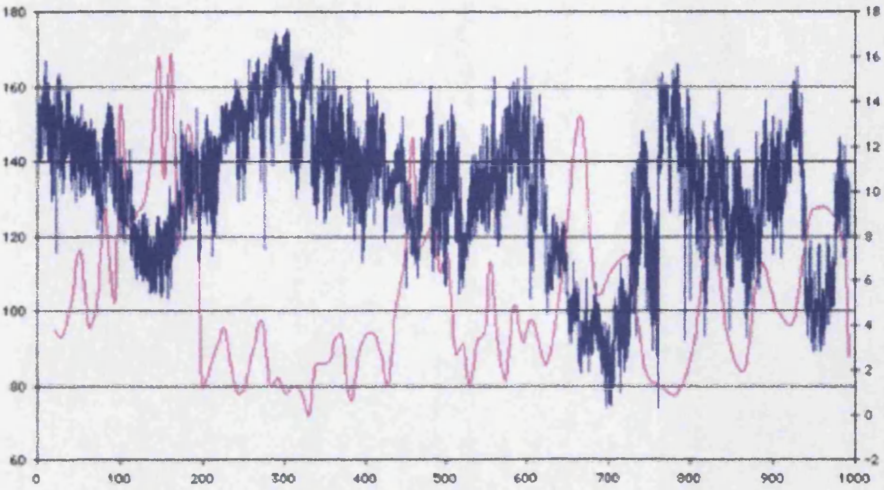

Figure 4.18: Variation in greyscale (blue) and *Tranolithus orionatus* (pink). Primary y axis - greyscale values where higher numbers are darker colours, Secondary y axis - percent abundance of nannofossil, x axis - depth/cm from top.

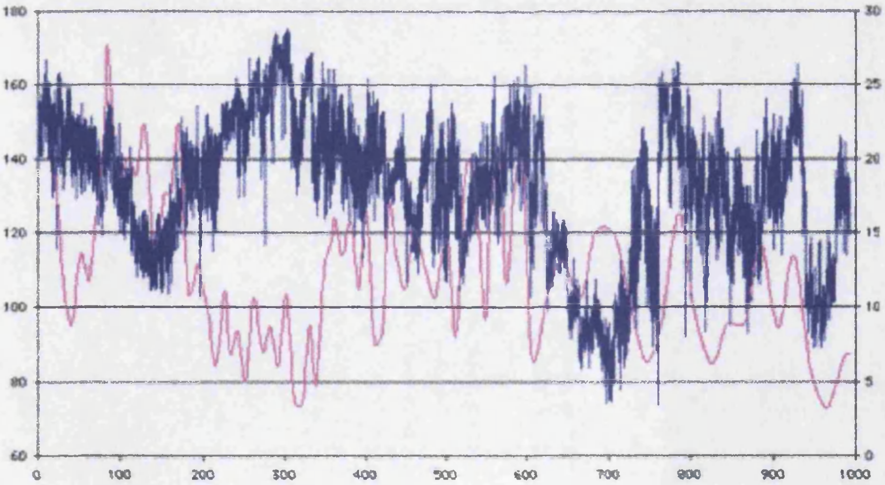

Figure 4.19: Variation in greyscale (blue) and *Watznaueria barnesae* (pink). Primary y axis - greyscale values where higher numbers are darker colours, Secondary y axis - percent abundance of nannofossil, x axis - depth/cm from top.

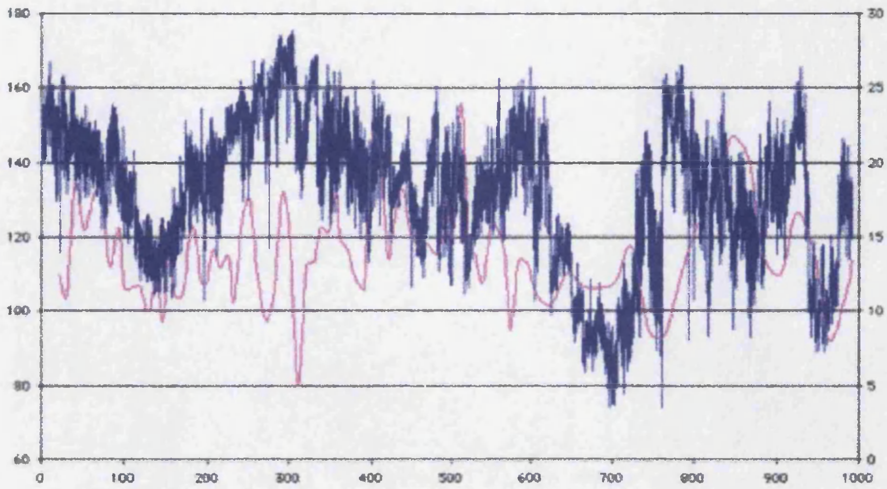

Figure 4.20: Variation in greyscale (blue) and *Zeugrhabdotus* sp. (pink). Primary y axis - greyscale values where higher numbers are darker colours, Secondary y axis - percent abundance of nannofossil, x axis - depth/cm from top.

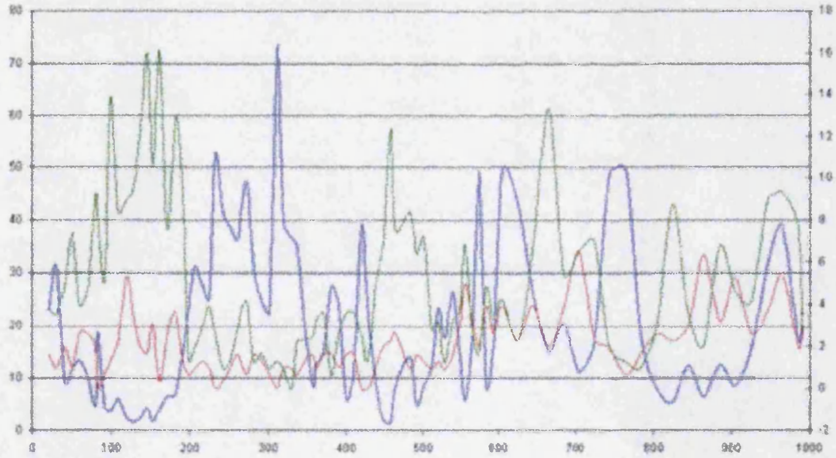

Figure 4.21: Interplay between the three main productivity indicator nannofossil species. Primary y axis - *Eprolithus floralis* percentage abundance (blue), Secondary y axis - *Tranolithus orionatus* (green) and *Sollasites horticus* (red) percentage abundance, x axis - depth/cm from top.

correlation between	coefficient, ρ
greyscale and H(S)	-0.29
greyscale and E	-0.43
NIP and H(S)	-0.75
NIP and E	-0.78
H(S) and $C_{organic}$	-0.12
H(S) and C_{CaCO_3}	0.09
E and $C_{organic}$	-0.22
E and C_{CaCO_3}	0.21
greyscale and NIP	0.48
NIP and nanno density	0.37
nanno density and H(S)	-0.3
nanno density and E	-0.4
greyscale and $C_{organic}$	0.75
greyscale and C_{CaCO_3}	-0.77
C_{CaCO_3} and $C_{organic}$	-0.8

Table 4.5: Table of correlation coefficients between Tarfaya proxy indicators.

The NIP results are given in Appendix B.3, along with a down core plot of the values. Correlation coefficients for NIP with H(S), E greyscale and nannofossil density were calculated and these are shown in Table 4.5.

4.7 Thin section results

Point counts of the thin sections allowed the Tarfaya sediment to be classified into three broad categories: light sediment, intermediate coloured sediment and dark sediment (see figure ?? for where these categories occur in the section). Each is described below with point counts from a typical representative slide. By counting the number of laminae per mm it was possible to estimate the sediment accumulation rate and speculate on the amount of time that one lamina represents (section 4.7.4).

4.7.1 Dark sediment

Overall preservation was good, with foraminifera walls still intact and very few broken chambers. Slide 11B2A is typical of the dark sediment. Figures 4.22 to

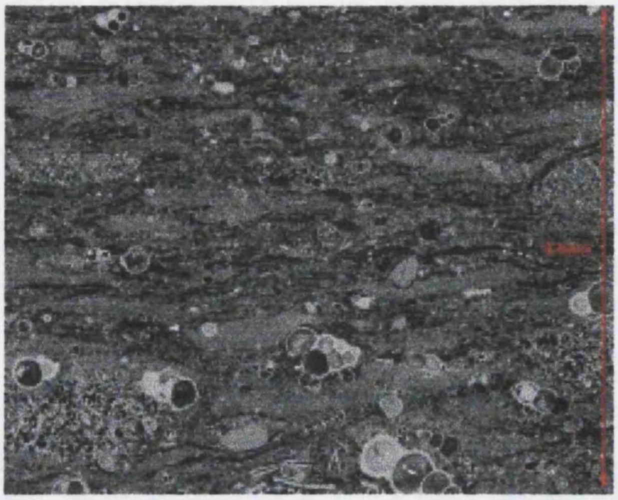

Figure 4.22: Typical image of dark sediment from rock slab 11. In the bottom left of the image an *Eprolithus floralis* rich faecal pellet can be seen (the close up image of the pellet reveals the classic blocky, reflective shape of *Eprolithus floralis*). The scale of the image is 600μm from top to bottom. Taken on the Southampton BSEM by Dr. Richard Pearce.

4.25 show typical BSEM images of the dark sediment, including a close up of the inside of a faecal pellet. The average characteristics observed in one field of view (diameter 2mm) are described in the following list.

Foraminifera - between 80 and 150, dominated by *Heterohelix moremani*.

Foraminifera sizes - one or two large foraminifera with largest chamber diameter 150μm. Average chamber diameter around 30μm.

Radiolarian - extremely rare, none observed in slide 11B2A

Laminae - between 40 and 50 light/dark couplets. Individual layers of faecal pellets and foraminifera alternated clearly with individual layers of dark organic matter. This suggested fairly abrupt phytoplankton bloom events with a short seasonal duration. The overall appearance of these laminae was of a dark layer with distinct thin light bands contained within it.

Bivalves and/or ostracods - between 10 and 40. A few fragments of *Inoceramus* and many very thin, unidentifiable shells. Orientated along the lines of laminae, occurring throughout the slide. Assuming bottom waters were anoxic, these bivalves would have been surface dwellers.

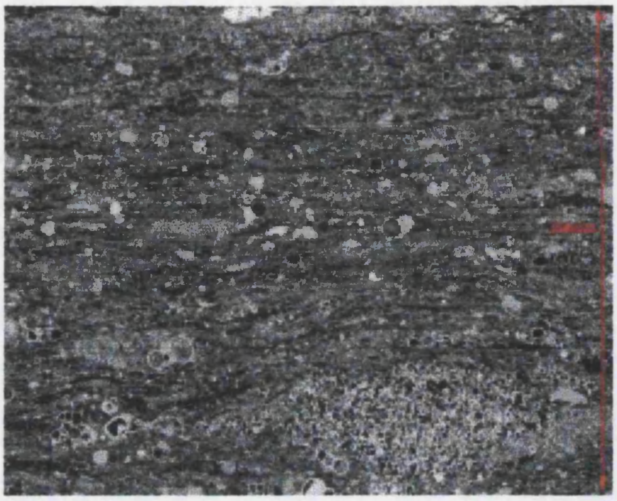

Figure 4.23: Typical image of dark sediment from rock slab 11. The laminae are slightly thinner than in Fig 4.22. In the bottom right of the image an *Eprolithus floralis* rich faecal pellet can be seen. The scale of the image is 600μm from top to bottom. Taken on the Southampton BSEM by Dr. Richard Pearce.

Figure 4.24: A slightly lighter area within the dark sediment from rock slab 11. In the bottom right bivalve remains can be seen. The scale of the image is 600μm from top to bottom. Taken on the Southampton BSEM by Dr. Richard Pearce.

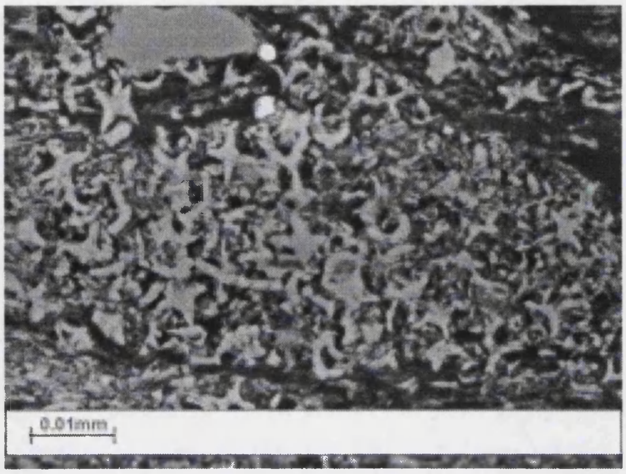

Figure 4.25: A close up image of the inside of an *Eprolithus floralis* rich faecal pellet. Scale bar 10μm. Taken on the Southampton BSEM by Dr. Richard Pearce.

Faecal pellets - varies between faecal pellet rich and faecal pellet poor areas. The largest faecal pellets have dimensions of approximately 600μm by 200μm. The average faecal pellet size is around 150μm by 20μm. Many of the faecal pellets in the dark sediment were composed predominantly from *Eprolithus floralis.*

Average percentage of organic carbon - 40 to 60%.

Average percentage of faecal pellets - 10 to 30%.

Average percentage of foraminifera, radiolarian and bivalves - 30%.

4.7.2 Intermediate coloured sediment

Preservation was not as good as for the dark sediment. Foraminifera walls were rarely preserved. Nonetheless it was still possible to identify different types of foraminifera. Slide 4A3 is typical of intermediate coloured sediment. The average characteristics observed in one field of view (diameter 2mm) were as follows.

Foraminifera - between 30 and 40, dominated by *Heterohelix moremani*, but also some *Heterohelix globulosa* present.

Foraminifera sizes - one or two large foraminifera with largest chamber diameter 150μm. Average chamber diameter around 50μm.

Radiolarians - extremely rare, none observed in slide 4A3

Laminae - between 25 and 35 light dark couplets. Moderately well defined layers of faecal pellets and foraminifera alternating with dark organic matter. However layers were not always distinct.

Bivalves - a few thin bivalve shells seen, however these could also have been slices of foraminifera chamber. No definite observations of bivalve shell.

Fish scales - a few, thin, honey coloured fish scales observed throughout this slide.

Faecal pellets - varies between faecal pellet rich and faecal pellet poor areas. The largest faecal pellets have dimensions of approximately 700μm by 150μm. The average faecal pellet size is around 150μm by 50μm.

Average percentage of organic carbon - 10 to 30%.

Average percentage of faecal pellets - 50 to 60%.

Average percentage of foraminifera, radiolarian and bivalves - 20 to 30%.

4.7.3 Light sediment

Preservation similar to intermediate coloured sediment. Slide 0C2 is typical of light coloured sediment. Figures 4.26 and 4.27 show typical BSEM images of the light sediment, unfortunately they are so bright that the images are over-exposed. The average characteristics observed in one field of view (diameter 2mm) are described in the following list.

Radiolarians - around 20 spherical forms, with spongeous internal structure, a probable indication of a high latitude/cold water dweller. However preservation was not good enough to identify the species. No original silica remained and they were all replaced by calcite.

Radiolarian size - around 100μm diameter.

Foraminifera - between 40 and 60, predominantly *Heterohelix moremani*, but also some *Heterohelix globulosa* and *Whiteinella* sp. present.

Foraminifera sizes - Average chamber diameter around 30μm.

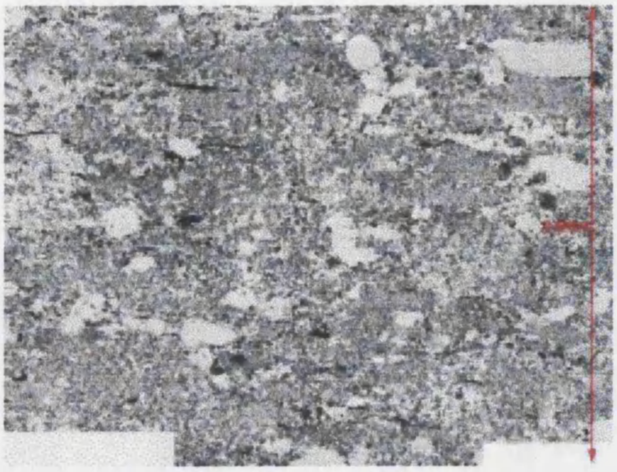

Figure 4.26: Typical image of light sediment from rock slab 0. The bright areas are foraminifera, radiolarian and faecal pellets. The lamina structure is not visible at this scale. The scale of the image is 600μm from top to bottom. Taken on the Southampton BSEM by Dr. Richard Pearce.

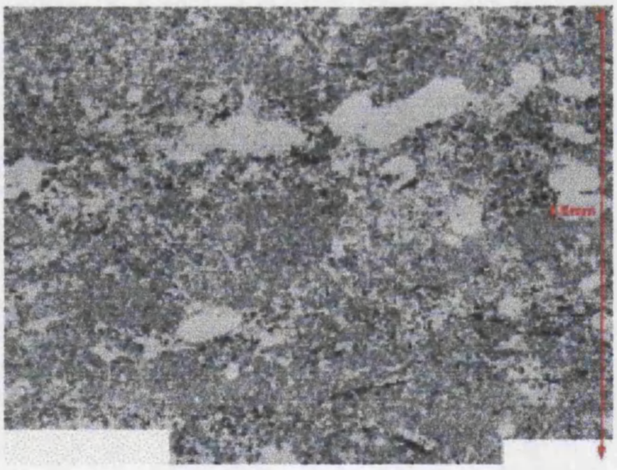

Figure 4.27: Typical image of light sediment from rock slab 0. In this image a hint of the lamina structure is visible in the row of faecal pellets across the top of the image. The scale of the image is 600μm from top to bottom. Taken on the Southampton BSEM by Dr. Richard Pearce.

Laminae - between 20 and 25 light dark couplets. Again moderately well defined layers of faecal pellets and foraminifera alternating with dark organic matter, but the layers were not always laterally continuous for more than a few centimetres.

Bivalves - one *Inoceramus* seen, but otherwise bivalves appear to be extremely rare in this environment.

Faecal pellets - varies between faecal pellet rich and faecal pellet poor areas. The largest faecal pellets have dimensions of approximately 1000μm by 300μm. The average faecal pellet size is around 300μm by 100μm.

Average percentage of organic carbon - 5%.

Average percentage of faecal pellets - 50 to 65%.

Average percentage of foraminifera, radiolarian and bivalves - 30 to 45%.

4.7.4 Sediment accumulation rates

It is likely that sediment accumulation rates varied over time with differing environmental conditions. If it is assumed that one lamina (light/dark couplet) always represents the same amount of time, then the variation in thickness of laminae from light to dark sediment suggests either differing sedimentation rates or differing amounts of sediment compaction after burial. Of course one lamina may not always represent the same amount of time and it is possible that lamina in the dark sediment represent a different event to those in the light sediment.

To take this into consideration a number of calculations were carried out to calculate sediment accumulation rate using four different scenarios. Firstly the quarry greyscale record was divided into blocks of dark, intermediate and light sediment, using cutoffs of 110 and 140 on the greyscale range. These blocks are illustrated in Fig 4.28.

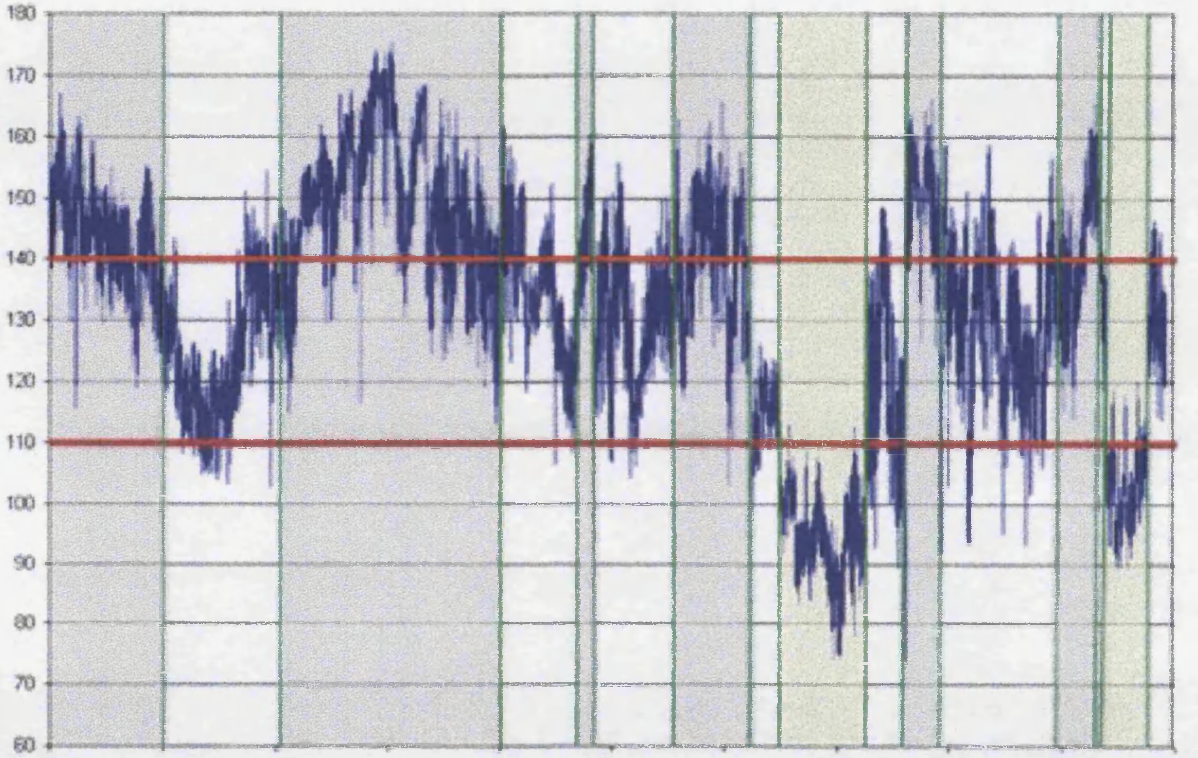

Figure 4.28: Tarfaya greyscale record divided into blocks of dark (grey), intermediate (white) and light (cream) sediment. The red lines indicate the greyscale cutoffs for each colour band. (x axis - depth in cm from the top of the quarry, y axis - greyscale where higher numbers are darker colours.)

From Fig 4.28 the length of each dark, intermediate and light block was measured and the number of laminae in that block estimated using the average number of laminae counted per field of view in the thin sections. The average number of laminae per cm estimated from the thin sections were as follows.

dark - 225

intermediate - 150

light - 125

Four sedimentation scenarios were considered as follows.

Scenario 1 - all lamina represent one year of sedimentation, possibly an annual bloom followed by continuous light sedimentation for the remainder of the year.

Scenario 2 - In the intermediate and light coloured sediment one lamina represents one year of sedimentation, while in the dark coloured sediment two laminae represent one year of sedimentation (possibly a spring and then autumn bloom).

Scenario 3 - Two lamina represent one year of sedimentation for all sediment colours (perhaps a spring and then autumn bloom scenario).

Scenario 4 - For intermediate and dark sediment one lamina represents one year, while in the light sediment two laminae represent one year of sedimentation.

Table 4.6 shows the calculation of sediment accumulation rate for each scenario. All the different scenarios give sediment accumulation rates within the same order of magnitude as those calculated in section 4.4. The closest sediment accumulation rate to that calculated in equation 4.4.1 comes from scenario 3, where two lamina represent a year for all colours of sediment.

The estimated sedimentation rates for the Cenomanian Tarfaya Basin are comparable to and within the same order of magnitude as other high sediment flux areas from anoxic hemi-pelagic and pelagic ocean basins. Leckie *et al* computed the sedimentation rate for the Pleistocene-Holocene Cariaco Basin (Site 1002) and the Cenomanian-Seronian La Luna-Querecual Formation (north Venezuela) [98]. The Cariaco series had a sedimentation rate of 0.128mm/year, while the La Luna Formation had a sedimentation rate of 0.013mm/year. It is thought that the higher sedimentation rate for the Cariaco series was due to enhanced land erosion due to block faulting in the Venezuelan Andes and Guyanese Craton, plus a lower sea level [98].

Given that the Tarfaya sediments have undergone some degree of compression, the actual sedimentation rate will have been higher still than the calculated rate and represents a very high sediment flux for this kind of basin. It suggests that productivity must have been very high to maintain such a flux.

	block colour	block thickness/cm	number of lamina	Scenario 1/years	Scenario 2/years	Scenario 3/years	Scenario 4/years
	dark	100	22500	22500	11250	11250	22500
	intermediate	104	15600	15600	15600	7800	15600
	dark	196	44100	44100	22050	22050	44100
	intermediate	70	10500	10500	10500	5250	10500
	dark	12	2700	2700	1350	1350	2700
	intermediate	80	12000	12000	12000	6000	12000
	dark	58	13050	13050	6525	6525	13050
	intermediate	30	4500	4500	4500	2250	4500
	light	75	9375	9375	9375	4687.5	4687.5
	intermediate	33	4950	4950	4950	2475	4950
	dark	35	7875	7875	3937.5	3937.5	7875
	intermediate	99	14850	14850	14850	7425	14850
	dark	43	9675	9675	4837.5	4837.5	9675
	intermediate	5	750	750	750	375	750
	light	35	4375	4375	4375	2187.5	2187.5
	intermediate	16	2400	2400	2400	1200	2400
Total		991	179200	179200	129250	89600	172325
Sedimentation rate mm/yr				**0.055**	**0.077**	**0.111**	**0.058**

Table 4.6: Calculation of sediment accumulation rates for the Tarfaya quarry sediments under four different scenarios.

4.8 Electron microscope work

Dr. Richard Pearce from the School of Ocean and Earth Science at the University of Southampton, carried out some independent research, studying parts of the Tarfaya sediment under the backscatter scanning electron microscope (BSEM). This work is ongoing but the most interesting finding so far has been a layer of *E. floralis*, (see Fig 4.29).

At University College London, five scanning electron microscope (SEM) stubs were taken from the following places in the Tarfaya section. It would have been interesting to have studied a greater number of stubs under the SEM, but unfortunately it was difficult to break off appropriate pieces of rock to make stubs and the process was very destructive to the core. Hence it was decided to concentrate on five areas of interest.

T1 - from the top of piece 15D4, a faecal pellet layer in dark sediment

T2 - from the top of piece 14C, a light area of sediment

T3 - from the bottom of piece 13A1, a bioturbated, non laminated, intermediate coloured area

T4 - from the bottom of piece 11E1/2, a dark laminated area

T5 - from the bottom of piece 8J, another dark laminated area

Each stub was studied in a qualitative way, noting the preservation of nannofossils, predominant species and their spatial distribution over the surface. The next five sections describe each stub in turn.

The images from the SEM are of rather a disappointing quality. It is thought that this may have been due to charging problems with the SEM at University College London.

4.8.1 Stub T1 - faecal pellets in dark sediment

Preservation of calcareous nannofossils was good with delicate structures still preserved. For example the central area of species such as *S. horticus* and *Cribrosphaerella ehrenbergii* were complete (see Fig 4.30 and Fig 4.31). The surface was covered in a wide variety of nannofossils with no one species appearing predominant. Many

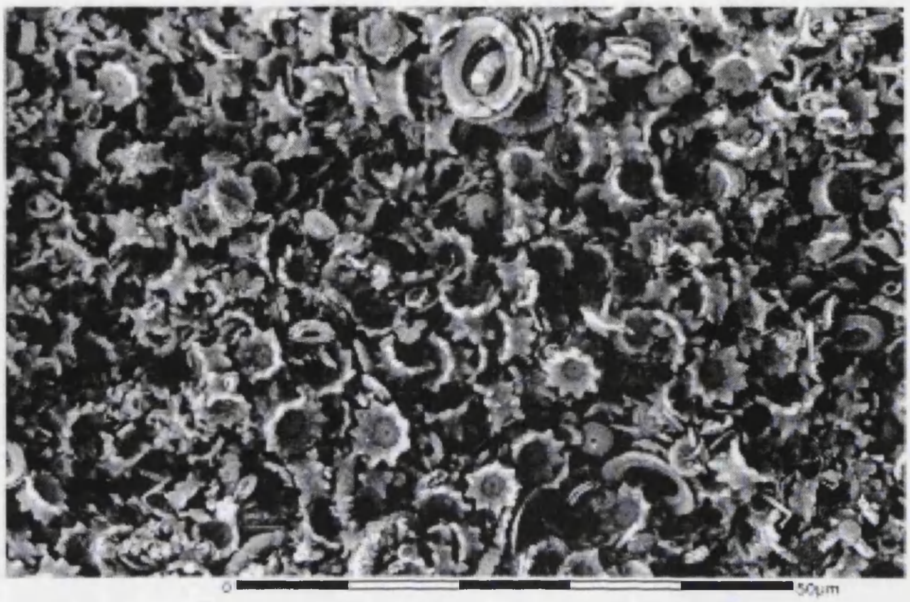

Figure 4.29: Almost monospecific bloom surface of *Eprolithus floralis* seen on the Southampton BSEM by Dr. Richard Pearce, scale at base of picture.

very small ($< 2\mu$m diameter) *Zeugrhabdotus* sp. were visible, probably these species were too small to be confidently identified under the light microscope. All the predominant and periodically predominant species were seen. In particular *Lithraphidites carniolensis* seemed to appear in clusters rather than being evenly spread across the surface. Possibly this represented burst coccospheres or alternatively monospecific faecal pellets. Remnants of coccospheres were seen reasonably frequently, especially for *W. barnesae* (see Fig 4.32). It was not possible to identify individual faecal pellets. This is probably because the faecal pellets overlapped each other and contained a similar mix of species. A few small foraminifera were seen but these did not dominate the surface.

4.8.2 Stub T2 - light area

Again preservation was good with delicate structures preserved and little overgrowth. The surface was covered with all predominant and periodically predominant calcareous nannofossils (see Fig 4.33). In particular *B. ellipticum* appeared frequently along with many very small *Zeugrhabdotus* sp.. Again remnants of coc-

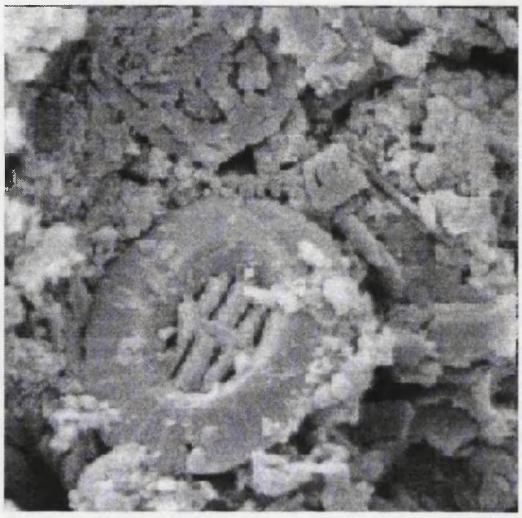

Figure 4.30: *Sollasites horticus* in Stub T1, magnification x 10000, picture width - 9.18μm.

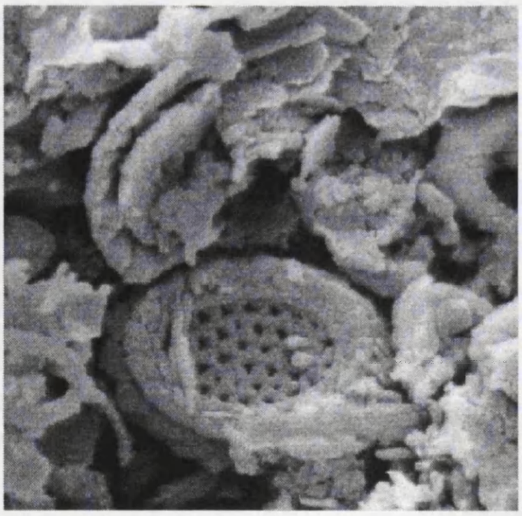

Figure 4.31: *Cribrosphaerella ehrenbergii* in Stub T2, magnification x 11500, picture width - 7.98μm.

Figure 4.32: *Watznaueria barnesae* in Stub T1, magnification x 7750, picture width - 11.85μm.

cospheres were seen reasonably frequently. A greater proportion of foraminifera were observed than in stub T1 and they were generally larger than those seen in T1. No obvious structures such as faecal pellets were visible.

4.8.3 Stub T3 - bioturbated area

Preservation of calcareous nannofossils was moderate to good, with some significant overgrowth. There was a high proportion of blocky crystalline pieces and calcite veins, suggesting that dissolution and re-crystallisation had taken place (see Fig 4.34). Calcispheres (or possibly foraminifera chambers) were common (see Fig 4.35). Very few coccosphere remnants were seen. The most common species to be observed were *Zeugrhabdotus* sp. and *S. horticus*. Few foraminifera were seen.

4.8.4 Stub T4 - dark laminated area

Preservation was good. This stub was a bed of mostly foraminifera, with at least three different species present. There were occasional pockets of calcareous nannofossils, probably where the surface cut into a different lamina. Where the nannofossils were visible they often appeared to be in near monospecific clusters

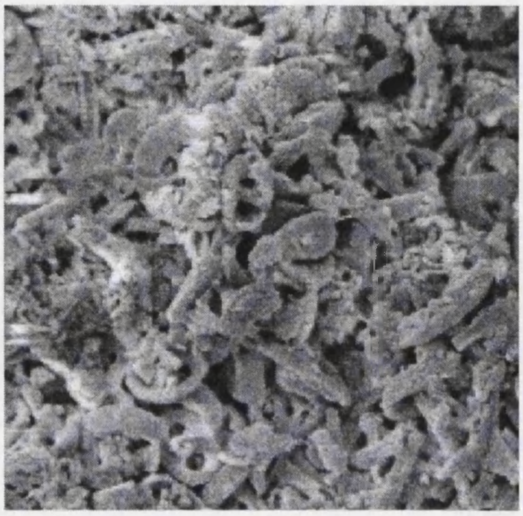

Figure 4.33: Typical surface of mixed nannofossil species in Stub T2, magnification x 3700, picture width - 24.84μm.

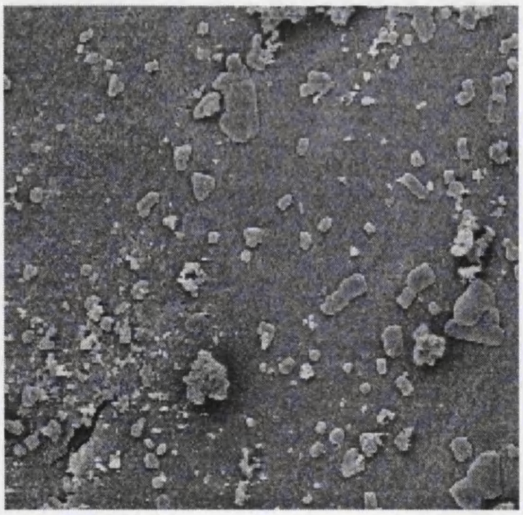

Figure 4.34: Typical crystalline surface in Stub T3, magnification x 2000, picture width - 45.96μm.

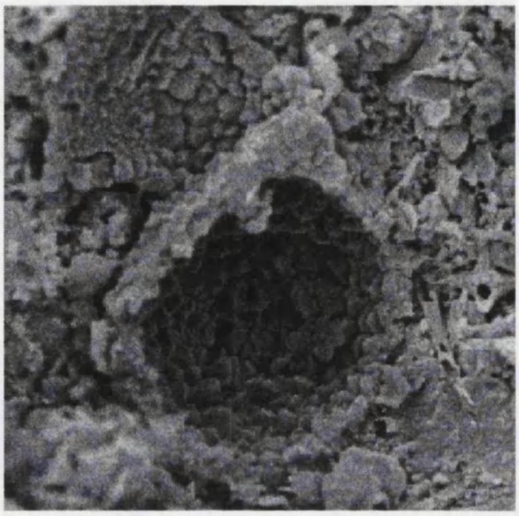

Figure 4.35: Foraminifera chambers in Stub T3, magnification x 3400, picture width - 27.03μm.

of either *S. horticus* or *Lithraphidites carniolensis.*

4.8.5 Stub T5 - dark laminated area

Preservation was good. This stub was almost the reverse of stub T4, with a layer of calcareous nannofossils and very few foraminifera visible. All predominant and periodically predominant nannofossil species were observed with no particular spatial structure.

5

Time series analysis of the Tarfaya greyscale data

5.1 Creating a time series

In the earth sciences stratigraphic position is often a proxy for time. Hence it is possible to analyze measurements made at regular intervals through a section, using the same methods used to analyze a true time series.

Of course there can be problems with assuming that stratigraphic position is a proxy for time; sedimentation rates may vary giving sharp discontinuities or even a hiatus. However nature generally varies in a reasonably continuous way and samples that are close to each other in space or time tend to be very similar, no matter what is measured. Providing there is no evidence for sharp discontinuities or a hiatus then most sedimentary sections can be analyzed using time series analysis.

5.2 Constructing the Tarfaya greyscale time series

The physical method of generating the data and creating a continuous record of greyscale is outlined in section 3.1. Examination of thin sections and closer inspection of the rock suggested that sedimentation rate had varied somewhat in this section.

It was noticed that the light/dark lamina couplets varied significantly in thickness and distinctiveness throughout the sediment. In particular there is a general pattern of thinner couplets in the darker sediment and wider couplets in the lighter sediment (see section 4.7). Possible interpretations for the change in lamina thickness are discussed in section 6.1. No sharp changes in couplet thickness are observed which implies that changes in sedimentation rate will have been gradual.

For the purposes of creating a time series the section was divided into shorter intervals to ensure that the variations in couplet thickness were small within each interval. This increased the probability that each interval was likely to have been deposited under similar environmental conditions. Because we were interested in looking at a number of different time scales the section was analyzed at three different orders of magnitude. Firstly the entirety of the section was analyzed to focus on variation at the decimetre scale. Then the section was divided into 29 intervals of 34.7cm each in order to pick up variation at the centimetre scale. Finally the section was further subdivided into 117 intervals of 8.7cm each to observe millimetre scale variations. The interval lengths were chosen with ease of carrying out a Fast Fourier Transform in mind, as explained in the next section.

5.3 Fourier Series and spectral analysis

An excellent description of Fourier series and spectral analysis can be found in [112] The following paragraphs summarize the description in Middleton (2000) and a more detailed description can be found in [112].

Fourier series are sums of sine and cosine waves, of the type (5.3.1).

$$f(t) = \frac{a_0}{2} + \sum [a_n \cos(2\pi nt) + b_n \sin(2\pi nt)] \tag{5.3.1}$$

where a_0, a_n and b_n are constants and n = 1,2,3,4........

This can also be written more simply as a sum of a single complex exponential series (5.3.2).

$$f(t) = \sum c_n e^{-2\pi int} \tag{5.3.2}$$

where c_n is a constant.

A Fourier series can be used to represent almost any time series as a sum of sine and cosine waves, no matter how angular and irregular that original time series seems to be.

Fitting a Fourier series to a time series consisting of N equally spaced data generally produces a sum of N/2 distinct pairs of sine and cosine terms, with different amplitudes a_n and b_n. The constant term a_0 can be made zero by first subtracting the mean value from each term in the series. For large N the amount of computation required is large, but it can be reduced to the order $Nlog(N)$ operations, by using a technique known as the Fast Fourier Transform (FFT). The only disadvantage with the FFT is that the number of input data must be a power of 2 (e.g. 64, 128, 256, 512......).

One important point about Fourier series is that only the terms up to $n = \frac{N}{2}$ contain any useful information. The frequency corresponding to this midpoint is called the Nyquist frequency. Above the Nyquist frequency the frequencies are higher than the frequency of sampling and so the samples are not sufficiently spaced to detect periodic variations on such a short time scale.

Performing spectral analysis on a finite, discrete time series produces a finite, discrete spectrum, showing the estimated variance (amplitude squared) of each frequency in the series up to the Nyquist frequency. This is called the periodogram.

5.4 Spectral analysis using MATLAB

MATLAB's FFT function determines the coefficients a_n and b_n for a time series x of length N. If N is a power of 2, then the FFT employs the Fast Fourier algorithm; if N is not a power of 2 it employs a slower algorithm [112]. Confidence levels are computed at the 95% level using a standard formula given by [38].

A polynomial curve fitting function is applied to the log-log plot to obtain the slope of the upper and lower parts of the graph. Since the function is applied with only one degree of freedom it simply fits the best straight line. The resulting gradients are referred to as ma (the upper part of the graph) and mb (the lower part of the graph).

The program used on the Tarfaya data was adapted from [112] and is reproduced in appendix D.1. It is designed for use on MATLAB for the Macintosh.

5.5 Density plots

Density plots were used to represent the results from all the individual sections on one plot. Each interval is plotted at a different position along the x axis with frequency running up the y axis. The variation in power for each frequency is then represented by colour. In this way it is easy to spot if a particular periodicity is dominant throughout the section, or only in certain parts of the section.

The MATLAB program used to generate density plots for the Tarfaya data is reproduced in D.2. Density plots are known as contour plots in the MATLAB programming language. Again it is designed for use on MATLAB for the Macintosh.

The shading used on the density plot was MATLAB's *hot* shading which runs from white to black through yellow, orange and red. White represents the highest values and black the lowest.

5.6 Results

The periodograms for spectral analysis of the entire Tarfaya section are shown in Figures 5.1 and 5.2. Representative periodograms for the sections of 34.7cm and 8.7cm length are shown in figures 5.3 to 5.14. Sections mat 21 and 21b come from piece 5C (see appendix C.1) and are examples of one of the lighter intervals from the section. Sections mat 14 and 14b come from piece 9A2/C (see appendix C.2) and represent an intermediate colour for the Tarfaya sediments. Sections mat 9 and 9b come from piece 11F (see appendix C.3) and represent a darker interval of the section.

Appendix D.3 contains two tables (Table D.1 and Table D.2) that show the average values of greyscale for each interval and the corresponding gradients from the log-log plot of the periodogram. For the upper part of the plot the gradient is labelled 'ma' and for the lower part of the plot 'mb'.

Scatter plots showing the amount of correlation between the average greyscale and each gradient (ma and mb) are shown in figures 5.15 to 5.19. Fig 5.16 is the same plot as Fig 5.15, but with an outlier sample, mat22, removed from the data. Mat22 comes includes rock interval 4C/D which is a particularly homogenized

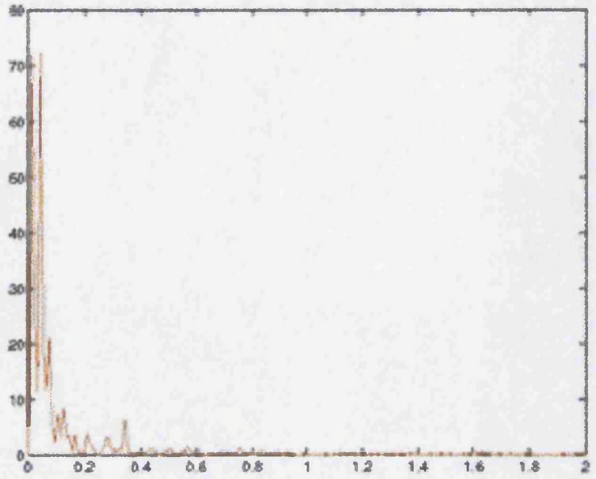

Figure 5.1: Periodogram (arithmetic variance scale) for the entire Tarfaya quarry dataset. y axis - variance, x axis - frequency per cm.

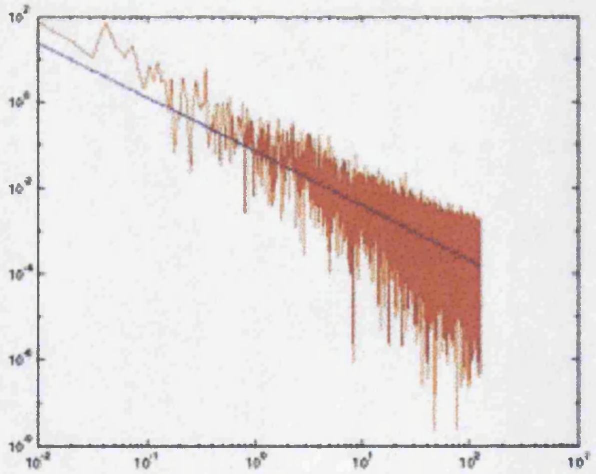

Figure 5.2: Periodogram (logarithmic scale) for entire Tarfaya quarry data set. Line of best fit in blue, gradient of -1.27. y axis - variance, x axis - frequency per cm.

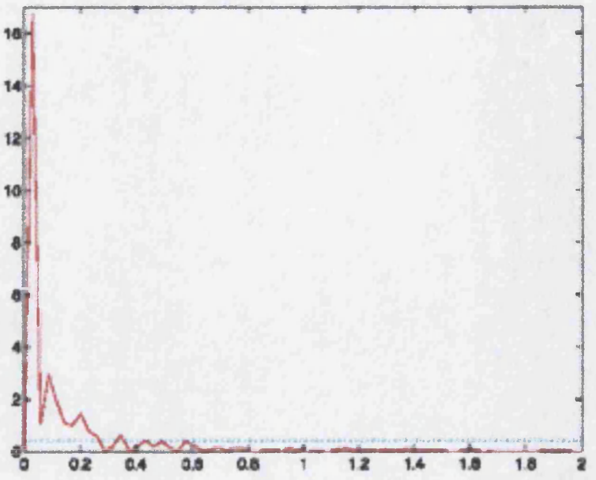

Figure 5.3: Periodogram (arithmetic variance scale) for mat21 (34.7cm from lighter interval in piece 5C). y axis - variance, x axis - frequency per cm.

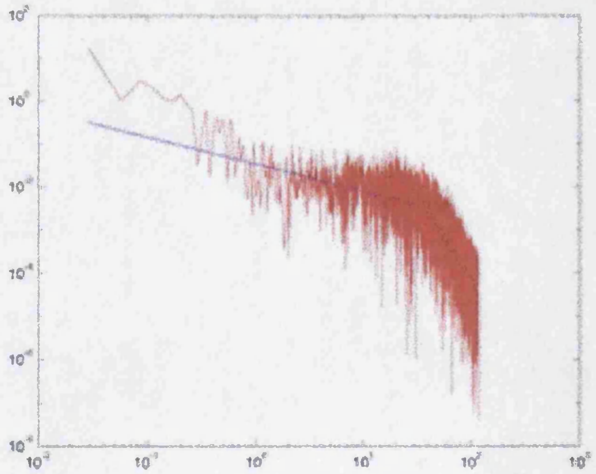

Figure 5.4: Periodogram (logarithmic scale) for mat21 (34.7cm from lighter interval in piece 5C), ma in blue, mb in green. y axis - variance, x axis - frequency per cm.

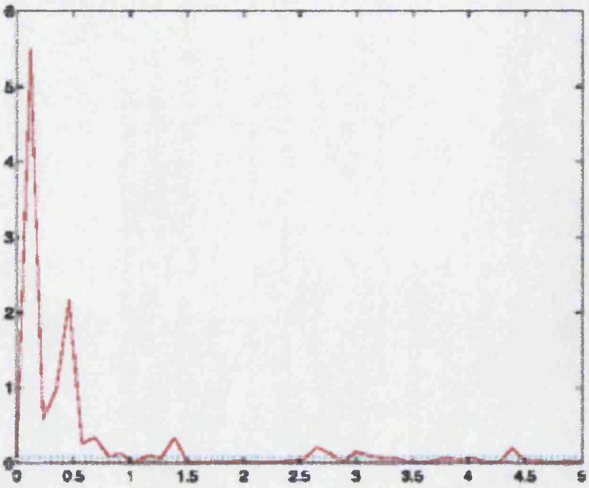

Figure 5.5: Periodogram (arithmetic variance scale) for mat21b (8.7cm from lighter interval in piece 5C). y axis - variance, x axis - frequency per cm.

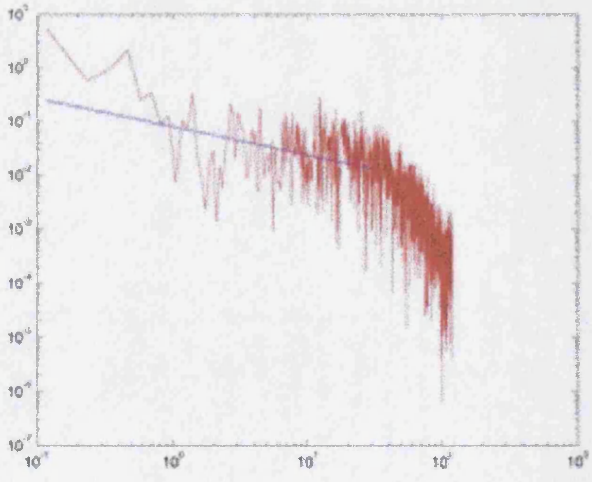

Figure 5.6: Periodogram (logarithmic scale) for mat21b (8.7cm from lighter interval in piece 5C), ma in blue, mb in green. y axis - variance, x axis - frequency per cm.

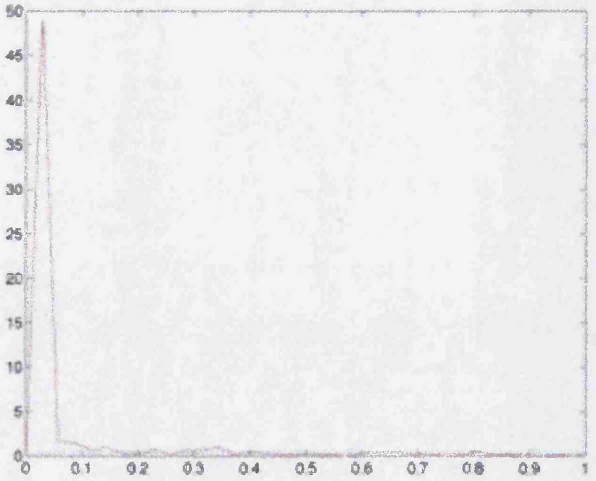

Figure 5.7: Periodogram (arithmetic variance scale) for mat14 (34.7cm from an intermediate colour interval in piece 9A2/C). y axis - variance, x axis - frequency per cm.

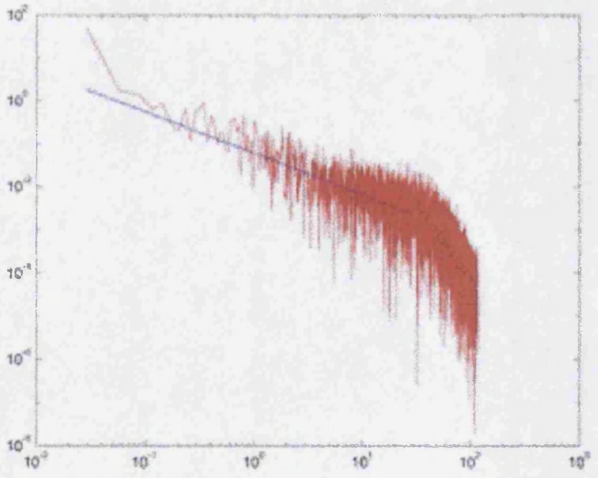

Figure 5.8: Periodogram (logarithmic scale) for mat14 (34.7cm from an intermediate colour interval in piece 9A2/C), ma in blue, mb in green. y axis - variance, x axis - frequency per cm.

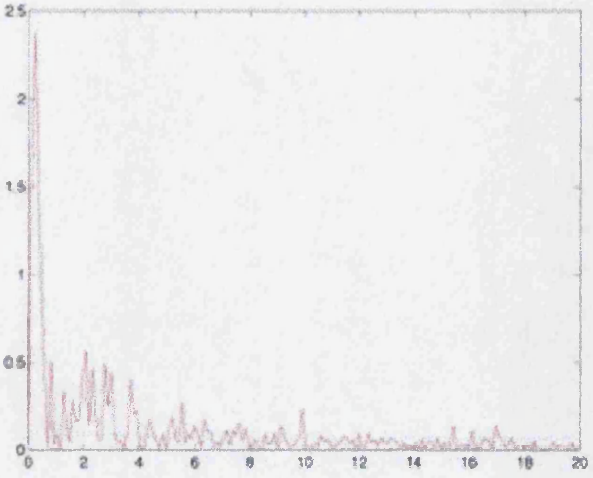

Figure 5.9: Periodogram (arithmetic variance scale) for mat14b (8.7cm from an intermediate colour interval in piece 9A2/C). y axis - variance, x axis - frequency per cm.

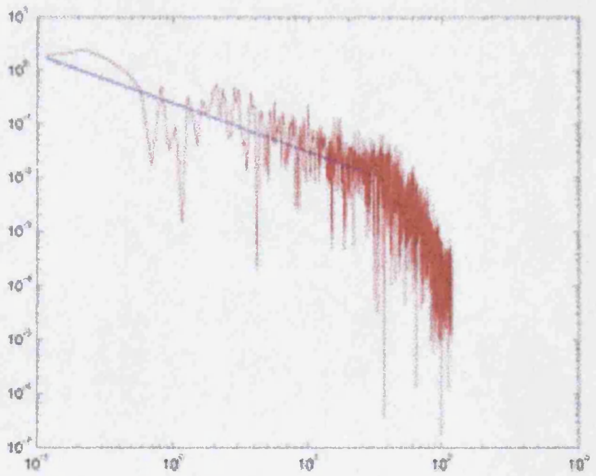

Figure 5.10: Periodogram (logarithmic scale) for mat14b (8.7cm from an intermediate colour interval in piece 9A2/C), ma in blue, mb in green. y axis - variance, x axis - frequency per cm.

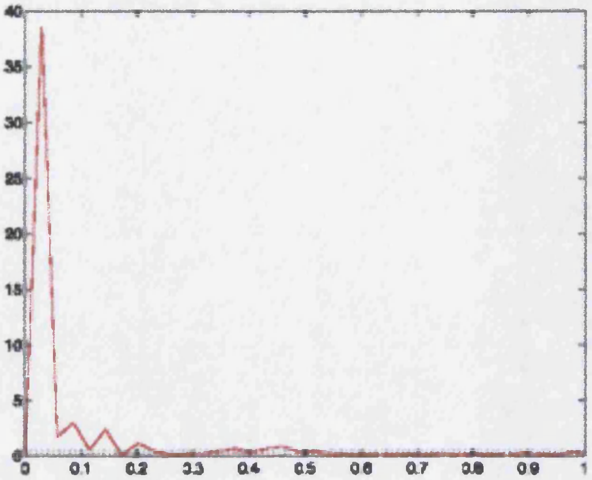

Figure 5.11: Periodogram (arithmetic variance scale) for mat9 (34.7cm from a dark colour interval in piece 11F). y axis - variance, x axis - frequency per cm.

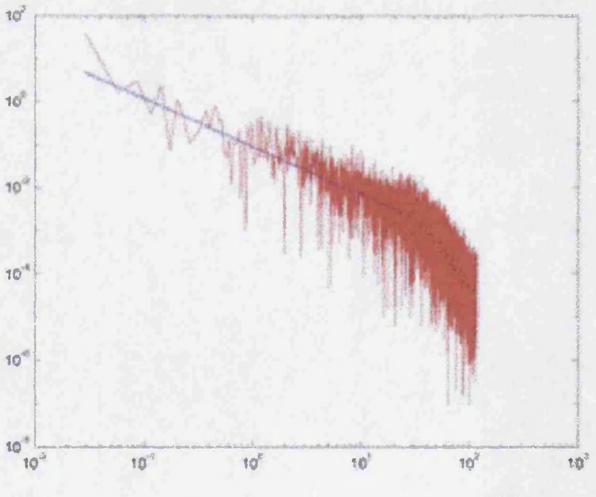

Figure 5.12: Periodogram (logarithmic scale) for mat9 (34.7cm from a dark colour interval in piece 11F), ma in blue, mb in green. y axis - variance, x axis - frequency per cm.

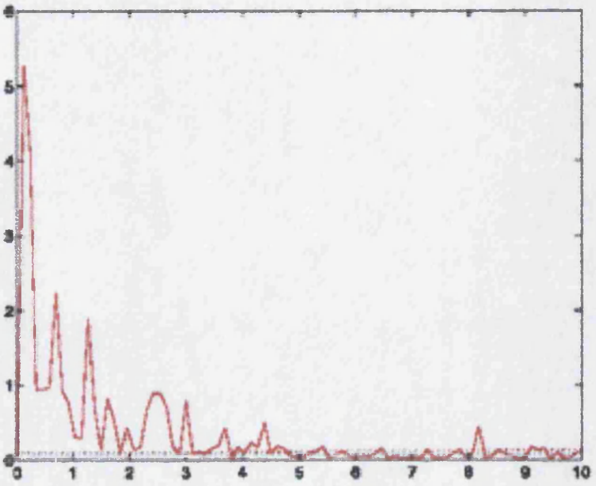

Figure 5.13: Periodogram (arithmetic variance scale) for mat9b (8.7cm from a dark colour interval in piece 11F). y axis - variance, x axis - frequency per cm.

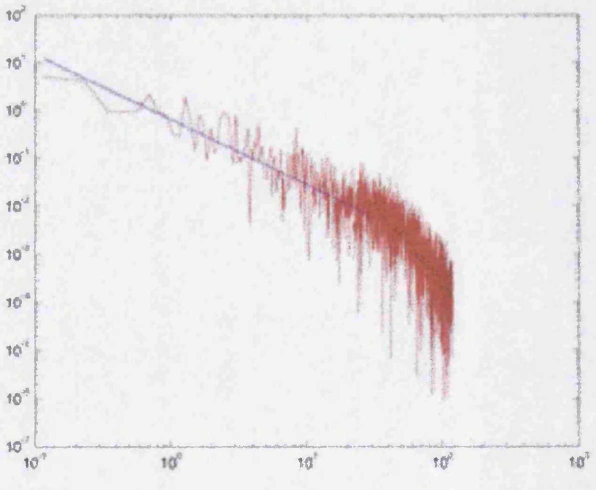

Figure 5.14: Periodogram (logarithmic scale) for mat9b (8.7cm from a dark colour interval in piece 11F), ma in blue, mb in green. y axis - variance, x axis - frequency per cm.

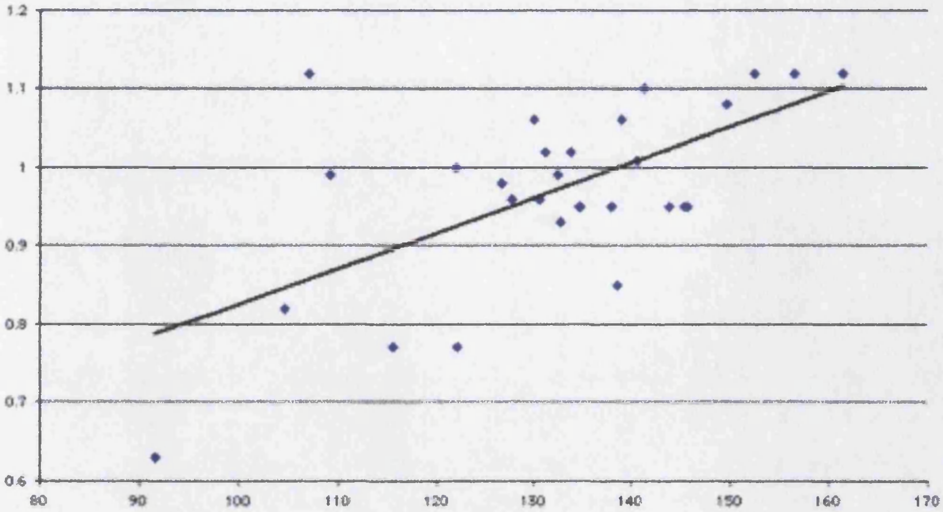

Figure 5.15: Correlation between ma and greyscale values for pieces of length 34.7cm. $\rho = 0.62$ y axis - gradient ma, x axis - average greyscale (higher numbers are darker colours)

piece of rock as appendix C.4 shows. Table 5.1 shows the correlation co-efficients between periodogram gradient and greyscale. It is worth noting that the correlation coefficients between average greyscale and gradient ma are high, while no correlation is seen between average greyscale and gradient mb.

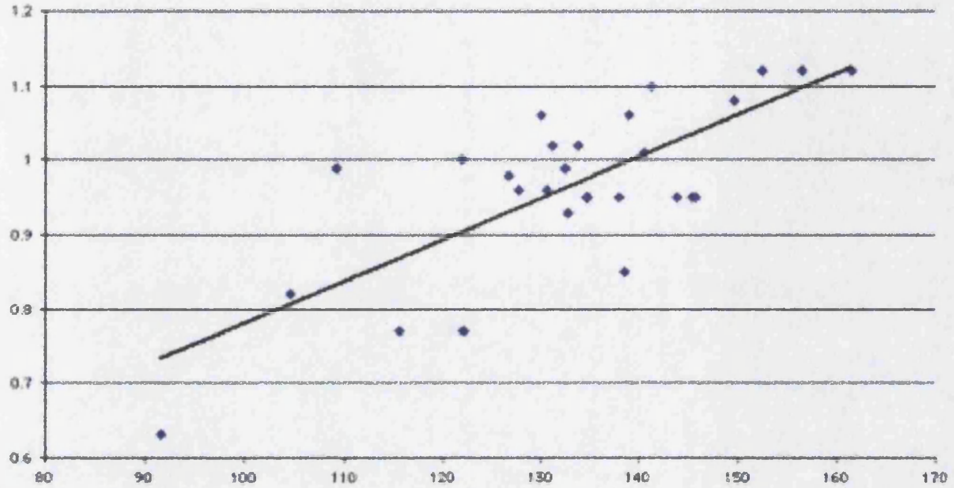

Figure 5.16: Correlation between ma and greyscale values for pieces of length 34.7cm with the outlier sample mat22 removed. $\rho = 0.75$ y axis - gradient ma, x axis - average greyscale (higher numbers are darker colours)

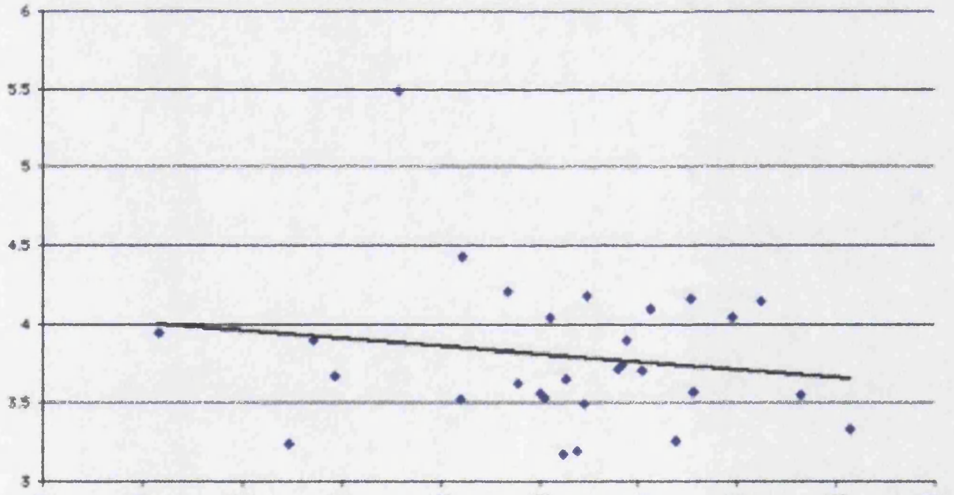

Figure 5.17: Correlation between mb and greyscale values for pieces of length 34.7cm. $\rho = -0.17$ y axis - gradient ma, x axis - average greyscale (higher numbers are darker colours).

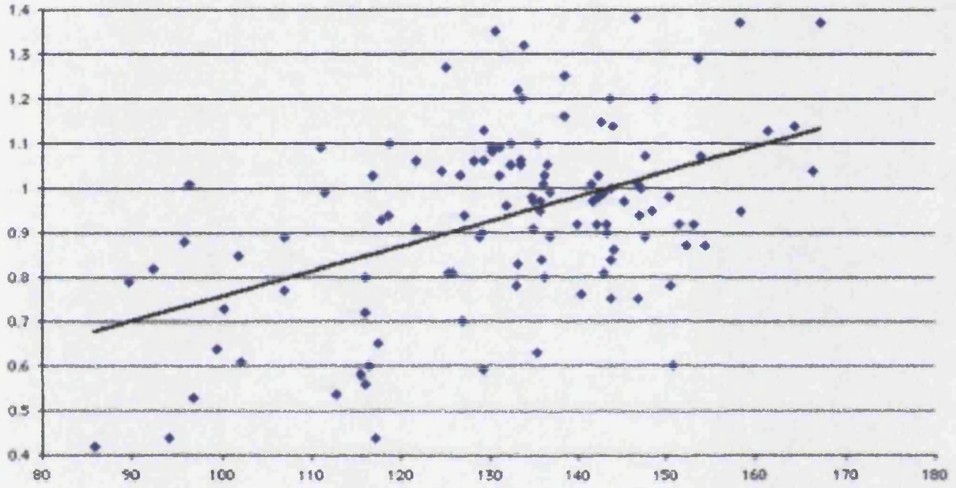

Figure 5.18: Correlation between ma and greyscale for pieces of length 8.7cm. $\rho = 0.48$ y axis - gradient ma, x axis - average greyscale (higher numbers are darker colours).

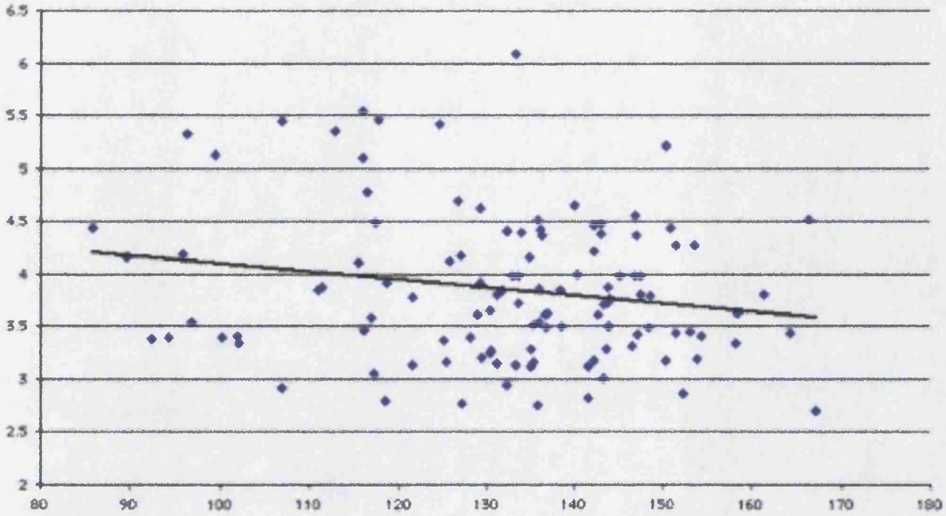

Figure 5.19: Correlation between mb and greyscale for pieces of length 8.7cm. $\rho = -0.19$ y axis - gradient ma, x axis - average greyscale (higher numbers are darker colours).

correlation between	coefficient, ρ
greyscale and ma - 34.7cm pieces	0.62
greyscale and ma - 34.7cm pieces with outliers mat22 and mat13 removed	0.75
greyscale and ma - 8.7cm pieces	0.48
greyscale and mb - 34.7cm pieces	-0.17
greyscale and mb - 8.7cm pieces	-0.19

Table 5.1: Table of correlation coefficients between periodogram gradients and greyscale.

All of the results from the FFTs on the intervals of 34.7cm length are combined in a contour plot Fig 5.20 The key for the frequency values is shown in Table 5.2.

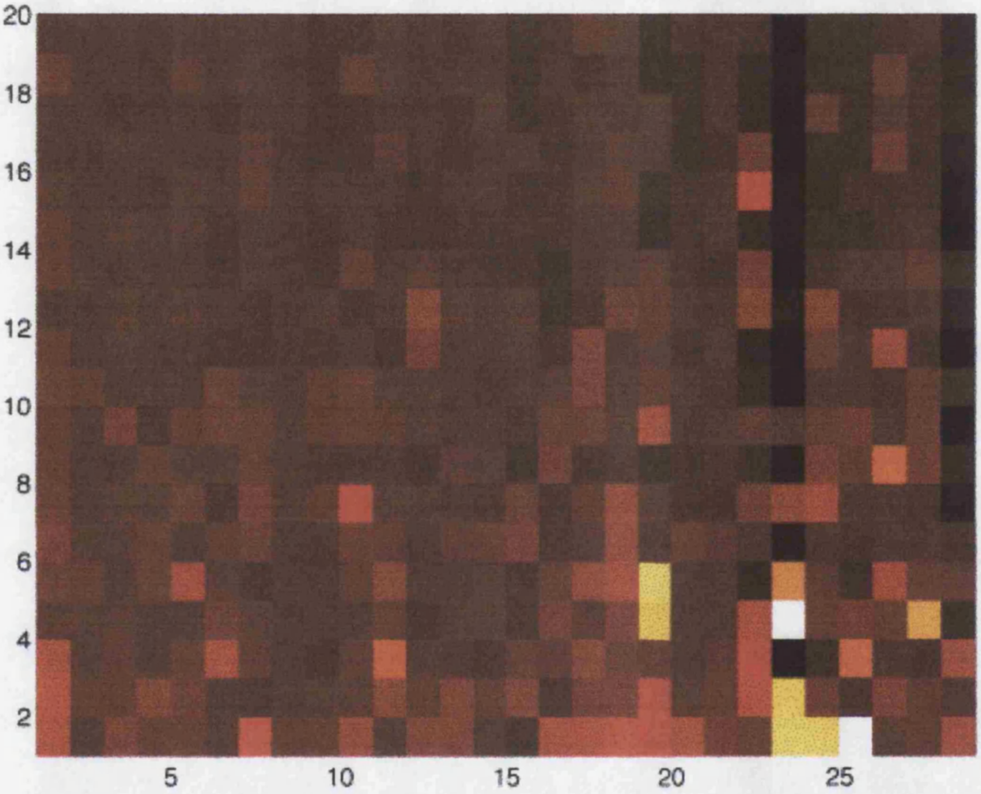

Figure 5.20: A density plot showing the variations in power from the FFTs of the Tarfaya data. x axis - sample number, y axis - frequency (see Table 5.2).

axis position	frequency ($\frac{1}{cm}$)	$\frac{1}{frequency}$ in cm
1	0	infinity
2	0.0288	34.8
3	0.0577	17.3
4	0.0865	11.6
5	0.115	8.7
6	0.144	6.9
7	0.173	5.8
8	0.202	5
9	0.231	4.3
10	0.26	3.8
11	0.288	3.5
12	0.317	3.2
13	0.346	2.9
14	0.375	2.7
15	0.404	2.5
16	0.433	2.3
17	0.461	2.2
18	0.49	2
19	0.519	1.9
20	0.548	1.8
21	0.577	1.7
22	0.606	1.7
23	0.634	1.6
24	0.663	1.5
25	0.692	1.4
26	0.721	1.4
27	0.75	1.3
28	0.779	1.3
29	0.807	1.2
30	0.836	1.2
31	0.865	1.2

Table 5.2: Key for frequency values on the density plot Fig 5.20.

6

Discussion

6.1 What is the Tarfaya greyscale a proxy for?

Digital sediment colour analysis (DSCA) records changes in the brightness of sediment and the frequency with which that brightness changes. Sediment is made up from differing shapes, sizes and colours of particles. The resolution at which the DSCA is carried out determines whether individual particles will be recognised or not.

DSCA was carried out with a resolution of 600 pixels per inch (one reading every 0.042mm) for the Tarfaya sediments. Hence individual particles such as faecal pellets and foraminifera did dominate some readings, but this was compensated for by taking 5 separate line scans (each 8 pixels wide) and averaging the result. The distance between the 5 lines varied from slab to slab and were chosen manually to ensure that the 5 most representative lines were scanned. In each case it was ensured that the line scans were carried out perpendicular to the laminae. The resulting greyscale record is a considerably smoothed version of greyscale for each slab, picking out the broad colour changes, but unable to resolve fine detail such as lamina scale colour changes.

The broad correlation of greyscale with $C_{organic}$ ($\rho = 0.77$) and C_{CaCO_3} ($\rho = -0.76$), indicates that dark sediment with high values of greyscale has a high organic carbon content, while light sediment with low greyscale values has a high calcium carbonate content (eg calcareous nannofossils and foraminifera). Low frequency changes in greyscale values are best described as a proxy for the carbon chemistry of the Tarfaya sediment.

Focusing in and looking at the high frequency changes in greyscale values reveals another level of detail in using greyscale as a proxy indicator. Some level of correlation is seen between power spectra slope and average greyscale (see section 5.6). In general the higher the average greyscale (darker sediment), the steeper the slope of the upper part of the power spectra, indicating a greater component of *red noise* character to the data.

The terms red noise and white noise are derived from optical spectroscopy where white light contains all the visible frequencies. An excellent background to red and white noise is described in Burroughs [28], and the following is a summary.

If data contains fluctuations at every timescale, contributing to all frequencies with equal probability, then it will produce a flat, *white noise* power spectrum. On the other hand if the data is biased such that it tends to damp out the more rapid fluctuations then it will exhibit greater low frequency fluctuations than high frequency ones. This will lead to a *red noise* spectrum where the distribution is weighted towards the lower frequencies. In real terms this means that the system being measured has a *memory.* Weather systems typically exhibit red noise characteristics since weather has better recollection of recent events and short term variations are damped out more than long term variations.

In the case of the Tarfaya data we see that the darker sediment has more red noise characteristics than the lighter sediment, suggesting that the darker sediment has a longer *memory.* Further evidence for this comes from phase diagrams of the data (see section 4.3.1).

As expected the greater the number of offsets used to plot each phase diagram, the more random the pattern becomes and the weaker the correlation between measurements. However the loss of *memory* or increase in disorder is quickest in the lighter sediment. In physical terms this means that the brightness of adjacent and nearby points is more likely to be very similar in darker areas of sediment than lighter areas.

This implies that dark sediment varies its brightness more smoothly than light sediment. Possibly this is due to the difference in types of particle making up dark and light sediment. Additionally sediment structure will be important at this scale.

Thin section work revealed that the darker areas of sediment tend to have well defined lamina that are laterally continuous. In contrast the lighter areas of sediment have a more disturbed appearance: the sediment has some structure with faecal pellet rich areas and foraminifera rich areas, but laterally continuous lamina are much harder to trace.

Putting these results together reveals that the high frequency greyscale variations in the Tarfaya sediments are a complex proxy for sediment structure and content. Broadly speaking when the greyscale power spectra has a strong red noise component the sediment is ordered and probably laminated, where as when the power spectra tends towards white noise the sediment is *noisy* with little structure and a more homogenised appearance.

6.2 Cyclicity in the Tarfaya sediments

Strong evidence exists for Milankovitch cyclicity in the Tarfaya sediments, in particular the 39000 year obliquity cycle appears to be dominant [92] (see section 4.4). One of the aims of this research was to look for higher frequency cycles by focusing in on a short, detailed section. As chapter 5 details, time series analysis was carried out on the greyscale record. None of the resulting periodograms provide significant evidence for cyclicity at higher frequencies than Milankovitch cycles.

This is illustrated in the density plot for blocks of length 34.7cm (Fig 5.20). As expected the colour darkens going up the plot, showing the decrease in power for shorter wavelengths. If any cycles with length less than 34.7cm existed then we would expect a bright horizontal band at the relevant frequency. This would indicate strong power (or peaks in the spectrum) for a particular frequency throughout the section. No such band is seen. Another possibility would be transient cycles that come and go, probably dependent upon the varying sedimentation mechanism. Sections of rock that contain strong power at a particular frequency are plotted as a bright spot, a number of bright spots at the same frequency indicates a frequency that is dominant and re-occurring. This would be represented by a bright horizontal band with a dashed appearance. Again this is not seen.

What the greyscale does exhibit is power law fourier series (see section 2.11.1). The logarithmic periodogram for the entire Tarfaya data set, Fig 5.2, shows no significant periodic frequencies, but instead exhibits a power law fourier series with gradient of -1.27. This result hints at complex underlying dynamics, not necessarily correlated to external factors, as described in section 2.11.1. As hinted there, such data could indicate a mechanism for sedimentation in the Tarfaya Basin which has some so-called self organised criticality (SOC) characteristics. In many ways this is not a surprising result. Greyscale is a measure of colour and brightness, both of which vary over a wide range of time and depth scales, with few major discontinuities. It is conceivable that changes in colour and brightness are largely internally driven by factors such as water turbulence, sediment settling rate, particle flocculation and sediment compression. Factors that effect greyscale and are likely to have been externally driven, such as particle type (for example the ratio of carbonate to organic carbon particles) may have been suppressed or over-ridden by the internal dynamics. However it must be noted that this result only tells us about the mechanisms creating the greyscale record. It is quite possible that other proxies in the Tarfaya data were more intimately linked to external factors such as climate dynamics.

Further evidence for the greyscale record being produced by a non-linear system comes from the logarithmic periodograms for the shorter sections. In particular the upper part of the logarithmic periodograms exhibit varying degrees of *red noise*. As explained in section 6.1, the darker sediment tends to have more red noise character than the lighter sediment, suggesting that the darker sediment has a longer *memory*, i.e. it is more temporally correlated. Correlation between greyscale and upper periodogram gradients is high (Table 5.1). The greater white noise character in lighter sediment suggests that sedimentation was more turbulent in character and that the system was much noisier than during times of dark sediment deposition. Together with the fossil and sedimentary evidence it suggests that light and dark sedimentation environments differed considerably.

In addition, when looking at the thin sections it was noticed that the dark sediment had a more ordered appearance than the light sediment (see section 4.7). Distinct banding was visible in the dark sediment from the lamina scale up to the order of centimetres. By contrast the lighter parts of the sediment had a more homogenised appearance. The greater degree of organisation in the darker sediment could be due to a number of effects. As discussed above, it appears that the greyscale record is strongly effected by the internal dynamics of the system, therefore it is likely that internal changes caused the swings in noise character from red to white. For example changes in the degree of turbulence in the water column would have effected how the particles fall through the water and settle in the sediment. It is conceivable that the water column was more turbulent in nature during light sediment deposition meaning that particles were more strongly mixed before reaching the ocean floor. Another possibility is that the degree of particle flocculation differed in light and dark sediment deposition. Perhaps sedimentation was faster and particle flocculation stronger during dark sediment deposition. This would give the sediment a more blocky and layered appearance as particles that started in the top layer of the ocean together would have a greater chance of reaching the bottom at the same time. In this way distinct events such as planktonic blooms would have a greater chance of being recorded in the underlying sediment.

One can conclude that in order to create distinct layers, the darker sediment must have been deposited in calm, most likely anoxic, bottom waters. During episodes of lighter sediment deposition the bottom layer may not have been as well developed and possibly bottom waters were more turbulent in nature. Additionally it would seem that dark sediment deposition was more event driven than light sediment deposition. Certainly at the lamina scale the distinct bloom events are visible in the form of faecal pellet layers. By comparison the light sediment doesn't exhibit such a distinct layered appearance and this suggests that the sedimentary environment was more continuous over time.

The lower periodogram gradient, mb, shows no correlation with greyscale. This is likely to be because the high frequency greyscale record contained a lot of noise and this will have over-ridden any natural signals.

No extra information was gained from carrying out time series analysis on 8.7cm blocks as well as the 34.7cm blocks. This is likely to be because the greyscale record was too noisy at the millimetre resolution to give any extra information. This is evidenced by the drop in correlation between greyscale and upper periodogram gradient, ma, for the shorter, 8.7cm blocks (Table 5.1). Nonetheless it can still be seen that dark sediment sections have more of a red noise character, while light sections tend to have more of a white noise character.

One might expect to see evidence for some cyclicity at the annual scale given the estimated sedimentation rates (see section 4.7.4). Calculations suggest that individual lamina (light/dark couplets) are likely to represent time scales of the order of 6 months to a year. Unfortunately the greyscale measurements were not of high enough resolution to pick out variations from lamina to lamina. On average only one or two greyscale readings will have been made for each lamina. To see any cyclicity a minimum of seven measurements per cycle is required. If time had allowed it would have been better to make thin sections of the entire Tarfaya quarry section and to obtain a high resolution greyscale record from the thin sections.

6.3 Interpreting the high organic carbon values

There is still disagreement within the scientific community as to the origins of organic carbon rich sediments. However it is clear that high primary productivity is essential to provide a sufficient amount of organic material [86], [129]. Organic carbon preservation is favoured in calm environments with a stratified water column [86]. However, calm stratified water is not a pre-requisite for preserving organic carbon and upwelling environments are also important environments for organic carbon preservation. The high level of nutrients being brought into the oxygenated photic zone increase phytoplankton production. High rates of sedimentation may cause the bottom waters to become anoxic and so encourage organic carbon preservation. A current example is the accumulation of organic rich sediments under the Peru upwelling [86].

Values of $C_{organic}$ in the Tarfaya section range between 1.99% and 17.8%. In present day sediments $C_{organic}$ rarely exceeds 2% and over most of the ocean floor it is less than 0.25% [86]. In addition sediment accumulation rates were high in the Tarfaya Basin (see section 4.7.4). Taking an average sedimentation rate of $0.077mm/year$ and using the same estimates of sediment density and preservation factor as Luderer for the Tarfaya Basin [105], the organic carbon accumulation rates for the Tarfaya Basin lie between 10 and $40gC/m^2/year$. These values are at least an order of magnitude greater than those calculated by Bralower and Thierstein [25] for mid-Cretaceous deep sea sediments and suggest that the Tarfaya Basin was extremely productive at this time. Hence the high to extreme values of $C_{organic}$ and the high sedimentation rate in the Tarfaya section would suggest that productivity was always high and played an important part in sediment production and preservation at the time. Such high values of $C_{organic}$ can only be explained by strong upwelling in the Tarfaya Basin. This implies that the higher the value of $C_{organic}$, the greater the intensity of the upwelling.

Additionally it is found that both $C_{organic}$ and C_{CaCO_3} exhibit strong correlation with the greyscale record (see section A.3). The darker sediment tends to contain a greater percentage of organic carbon, while the lighter sediment contains a greater proportion of calcium carbonate. One possible explanation is that productivity was more intense during episodes of dark sediment deposition and weaker during periods of light sediment deposition. This idea is pursued further in the following section where the calcareous nannofossil results are taken into consideration.

6.4 Biodiversity of the Tarfaya section

Quantitative SEM work and thin section observations reveal that the darker sediment is composed from thin layers of faecal pellets interspersed with dark organic material (see section 4.7). Species diversity is low compared to lighter coloured sediment. Foraminifera are dominated by *Heterohelix moremani*, while some of the faecal pellet layers are composed almost entirely from *E. floralis* (see Fig 4.29). This suggests that almost monospecific blooms of *E. floralis* occurred from time to time.

In contrast the lighter sediment comprises indistinct light/dark couplets that are much thicker than those in the dark sediment (see section 4.7). More of a variety of foraminifera and radiolarian are observed and faecal pellets are larger and not monospecific.

6.4.1 *Eprolithus floralis*

Sample preparation for the light microscope is described in section 3.2.1. Due to the abrupt nature of the *E. floralis* faecal pellet layers it was not the best method of sampling to investigate such lamina scale detail. Since samples were taken over a 1cm thickness, including a number of laminae, the sampling will have been effected by the monospecific faecal pellet layers. Some samples will have contained a large proportion of *E. floralis* due to sampling across one or more *E. floralis* layers, while other samples will have been nearly devoid of *E. floralis* when the sample area didn't include an *E. floralis* layer. The uneven nature of the *E. floralis* distribution means that light microscope counts will have been skewed with respect to *E. floralis.* To get a general picture of how *E. floralis* changes through the Tarfaya section it is probably necessary to sample over a greater depth, say 2cm, to reduce the bias towards monospecific faecal pellet layers. In hindsight 1cm did not cover enough lamina, but it still gives a reasonable picture of the changes in calcareous nannofossils throughout the Tarfaya section.

Not surprisingly little mathematical correlation is seen between greyscale values and *E. floralis.* However it is possible to see some correlation visually between extreme values of greyscale and extreme abundances of *E. floralis* (see Fig 4.11). For example *E. floralis* abundance is generally high between 250cm and 350cm, and generally low between 650cm and 750cm. Inconsistencies such as the dip in abundance around 300cm could be due to just missing an *E. floralis* faecal pellet layer within the 1cm sampling space.

The correlation observed between extreme values of greyscale and extreme abundances of *E. floralis* suggests that the environmental conditions that favoured dark sediment deposition, also supported frequent blooms of *E. floralis.* On the other hand the environmental conditions that favoured light sediment deposition, were not conducive to blooms of *E. floralis.*

This is further supported by the strong negative correlation between *E. floralis* abundance and both the Shannon Weaver diversity index H(S) and Equatability (E) (see Table 4.4). H(S) is a measure of diversity while E is a measure of species dominance. The negative correlation indicates that when *E. floralis* is abundant it is extremely common and the diversity of calcareous nannofossils is low. Bralower documents extremely high abundances of *E. floralis* (up to 80.4%) in many C/T boundary intervals from numerous sections in Europe, North America and Africa [24]. He notices that the *E. floralis* peak occurs earlier in North West Europe than in the Western Interior Basin. In addition the samples containing abnormal *E. floralis* contents also possess an absence of planktonic and calcareous benthic foraminifera and numerous ostracods. Since *E. floralis* are a solution resistant taxa, Bralower suggests that high enrichments of *E. floralis* are partly of diagenetic origin, possibly indicating a widespread dissolution event in the water column or during early diagenesis [24]. Given that *E. floralis* has been documented as a cold water species [148], [95], [24] it is likely in this case that it took advantage of extreme conditions where upwelling was intense and there was a strong flux of nutrient rich, cold water.

6.4.2 *Tranolithus* species and *Sollasites horticus*

S. horticus, T. orionatus and *T. minimus* all show a significant correlation with greyscale values (see Table 4.4). They become abundant in lighter areas of sediment and are infrequent in darker areas of sediment. This is in direct contrast to the behaviour of *E. floralis.*

In addition some positive correlation is seen between *S. horticus, T. orionatus* and *T. minimus* and the values of H(S) and E. When *S. horticus, T. orionatus* and *T. minimus* are abundant the diversity of species is high and no one species is dominant. One can conclude that *S. horticus, T. orionatus* and *T. minimus* thrived in a different environment to the one preferred by *E. floralis.* Scarparo Cunha provides evidence that *Tranolithus* sp. preferred relatively warm waters and nutrient rich environments [154]. A possible scenario in the Tarfaya basin during times of light sediment deposition, would be weak upwelling giving relatively warm and nutrient poor waters, supporting a diverse community that includes a wide range of calcareous nannofossils, foraminifera, radiolarian and zooplankton that grazed on the phytoplankton.

6.4.3 Other species of calcareous nannofossil

E. floralis, S. horticus, T. orionatus and *T. minimus* all show some level of correlation with other external proxy indicators such as carbonate and organic carbon variation. This suggests that these species responded strongly to changes in the Tarfaya basin environmental conditions. None of the other species exhibited a significant relationship with external proxies, implying that these species were, at most, only mildly influenced by the environmental changes established in the Tarfaya basin at this time, or responded in a non linear way to environmental changes.

Previous research has recognised *Biscutum* sp. and *Zeugrhabdotus* sp. as high fertility indicators, while *W. barnesae* correlated with low fertility environments [45], [51]. These species did not exhibit any clear cut patterns in the Tarfaya basin sediments. The Tarfaya basin environment appears to have been extreme and this may explain why the commonly recognised mid-Cretaceous fertility indicators are not responsive to environmental change here. *Biscutum* spp., *W. barnesae* and *Zeugrhabdotus* spp. do not show a strong correlation to the strongest trend seen in the Tarfaya data. It is possible that the limited number of cycles sampled did not cover a great enough time period to illustrate the variations in these species. Possibly a multivariate statistical analysis of the data may have teased out some of the more complex relationships between different species and environmental change.

6.4.4 Faecal pellets

Thin section work revealed a marked change in size and content of faecal pellets as sediment colour changed (see section 4.7). Within the darker coloured sediment faecal pellets occur in distinct layers. Generally the pellets are small, averaging around 150μm by 20μm. Some of the faecal pellet layers consist almost exclusively of *E. floralis* (see section 4.8). Small foraminifera are occasionally seen inside the faecal pellets, but generally the pellets are composed largely of calcareous nannofossils.

By contrast the lighter coloured sediment contains larger faecal pellets (average size 300μm by 100μm) as well as a greater range in faecal pellet size. Some of the largest faecal pellets are the order of five times larger in cross sectional area than the average dark sediment faecal pellet.

The most likely producers of the faecal pellets are copepods. These are currently the largest and most diverse group of aquatic crustaceans. They evolved in the Lower Cretaceous and quickly colonised all available water habitats.

The discrepancy in sizes between light and dark sediment faecal pellets suggest that the species assemblage of copepods differed between light and dark sediment environments. The greater range in sizes in faecal pellet in the light sediment implies a greater diversity in copepod species during light sediment deposition. This supports the idea of a less extreme environment, supporting a greater range of species, during light sediment deposition.

It is unlikely that copepods were selective grazers of calcareous nannofossils and it would seem almost impossible that they could be selective at the species level. Hence the near monospecific *E. floralis* faecal pellets suggests blooms of *E. floralis* rather than selective grazing.

To create the distinct layers of faecal pellets observed in the dark sediment a stable bottom water environment will have been necessary. In addition the lamina scale layering suggests distinct events when the plankton bloomed, combined with a background rain of sediment during the rest of the season. Within the light sediment the faecal pellet layers appear to merge into each other at times and lamina are much less distinct. This suggests a more continuous plankton population throughout the season during light sediment deposition.

6.4.5 Fish remains

One puzzling fact is the lack of fish scales and bone found in the Tarfaya sediments. Occasional pieces of phosphatic bone material are seen but they are far and few between. Some thin sections had a few fish scales, but again they were not numerous (see section 4.7). Given that the Tarfaya Basin was a highly productive area, it is expected that it would have supported a healthy fish population. One possible explanation is that fish shoals only arrived seasonally rather than living in the waters all year round. Hence the only time when fish remains might have reached the sediment were during the short seasonal visit. Another possibility is that fish bone was preferentially dissolved out from the sediment. Alternatively the area did not support fish populations. A more in depth analysis of exactly where the

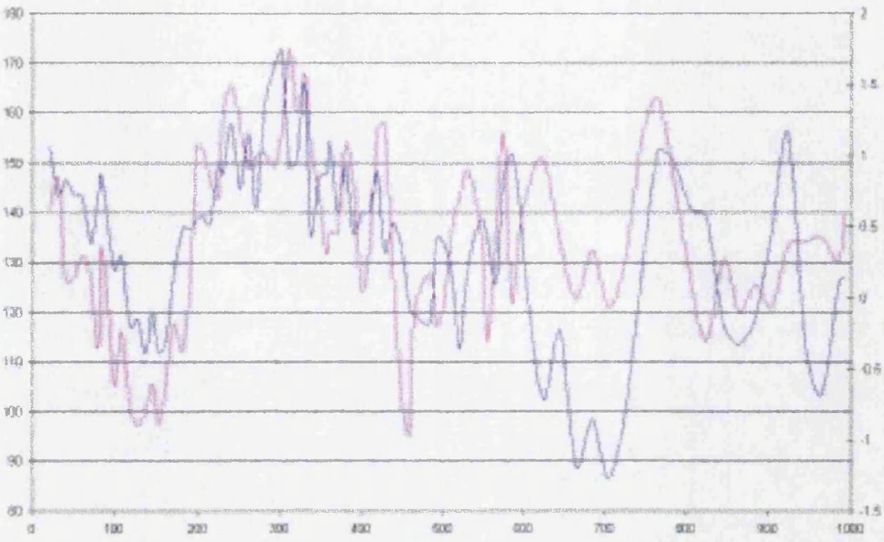

Figure 6.1: Variation in NIP and greyscale throughout the Tarfaya quarry core. Primary y axis - greyscale, where high numbers represent darker colours (blue), Secondary y axis - NIP (pink), x axis - depth/cm from top.

small amounts of fish bone and scales occur within the sediment structure may shed more light on this matter.

6.4.6 Nannofossil index of productivity

After concluding that *E. floralis* is a proxy for extreme upwelling (and associated high productivity) and that *S. horticus, T. orionatus* and *T. minimus* are proxies for moderate upwelling (and associated moderate productivity), it was possible to compute a nannofossil index of productivity (NIP) for the Tarfaya section.

A moderate correlation is observed between NIP and greyscale (see Table 4.5 and figure 6.1) showing that, in general, dark sediment (high values of greyscale) correlates with high values of NIP, while light sediment (low values of greyscale) correlates with low values of NIP.

This supports the idea of two productivity regimes that can be distinguished using sediment colour, chemistry, structure and microfossil assemblages. These productivity regimes are described fully later.

6.4.7 Foraminifera

Thin section work revealed changes in the diversity and distribution of foraminifera between the light and dark sediment (see section 4.7). Dark sediment is characterised by a high percentage of foraminifera in the sediment, but a very low diversity in species. The assemblage is almost exclusively composed of the species *Heterohelix moremani.* This biserial, planktonic foraminifera has been described by Nederbragt *et al* as an opportunist that thrives in extreme conditions [118]. Nederbragt *et al* observe it diversifying during ocean anoxic events, with a maximum abundance during the late Cenomanian ocean anoxic event 2 [118]. Keller *et al* find *Heterohelix moremani* in sections of the Cenomanian/Turonian transition at Eastbourne and suggest that this indicates low oxygen conditions [84].

By contrast the light coloured Tarfaya sediment has a lower overall percentage of foraminiferas, but a greater diversity of species. *Heterohelix moremani* is still dominant but it is joined by common surface dwellers such as *Heterohelix globulosa* and *Whiteinella* sp..

The distinct changes in diversity and abundance of foraminifera between areas of light and dark sediment support the idea of different palaeoenvironments during sediment deposition. A dominance of *Heterohelix moremani* along with the nannofossil species *Eprolithus floralis* strongly suggests an extreme environment during dark sediment deposition. This could have been caused by intense upwelling and is discussed in section 6.5. Surface waters were likely to have been very cold, nutrient rich, turbulent and possibly low in oxygen.

During light sediment deposition the greater diversity in both nannofossils and foraminifera, and the appearance of more moderate species such as *Whiteinella* sp., suggests a milder environment. The fast rate of sedimentation (see section 4.7.4) still suggests a high productivity environment, but one that is less extreme and supports a greater diversity of species.

6.4.8 Radiolarian

Radiolarian are not common in the Tarfaya sediments. Thin section work showed a relationship between radiolarian occurrence and sediment colour (see section 4.7). In dark and intermediate coloured sediments radiolarian were extremely rare, whereas in light sediment they made up a noticable component of the sediment. Identification of the radiolarian species was not possible but their internal structure indicated that they were high latitude/cold water species (Thurow, pers. comm.).

It is likely that silicate organisms such as radiolarian and diatoms were dissolved out of the Tarfaya sediment. Only the most robust structures were likely to have been replaced by calcite and so the radiolarian record we see today is probably not representative of radiolarian occurrence at the time. Nonetheless, it is interesting that radiolarians were definitely present during light sediment deposition. Foraminifera and nannofossil evidence point towards this being a time of greater diversity and perhaps a less extreme environment. The presence of radiolarian in the light sediment backs up the idea that diversity was greater during intervals of light sediment deposition.

6.4.9 Bivalves

Bivalves also showed a change in distribution relating to the sediment colour (see section 4.7). *Inoceramus* and a very thin shelled species were relatively common in areas of dark sediment, but diminished in number as the sediment became lighter. Assuming that bottom waters were anoxic most of the time, it is likely that all bivalves were surface dwellers.

Once again the sharp difference in distribution between dark and light sediment supports the idea of widely differing environments that supported a different range of taxa.

6.4.10 Shannon Weaver diversity index (H(S)) and Equatability (E)

H(S) values vary in the Tarfaya nannofossil assemblage from 1.17 to 2.58 (see appendix B.3). E values range from 0.19 to 0.65 (see appendix B.3). Both H(S) and E values are considerably lower than those calculated by Watkins for the Cenomanian Greenhorn limestone (H(S) ranged from 2.34 to 3.03 and E from 0.688 to 0.837) [187], and by Fisher & Hay for the Cenomanian U.S. Interior (H(S) ranged from 2.1 to 3.1 and E from 0.6 to 0.8) [51]. Watkins (1989) [187] found

Shannon Diversity values equal to or greater than 2.7 associated with chalks ($\geq$ 70% carbonate), whereas values less than 2.7 were associated with marls ($\leq$ 70% carbonate). He interpreted the lower values to represent the less stable conditions during marl deposition.

The extremely low values of H(S) and E for the Tarfaya basin indicate that the nannofossil assemblages were very low diversity and often dominated by a very small number of species. Shannon Diversity takes both the number of species and the equitability of their distribution into account and so it can be cautiously used to directly compare samples. The values of H(S) and E for the most diverse and equitable Tarfaya nannofossil assemblages are comparable to the least diverse and equitable assemblages that both Watkins (1989) and Fisher & Hay (1999) recorded. If H(S) and E are taken as absolute measures of environmental stability, then comparisons with Watkins (1989) [187] and Fisher & Hay (1999) [51] suggest that the Tarfaya environment ranged from being fairly unstable to very unstable. By this measure the Tarfaya environment really was unusual and very extreme.

6.5 Two productivity regimes in the Tarfaya basin

The results from the previous sections all point towards the existence of two different productivity regimes during the Cenomanian in the Tarfaya basin. Based on the results from this research, the sedimentological characteristics of each productivity regime is summarised in the following paragraphs.

6.5.1 Regime 1 - Extreme conditions

Regime one is characterised by dark coloured sediment (generally with sediment greyscale values greater than 135), high percentages of organic carbon (usually greater than 10%) and low percentages of calcium carbonate (usually less than 65%). The sediment comprises thin light/dark couplets (average thickness of 30μm) made up from clearly defined layers of faecal pellets and dark organic matter. The couplets are relatively distinct and continuous over at least a few centimetres. Faecal pellets are elongated in shape and generally small (average size 150μm by 20μm). Foraminifera are small, abundant and dominated by the species *Heterohelix moremani.* Layers containing a high proportion of small bivalves are also relatively frequent. Calcareous nannofossils are dominated by the six core species (see section 4.6), in particular, *E. floralis* is extremely abundant. Radiolarian are not observed. Diversity of both nannofossils and other taxa is low.

6.5.2 Regime 2 - Moderate conditions

Regime two is characterised by light coloured sediment (sediment greyscale values generally less than 135), low percentages of organic carbon (often less than 5%) and high percentages of calcium carbonate (usually greater than 65%). The sediment comprises indistinct light/dark couplets that are much thicker than those in regime one (average thickness 80μm). Again couplets are made up from light coloured faecal pellets and dark organics. However the faecal pellets are much larger than in regime one (average size 300μm by 100μm) and this means that the couplets vary in thickness as the lamina follow the shape of the faecal pellets. For this reason the couplets are difficult to follow laterally and appear much less distinct. Foraminifera are more diverse than in regime one with at least 3 dominant species. Bivalves are rarely seen. Radiolarians make up a small, but significant proportion of the fauna. Calcareous nannofossils show a more even distribution of species including all the common and periodically common species (see section 4.6). Both *Tranolithus* sp. and *S. horticus* become important. Diversity of nannofossils and other taxa is high compared to regime one.

6.5.3 Environmental Interpretation

Einsele and Wiedmann suggested that the Tarfaya, Cenomanian black shales represented the first occurrence of oceanic upwelling in the newly formed South Atlantic Ocean [42]. This research has taken a detailed look at the black shales in order to investigate the palaeoenvironment and identified differing intensities in the upwelling. All the hallmarks of oceanic upwelling, including high percentages of organic carbon, and high productivity microfossils, are present in the Tarfaya sediments at all times. However the make up of the sediment does change its proportions in a cyclical pattern, suggesting that the rate of upwelling varied over time.

The characteristics of the sediment in regime 1 suggest that upwelling was very intense, bringing large volumes of cold, nutrient rich water to the surface. In particular the low diversity of calcareous nannofossils and foraminifera point to an extreme environment that few species could take advantage of. The high percentages of organic carbon are likely to be due to a fast rate of sedimentation creating an oxygen minimum layer above the sea floor and encouraging the preservation of organic carbon. Such extreme upwelling is likely to have been driven by strong trade winds along the Northeast African margin.

In contrast the characteristics of the sediment in regime 2 hint at more moderate conditions. In particular the greater diversity of species and the continuing high to moderate productivity levels suggest mild water temperatures and a reasonably plentiful nutrient supply. Organic carbon percentages are still high indicating that a sea floor oxygen minimum layer is still likely to have existed. However there are two places were bioturbation is visible in the sediment for short periods, showing that this oxygen minimum zone was more transient and that sedimentation rates were probably lower than in regime 1. These conditions are likely to have been created by a reduction in the trade wind strength along the Northeast African margin, resulting in weaker oceanic upwelling.

6.5.4 Mechanism for changing intensity of upwelling

In the Tarfaya Basin the intensity of the coastal upwelling is thought to have been strongly influenced by the strength of the trade winds. It is likely that the driving force behind change in sedimentary regimes in the Tarfaya Basin was change in trade wind strength over the Tarfaya region. Changing the strength or location of the trade winds is caused by a change in intensity or location of the Hadley cell circulation. Possible mechanisms to cause changes in Hadley cell circulation are discussed in section 2.5.2.

Annual variations were probably caused by the movement of the Hadley cell north and south (see section 2.5). While longer term changes in sedimentary regime observed in the Tarfaya Basin strongly suggests a significant change in upwelling intensity linked to the obliquity cycle. Unfortunately the sediments do not reveal how the obliquity cycle is linked to the change in upwelling intensity and we can only speculate about this matter.

One possibility is that orbitally controlled variations in incoming solar energy on a Milankovitch timescale caused a change in the global latitudinal temperature gradient. Most research suggests that there were no permanent ice sheets at high latitudes at this time [121], [74], [122]. However Gale 2002, [59], has recently found evidence for a short lived cold event in the mid Cenomanian, where the rapidity and magnitude of sea-level fall and cooling are suggestive of glacioeuustatic control. If there were ice sheets then changes in global latitudinal temperature gradient will have been intensified by ice sheet albedo feedback mechanisms. If, however, there were no ice sheets then land distribution is likely to have been the most important factor. At this time in the Earth's history, even a small change in latitudinal temperature gradient may have had a magnified effect on the intensity of the Hadley circulation due to the close proximity of many large landmasses. An increase in latitudinal temperature gradient is likely to have intensified the Hadley circulation (due to greater thermal and pressure gradients) and strengthened trade winds. However it is impossible to estimate precisely what drove the changes in upwelling over the Tarfaya Basin as it may have been strongly effected by local conditions (such as the size of the basin and the topography of the nearby land).

The dark sediment (regime 1) appears to have experienced the strongest upwelling conditions and so it is likely that this was deposited during a time of strong trade winds, intense Hadley circulation and a high equator to pole temperature gradient. In contrast the light sediment (regime 2) experienced weaker upwelling conditions, probably driven by weaker trade winds, a more moderate Hadley circulation and a lower global latitudinal temperature gradient.

7

Conclusions and Further Work

This chapter summarises the main conclusions of this high resolution study into the characteristics and environmental interpretations of the Cenomanian Tarfaya basin sediments. It also suggests possible avenues of further research that would be interesting to investigate. The study has integrated calcareous nannofossil data, geochemical studies and detailed examination of sediment colour to provide new information on the high frequency changes occurring in the Cenomanian greenhouse climatic environment. In particular calcareous nannofossil work explores temporal palaeoproductivity patterns in the Tethys Ocean and provides evidence for a correlation between Milankovitch cycles and changes in productivity.

7.1 Conclusions

Sub-Milankovitch cycles were not found in the greyscale record. Either this is because sub-Milankovitch cycles did not exist at this time, or because the greyscale record was an inappropriate proxy to record short term cycles. Time series analysis work hinted at the existence of a SOC like sedimentary system in the Tarfaya basin. This implies that the detailed sedimentary structure was predominantly influenced by internal mechanisms such as water turbulence and particle flocculation rather than external forcing factors such as global climate and ocean currents. In particular it was noticed that the lighter areas of sediment were *noisier* than the darker areas of sediment indicating a higher degree of noise within the system during times of light sediment deposition.

Thin section work allowed recognition of individual lamina couplets. An approximation of sediment accumulation rate was made by estimating the number of lamina in one obliquity cycle. Assuming that the major changes in greyscale are related to the obliquity cycle and can be dated to be 40000 years in duration, it was possible to estimate that individual lamina couplets represent time scales of six months to one year.

Two productivity regimes were identified that appear to be correlated to the obliquity cycle. Regime one is characterised by dark coloured sediment, a high percentage of organic carbon, low nannofossil diversity and blooms of the species *Eprolithus floralis.* This is interpreted to represent extreme productivity, induced by very strong coastal upwelling conditions. Regime two is characterised by light coloured sediment, lower percentages of organic carbon and a more diverse calcareous nannofossil assemblage. This is interpreted to represent moderate to high productivity under moderate coastal upwelling conditions.

E. floralis was identified as a species which thrives in certain extreme environments. In this case it would appear that cold, nutrient rich, and potentially turbulent water conditions were ideal for *E. floralis* to bloom at regular intervals.

7.2 Further work

The Cenomanian Tarfaya basin sediments are unique in terms of their high resolution and excellently preserved calcareous nannofossils during a greenhouse mode climate system. This study has revealed their potential to investigate oceanic productivity and high frequency climate variability during this period. More information can be extracted from these sediments and the following paragraphs suggest further interesting lines of research.

A higher resolution calcareous nannofossil study would be very worthwhile. Ideally it would be interesting to carry out a lamina by lamina study, similar to that done by Thomsen on the lower Cretaceous Munk Marl beds [177], [178]. This would reveal the frequency of the *E. floralis* blooms and identify any cyclicty.

Further SEM and BSEI work would uncover details of the sediment architecture and would probably be the best way to carry out a high resolution calcareous nannofossil study. In addition it would be interesting to accompany the high resolution nannofossil work with a quantitative study of the foraminifera, radiolarian and bivalves.

To be useful at the lamina scale the digital sediment colour analysis (DSCA) needs to be done at a higher resolution. Possibly the best way to do this would be to scan BSEI images or use photomicroscopy. To pick out light/dark couplet cycles would require sampling at around 6000 pixels per inch; something that is currently not possible on an ordinary flat bed scanner. A higher resolution greyscale record would be more likely to pick out high frequency cycles at the decadal to centennial scale. In addition it would be interesting to compare greyscale records from one particular interval in a number of different cores. It would then be possible to determine whether the sub-structure visible in each record was consistent, and therefore likely to be an environmental signal, or simply a local noise effect.

Given that a number of cores have been drilled in the Tarfaya Basin it would be interesting to do a detailed comparison of greyscale records from one interval to determine whether the sub-structure visible in each record is consistent.

Finally, a comparative study with modern icehouse climate sediments may shed light on the major differences between processes acting and controlling greenhouse and icehouse climate modes. One suitable area for comparison, that has already been drilled, is ODP site 1002, in the Cariaco Basin (Venezuela). These sediments are finely laminated and were also deposited under anoxic water conditions.

It would be interesting to carry out a similar greyscale study on modern laminated sediments to try and establish what the greyscale can tell us about the mechanisms of sedimentation occurring. More information is available about the climate, ocean currents, and water stratification during modern times so a greyscale study on modern laminated sediments would serve as a control and act as a benchmark to which more ancient sediments could be compared.

Appendix A - Preparation notes

A.1 Glued rock

Some of the rock sections broke while they were being cut. When the pieces were small they were glued back on again to avoid losing the piece. The following is a list of the pieces that were glued together using the method described in Section 3.1.1.

The middle of piece 2B

The top of piece 2D

Four glued layers in the top of piece 3G

Between 6B and 6C

Towards base of 6I2

Very top of piece 10D

Very top of piece 11F

Top of 15D7

Towards bottom of piece 17A1

At 2 places in piece 18A/B

A.2 Overlap

The rock slabs were cut from the quarry with overlap between each slab. The amount of overlap was usually visible and could be calculated precisely by matching up lamina. Figures A.1 to A.3 are a stratigraphic section of the quarry detailing where the slabs were taken from. The section show the variation between laminated areas, massive areas, nodular layers and bioturbated regions. The lab notes written on 12th April 2001, detailing the amount of overlap between rock pieces, are reproduced below.

A.2.1 Slab 18

Unable to match any overlap, probably there is a gap between this and slab 17 so slab 18 was not used.

A.2.2 Slab 17

Complete overlap with slab 15, easy to match up with nodular layers in slab 15. The pieces from slab 17 were not used due to their replication in slab 15.

A.2.3 Slab 16

Missing, possibly not taken.

A.2.4 Slab 15

Consists of 11 pieces labelled from top to bottom as follows, 15D7, 15D6, 15D5, 15D4, 15D321, 15C, 15B2, 15B1, 15A3, 15A2, 15A1. Piece 15D7 was used as the top of the section. Overlap of 3,5cm between 15D6 and 15D5 which can be seen by matching up faecal pellet layers. Overlap of 5.3cm between 15D4 and 15D321. 15D321 contains one of the nodular layers seem in slab 17.

A.2.5 Slab 14

Consists of 9 pieces labelled from top to bottom as follows, 14K, 14J, 14H/I, 14G3, 14G3/2, 14F/G1, 14D/E, 14C, 14A1/2/3. There is an overlap of 13cm between

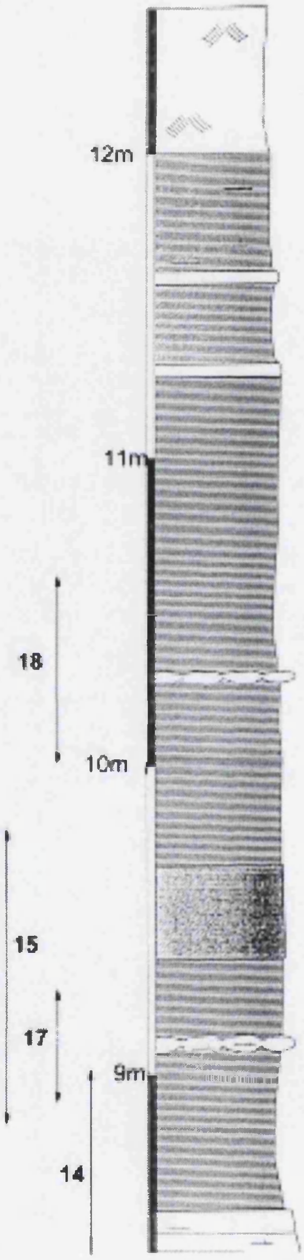

Figure A.1: Stratigraphic section of quarry - upper interval.

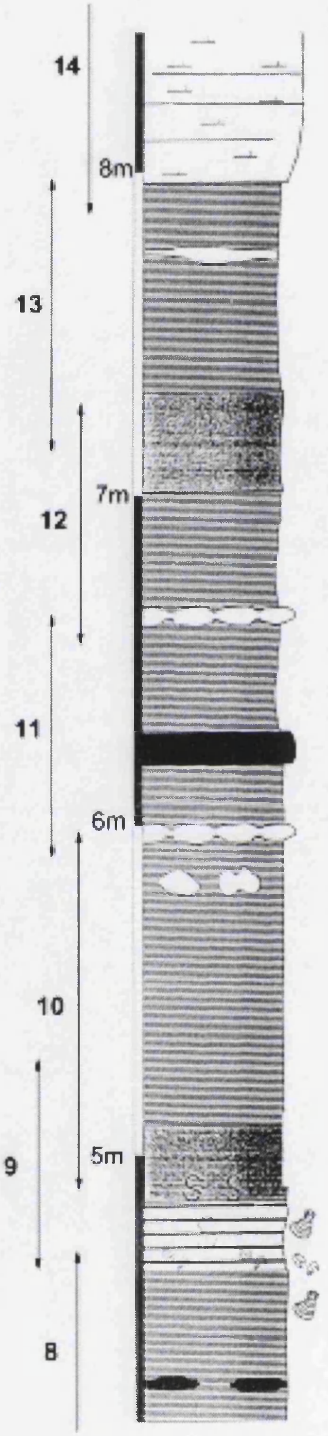

Figure A.2: Stratigraphic section of quarry - middle interval.

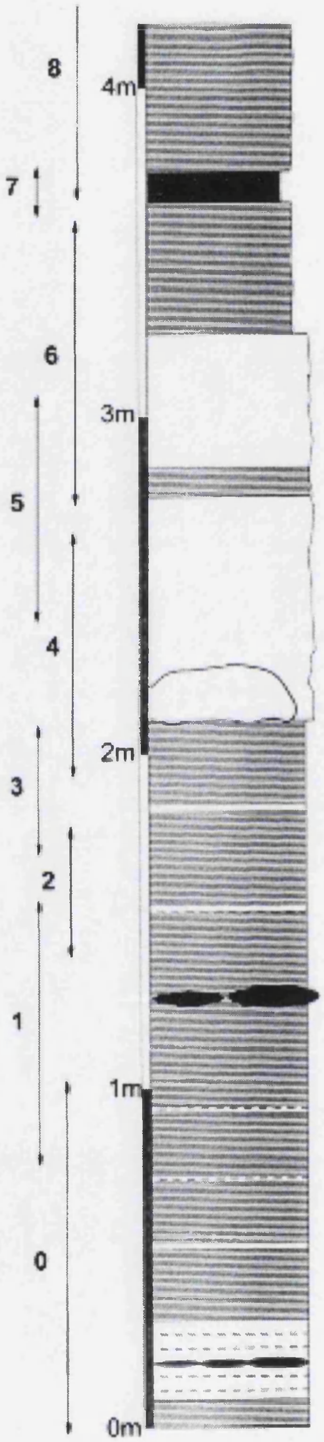

Figure A.3: Stratigraphic section of quarry - lower interval.

slab 14 and slab 15. The top pieces of slab 14 were removed in preference to the bottom of slab 15 since they had salt precipitation on them. The unused pieces were 14K and the top 0.7cm of 14J down to a prominent faecal pellet layer. Only the top 1.5cm of 14G3 were used as the remainder overlapped with 14G2/3.

A.2.6 Slab 13

Consists of 5 pieces labelled from top to bottom as follows, 13B6, 13B2/5, 13B1, 13A2, 13A1/0. Overlap was difficult to estimate as the pieces in slab 14 had been cut at a different angle to those in slab 13. However it was possible to match up 3 prominent faecal pellet layers in piece 13B6 with the same layers in piece 14A1. The top 2.4cm of piece 13B6 accounted for all the overlap between the slabs.

A.2.7 Slab 12

Consists of 5 pieces labelled from top to bottom as follows, 12E, 12D1/2, 12C, 12B, 12A. Overlap extremely difficult to estimate as it occurs in a bioturbated area. Approximately 9cm of overlap was estimated between the two slabs meaning that measurements were resumed again from 2.4cm down piece 12D1/2.

A.2.8 Slab 11

Consists of 11 pieces labelled from top to bottom as follows, 11H2, 11H1, 11G, 11F, 11E1/2, 11C/D, 11B, 11A4, 11A3, 11A2, 11A1. Easy to calculate overlap using the lamina. About 21cm of overlap, measurements start again from 4.9cm down on piece 11G.

A.2.9 Slab 10

Consists of 9 pieces labelled from top to bottom as follows, 10H2, 10H1, 10G, 10F, 10E, 10D, 10C, 10B, 10A1/2. Overlap computed by matching up nodular layers. Measurements start from 2.6cm down on piece 10E.

A.2.10 Slab 9

Consists of 9 pieces labelled from top to bottom as follows, 9G, 9F2/1, 9E3, 9E2, 9E1, 9E0, 9D1/2, 9A2/B/C, 9A1. 9.3cm down on piece 10A1/2 matches up with 0.8cm down on piece 9E0. These slabs were matched by comparing the bioturbated areas in pieces 9E0 and 9D1/2 with that in piece 10D. Measurements resume from 0.8cm down on piece 9E0.

A.2.11 Slab 8

Consists of 11 pieces labelled from top to bottom as follows, 8K/L, 8J, 8G2, 8G1, 8F2, 8F1, 8E, 8D2, 8D1, 8B/C, 8A. These pieces had been cut at an acute angle making it difficult to see overlap with slab 9 using the naked eye. However it was possible to match up two dark layers towards the top of piece 8K/L with the same layers in piece 9A1. Measurements were resumed from 3.7cm down on piece 8K/L.

A.2.12 Slab 7

Consists of 2 pieces labelled from top to bottom as follows, 7B, 7A. These pieces were cut to avoid chert layers in slabs 8 and 6. Measurements were terminated at 9.5cm down on piece 8D1 and started 3.7cm down on piece 7B. They were then terminated again 9.9cm down on piece 7A and resumed at the top of piece 8A.

A.2.13 Slab 6

Consists of 9 pieces labelled from top to bottom as follows, 6J, 6I2, 6I1, 6H2, 6H1, 6F1/2, 6E/F, 6B/C/D, 6A. It was possible to match up light layers in piece 6I2 with the same layers in piece 8A. Measurements were terminated at 4.7cm down on piece 8A and resumed at 5.4cm down on piece 6I2.

A.2.14 Slab 5

Consists of 5 pieces labelled from top to bottom as follows, 5E, 5D, 5C, 5B, 5A. Matched a break in sedimentation where an abrupt change from dark to light sediment is visible. This occurred at 18.5cm down on piece 6B/C/D and 0.8cm down on piece 5E respectively.

A.2.15 Slab 4

Consists of 3 pieces labelled from top to bottom as follows, 4C/D, 4B, 4A. Overlap was difficult to see, attempted to match up lamina. Terminated measurements at 11.6cm down on piece 5B and resumed at 7.1cm on piece 4C/D.

A.2.16 Slab 3

Consists of 4 pieces labelled from top to bottom as follows, 3G, 3E, 3D, 3A/B/C. Overlap is extremely easy to see with obvious colour changes that can be matched. Measurements terminated at 14.8cm on piece 4A and resumed at 12.1cm down on piece 3G.

A.2.17 Slab 2

Consists of 4 pieces labelled from top to bottom as follows, 2D2, 2D1, 2B/C, 2A. Overlap easy to see as can match a white band in 2D2 with the same band in 3A/B/C. Measurements terminated at 5.8cm on piece 3A/B/C and resumed at 3.7cm on piece 2D2.

A.2.18 Slab 1

Consists of 10 pieces labelled from top to bottom as follows, K2, J2, I2, H2, G2, F2, E/F2, D2, C2, A/B2. Overlap obvious with a white band in K2 matching with one in 2A. Measurements resumed at 1.7cm down in piece K2.

A.2.19 Slab 0

Consists of 10 pieces labelled from top to bottom as follows, 0I, 0H2, 0H1, 0F2/G, 0F1/2, 0E2, 0E1, 0D2/1, 0A/C, 0A/B. Plenty of obvious overlap between slab 1 and slab 0. Measurements terminated at 22.3cm down on piece A/B2 and resumed at 2.6cm down on OE1. In addition piece 0A/B is completely overlapped by piece 0A/C so is unnecessary.

A.3 Geochemistry Results

Table A.1: Table of carbon geochemistry results.

Depth/cm	C_{TOT}	C_{CaCO_3}	$C_{organic}$	average greyscale	$C_{organic}+ C_{CaCO_3}$	% Si estimate
20.1(youngest sample)	18.8	60.0	11.6	155.2	71.6	28.4
40.6	18.2	46.7	12.6	144.6	59.3	40.7
60.8	17.3	55.0	10.7	140.2	65.7	34.3
80.6	16.1	59.6	8.95	144	68.5	31.5
93.6	14.7	63.9	7.03	137.4	70.9	29.1
109.5	13.1	81.9	3.27	128.6	85.2	14.8
130.2	13.2	80.7	3.52	115.9	84.2	15.8
148.4	13.3	75.8	4.2	113.5	80	20
161.2	14.4	73.4	5.59	123.7	79	21
181.9	16.7	72.7	7.98	136.4	80.6	19.4
198.6	20.3	66.7	12.3	133	79	21
216	19.2	70.8	10.7	131.7	81.5	18.5
231.7	17.6	57.5	10.7	147	68.2	31.8
251.8	21.9	69.2	13.6	147.2	82.8	17.2
271.7	19.4	75.8	10.3	146	86.1	13.9
291.5	24.4	58.3	17.4	166	75.7	24.3
311.5	14.8	76.9	5.57	152	82.5	17.5
331	18.9	58.3	11.9	166	70.2	29.8
347.6	22.4	60.8	15.1	151	75.9	24.1
361.2	24.3	54.2	17.8	154	72	28
380.8	21.6	55.8	14.9	146	70.7	29.3
400	21.9	63.3	14.3	142	77.6	22.4
420	23.9	53.3	17.5	146	70.8	29.2
438.1	21.1	63.3	13.5	138	76.8	23.2

continued next page

Table A.1: *continued*

Depth/cm	C_{TOT}	C_{CaCO_3}	$C_{organic}$	average greyscale	$C_{organic}$+ C_{CaCO_3}	% Si estimate
458.3	15.8	79.6	6.25	121	85.8	14.2
483.9	15.8	78.4	6.4	120	84.8	15.2
502.2	22.8	69.2	14.5	133	83.7	16.3
522.3	17.1	73.5	8.28	113	81.8	18.2
538.8	19.7	67.5	11.6	136	79.1	20.9
554.8	20.2	74.2	11.3	133	85.5	14.5
565	20.8	74.2	11.9	127	86.1	13.9
584.1	21.3	69.2	13	151	82.2	17.8
605.1	16.4	79.7	6.84	125	86.5	13.5
625.1	13.5	79.2	3.99	102	83.2	16.8
645.1	14.3	82.9	4.35	115	87.3	12.7
660.3	13.3	86.9	2.87	104	89.8	10.2
696.7	12.9	90.9	1.99	85	92.9	7.1
719.3	14.6	90.4	3.75	98	94.2	5.8
743.3	19.5	75.8	10.4	140	86.2	13.8
754	15.5	90.6	4.63	106	95.2	4.8
764.2	18	70.8	9.5	149	80.3	19.7
786.2	18.2	70.4	9.75	145	80.2	19.8
804.1	17.3	79.6	7.75	141	87.3	12.7
824.3	20.8	76.7	11.6	134	88.3	11.7
844.3	18.5	74.1	9.61	134	83.7	16.3
855.8	17.9	84.7	7.74	131	92.4	7.6
875.8	16.7	80.2	7.07	115	87.3	12.7
893.5	19.5	75.8	10.4	136	86.2	13.8
912.9	17.9	76.7	8.69	132	85.4	14.6
932.9	16.2	80.8	6.5	147	87.3	12.7
953.2	13.2	92.1	2.15	98	94.2	5.8

continued next page

Table A.1: *continued*

Depth/cm	C_{TOT}	C_{CaCO_3}	$C_{organic}$	average greyscale	$C_{organic}+C_{CaCO_3}$	% Si estimate
972.8 (oldest sample)	13.9	92.8	2.76	108	95.6	4.4

B

Appendix B - Nannofossil results and statistics

B.1 Nannofossil species

The following is a list of all of the calcareous nannofossil species observed in the Tarfaya section.

Biscutum ellipticum

Broinsonia signata

Chiastozygus trabalis

Corollithion exiguum

Corollithion signum

Cretarhabdus conicus

Cribrosphaerella ehrenbergii

Eiffellithus turriseiffeli

Eprolithus floralis

Gartnerago obliquum

Helicolithus trabeculaes

Helicolithus turonicus

Lithraphidites carniolensis

Loxolithus armilla

Manivitella pemmatoidea

Prediscosphaera spp.

Radiolithus planus

Reinhardtites anthophorus

Retecapsa angustiforata

Retecapsa crenulata

Rhagodiscus angustus

Rhagodiscus asper

Rotelapillus crenulatus

Sollasites horticus

Staurolithites laffittei

Stoverius achylosus

Tegumentum stradneri

Tranolithus minimus

Tranolithus orionatus

Watznaueria barnesae

Zeugrhabdotus embergeri

Zeugrhabdotus spp.

B.2 Nannofossil counts

The following table presents the percent abundance with increasing depth, for all the major species of nannofossil observed in the Tarfaya sediments.

Table B.1: Table of nannofossil percentage abundance values from nannofossil microscope counts. Includes depth of sample and average greyscale value of sample.

sample name	depth/cm	greyscale	*Biscutum ellipticum*	*Eiffellithus turriseiffelii*	*Eprolithus floralis*	*Helicolithus turonicus*	*Lithraphidites carniolensis*	*Prediscophaera* spp.	*Sollasites horticus*	*Staurolithites laffittei*	*Tranolithus minimus*	*Tranolithus orionatus*	*Tranolithus* summed	*Watznaueria barnesae*	*Zeugrhabdotus* spp.
retarf5	20.1	153	9.2	9.2	6.6	0.6	0.6	9.2	1.6	2.9	1.3	3.8	5.1	19.4	12.4
retarf6	30.6	143	12.9	10.7	23.0	0.3	3.2	7.1	1.0	1.6	0.7	3.6	4.2	11.7	11.0
retarf7	40.6	147	16.9	12.1	4.3	0.3	3.9	7.8	2.0	1.0	4.9	4.9	9.8	8.8	18.6
retarf8	50.7	144	11.6	9.3	2.6	0.3	2.3	11.9	1.0	2.9	6.8	7.4	14.2	13.5	15.4
retarf9	60.8	143	17.2	9.2	6.1	0.7	5.0	10.2	2.6	1.0	1.3	4.0	5.3	11.9	17.5
retarf10	71.0	134	14.1	11.9	5.8	0.3	3.5	8.7	2.6	0.6	3.9	4.8	8.7	16.4	18.3
Tarf 11	80.6	143	8.2	11.8	4.9	2.0	3.9	7.5	2.0	2.3	2.3	9.2	11.5	22.3	13.4
Tarf 12	83.3	147	5.7	6.0	18.7	1.3	1.3	7.3	0.0	3.0	1.3	8.3	9.7	27.7	13.0
Tarf 13	92.2	136	14.3	14.6	4.6	1.6	3.6	5.2	0.6	2.9	3.2	5.2	8.4	19.8	15.6

continued next page

Table B.1: *continued*

sample name	depth/cm	greyscale	*Biscutum ellipticum*	*Eiffellithus turriseiffelii*	*Eprolithus floralis*	*Helicolithus turonicus*	*Lithraphidites carniolensis*	*Prediscophaera* spp.	*Sollasites horticus*	*Staurolithites laffittei*	*Tranolithus minimus*	*Tranolithus orionatus*	*Tranolithus* summed	*Watznaueria barnesae*	*Zeugrhabdotus* spp.
Tarf 14	99.5	128	17.8	8.2	3.6	2.6	1.6	4.3	1.3	1.6	6.6	13.8	20.4	18.8	11.5
Tarf 15	108.8	131	8.7	13.6	6.2	3.6	3.2	4.9	2.3	3.2	6.8	8.4	15.2	20.1	11.7
Tarf 16	119.4	117	14.6	8.6	2.3	5.0	2.7	5.3	5.3	3.3	6.6	9.0	15.6	18.9	11.6
Tarf 17	128.4	119	16.9	9.3	1.7	3.3	3.0	5.0	3.3	3.3	4.3	9.6	13.9	22.2	9.9
Tarf 18	137.2	112	15.0	9.8	2.3	3.9	3.6	7.5	2.0	2.9	6.5	12.4	18.9	14.0	12.1
Tarf 19	145.4	120	12.7	14.3	4.3	3.0	3.7	7.3	1.7	2.3	3.7	16.0	19.7	15.0	9.3
Tarf 20	152.0	112	14.1	12.3	2.3	0.9	3.1	7.0	3.1	3.5	6.6	10.6	17.2	17.6	13.7
Tarf 21	161.0	114	11.4	13.6	4.1	2.5	3.5	6.9	0.3	1.3	3.5	16.1	19.6	17.7	11.0
Tarf 22	170.5	127	13.7	9.5	6.7	2.9	3.8	9.2	2.5	4.8	1.6	7.6	9.2	22.2	11.1
Tarf 23	181.8	137	14.0	10.3	7.0	0.7	2.0	9.0	3.7	2.7	4.7	13.0	17.7	11.0	15.7
Tarf 24	191.6	137	14.8	8.7	14.8	2.9	1.3	7.4	1.3	2.9	4.5	9.4	13.9	12.9	11.9

continued next page

Table B.1: *continued*

sample name	depth/cm	greyscale	*Biscutum ellipticum*	*Eiffellithus turriseiffelii*	*Eprolithus floralis*	*Helicolithus turonicus*	*Lithraphidites carniolensis*	*Prediscophaera* spp.	*Sollasites horticus*	*Staurolithites laffittei*	*Tranolithus minimus*	*Tranolithus orionatus*	*Tranolithus* summed	*Watznaueria barnesae*	*Zeugrhabdotus* spp.
Tarf 25	198.5	139	27.1	8.5	22.9	1.6	0.7	6.2	0.7	0.3	2.0	1.3	3.3	11.4	11.8
Tarf 26	206.0	139	15.7	10.8	31.1	0.0	0.9	8.6	0.9	0.3	2.5	1.8	4.3	9.2	14.2
Tarf 27	215.5	138	22.2	7.3	27.8	0.6	1.9	9.2	1.3	0.6	1.6	2.8	4.4	6.0	13.0
Tarf 28	225.4	150	19.2	8.8	25.1	1.6	3.3	4.9	1.0	1.0	2.0	3.9	5.9	11.1	13.7
Tarf 29	231.7	148	8.9	8.6	52.5	0.3	1.0	4.6	0.0	0.0	1.0	2.6	3.6	6.9	10.6
Tarf 30	241.7	158	12.0	8.0	41.7	0.0	0.3	7.3	0.3	0.0	2.0	1.0	3.0	8.3	16.0
Tarf 31	251.8	145	11.6	6.6	38.7	0.0	0.0	8.6	1.0	2.3	2.0	1.3	3.3	5.0	17.5
Tarf 32	261.8	156	12.2	7.1	36.7	0.3	0.0	6.4	1.6	0.6	3.2	2.9	6.1	10.6	12.2
Tarf 33	271.7	141	9.9	6.4	47.4	0.3	1.3	2.2	0.6	1.3	2.9	4.2	7.1	7.1	9.3
Tarf 34	281.7	161	20.6	7.7	30.2	1.0	0.3	5.5	1.6	1.0	3.2	1.3	4.5	8.7	11.6
Tarf 35	291.5	168	22.3	8.0	25.0	0.0	1.0	7.3	1.3	1.0	1.7	1.7	3.3	6.0	18.0

continued next page

Table B.1: *continued*

sample name	depth/cm	greyscale	*Biscutum ellipticum*	*Eiffellithus turriseiffelii*	*Eprolithus floralis*	*Helicolithus turonicus*	*Lithraphidites carniolensis*	*Prediscophaera* spp.	*Sollasites horticus*	*Staurolithites laffittei*	*Tranolithus minimus*	*Tranolithus orionatus*	*Tranolithus* summed	*Watznaueria barnesae*	*Zeugrhabdotus* spp.
Tarf 36	301.5	172	21.2	10.3	22.5	0.0	0.3	7.1	0.6	1.9	1.9	1.0	2.9	10.9	14.1
Tarf 37	311.5	149	5.0	3.3	73.6	0.3	0.0	4.0	0.0	0.3	1.0	1.3	2.3	3.6	5.0
Tarf 38	320.9	151	18.1	5.1	39.0	5.4	1.0	4.4	1.0	0.6	0.6	1.0	1.6	3.5	13.0
Tarf 39	330.9	166	17.3	6.8	36.8	3.9	1.3	5.5	1.0	0.7	0.3	0.0	0.3	8.8	13.4
Tarf 40	337.8	136	9.6	7.3	35.1	8.3	0.3	5.8	0.6	0.3	4.2	2.2	6.4	4.8	15.7
Tarf 41	347.6	147	17.3	8.8	19.9	2.6	0.7	6.2	1.3	3.9	2.0	2.3	4.2	12.4	15.4
Tarf 42	357.5	148	21.1	11.0	8.5	0.6	0.6	8.2	1.6	3.5	2.5	2.5	5.0	14.5	18.0
Tarf 45	361.2	154	24.4	6.8	12.4	1.3	1.3	9.8	1.0	1.3	0.7	3.3	3.9	16.0	15.0
Tarf 46	370.8	140	18.8	9.9	15.1	1.3	1.0	10.9	1.6	0.7	1.3	3.6	4.9	13.5	14.1
Tarf 47	380.8	149	20.2	5.9	27.4	0.3	0.0	5.9	1.6	0.7	1.3	0.7	2.0	15.6	12.1
Tarf48	390.3	136	21.4	7.9	24.0	0.7	0.7	6.3	1.0	2.3	1.0	2.6	3.6	11.2	11.5

continued next page

Table B.1: *continued*

sample name	depth/cm	greyscale	*Biscutum ellipticum*	*Eiffellithus turriseiffelii*	*Eprolithus floralis*	*Helicolithus turonicus*	*Lithraphidites carniolensis*	*Prediscophaera* spp.	*Sollasites horticus*	*Staurolithites laffittei*	*Tranolithus minimus*	*Tranolithus orionatus*	*Tranolithus* summed	*Watznaueria barnesae*	*Zeugrhabdotus* spp.
Tarf 49	400.0	140	17.7	10.8	5.9	1.3	0.0	8.5	1.6	1.3	3.6	3.6	7.2	16.4	22.0
Tarf 50	410.0	140	22.4	10.2	11.2	0.3	0.7	9.5	1.6	1.3	2.0	3.6	5.6	7.6	20.7
Tarf 51	420.0	148	10.8	7.3	39.2	1.3	0.0	5.4	0.0	2.5	1.3	2.5	3.8	8.3	13.7
Tarf 56	428.1	132	12.1	10.8	21.6	1.0	2.0	7.2	0.0	1.6	2.3	1.3	3.6	17.0	16.0
Tarf 57	438.1	138	22.4	10.9	9.2	0.7	0.3	11.2	1.0	0.7	0.7	5.0	5.6	13.2	18.2
Tarf 58	448.3	133	26.2	13.6	2.0	1.0	0.3	8.6	2.0	2.0	2.0	7.0	8.9	11.3	15.2
Tarf 59	458.3	121	16.9	14.7	1.6	1.3	0.7	7.2	2.3	2.0	3.6	12.4	16.0	15.3	14.3
Tarf 60	464.8	120	15.7	11.8	8.2	2.6	0.7	8.9	2.6	3.9	3.3	7.5	10.8	14.4	14.8
Tarf 61	483.5	118	17.8	13.3	14.0	0.3	0.6	8.7	1.0	0.6	3.9	8.4	12.3	10.7	13.9
Tarf 62	492.2	135	17.5	12.7	5.1	1.9	0.6	8.3	1.6	4.1	2.9	6.4	9.2	12.7	17.8
Tarf 63	502.1	133	21.9	11.3	8.8	1.9	0.3	8.2	1.3	2.8	1.6	7.2	8.8	14.4	15.0

continued next page

Table B.1: *continued*

sample name	depth/cm	greyscale	*Biscutum ellipticum*	*Eiffellithus turriseiffelii*	*Eprolithus floralis*	*Helicolithus turonicus*	*Lithraphidites carniolensis*	*Prediscophaera* spp.	*Sollasites horticus*	*Staurolithites laffittei*	*Tranolithus minimus*	*Tranolithus orionatus*	*Tranolithus* summed	*Watznaueria barnesae*	*Zeugrhabdotus* spp.
Tarf 64	511.7	127	24.2	7.7	50.0	0.0	2.5	7.1	0.9	1.8	1.5	2.8	4.3	8.0	23.9
Tarf 65	520.3	113	13.5	9.9	23.0	0.6	0.6	6.1	1.3	1.6	1.3	3.2	4.5	17.6	14.4
Tarf 66	528.8	126	14.2	12.7	18.0	0.0	2.2	5.9	0.9	1.2	0.6	1.2	1.9	20.1	13.9
Tarf 67	538.8	136	11.9	13.9	26.0	0.3	2.0	3.0	1.7	2.0	0.3	3.3	3.6	15.8	11.9
Tarf 68	548.8	139	12.9	22.6	14.0	1.3	1.3	3.8	3.1	0.9	0.0	3.8	3.8	9.1	15.4
Tarf 70	554.8	134	13.1	13.7	5.9	0.9	0.6	5.3	5.0	2.8	1.2	6.9	8.1	16.8	15.9
Tarf 71	565.0	126	12.7	10.1	18.0	1.3	0.0	8.1	3.3	1.0	0.0	2.6	2.6	20.2	14.0
Tarf 72	574.2	147	5.5	8.0	50.0	1.9	0.3	5.8	1.9	0.6	0.0	1.6	1.6	11.6	8.7
Tarf 73	584.1	152	14.3	12.2	8.5	0.6	1.8	10.4	4.0	1.2	0.3	4.9	5.2	18.3	13.4
Tarf 74	594.3	143	14.8	10.5	16.0	0.7	0.7	5.6	2.6	0.7	0.7	3.3	3.9	20.0	13.1
Tarf 75	605.1	122	6.2	4.2	49.0	0.3	0.0	3.3	3.9	3.3	2.0	4.2	6.2	6.5	11.1

continued next page

Table B.1: *continued*

sample name	depth/cm	greyscale	*Biscutum ellipticum*	*Eiffellithus turriseiffelii*	*Eprolithus floralis*	*Helicolithus turonicus*	*Lithraphidites carniolensis*	*Prediscophaera* spp.	*Sollasites horticus*	*Staurolithites laffittei*	*Tranolithus minimus*	*Tranolithus orionatus*	*Tranolithus* summed	*Watznaueria barnesae*	*Zeugrhabdotus* spp.
Tarf 76	625.0	102	7.5	7.5	43.0	1.3	0.0	5.6	2.3	1.6	2.3	2.3	4.6	10.8	10.5
Tarf 77	645.0	116	9.9	9.5	26.0	0.3	0.7	4.3	3.9	1.6	3.6	6.6	10.2	13.2	12.5
Tarf 78	665.0	89	11.7	11.0	15.0	1.3	2.3	8.3	2.0	2.3	1.7	13.3	15.0	10.7	11.7
Tarf 79	685.0	99	10.9	10.3	20.0	1.0	0.6	5.1	3.9	3.2	4.5	5.5	10.0	15.1	11.6
Tarf 80	705.0	86	19.3	9.2	11.0	0.7	0.7	7.8	6.5	2.6	3.3	6.5	9.8	15.0	12.1
Tarf 81	725.0	99	12.3	12.7	17.0	0.7	0.0	8.3	2.3	2.3	1.7	7.0	8.7	11.0	14.3
Tarf 82	745.0	126	9.2	9.9	49.0	0.3	0.0	6.3	2.0	0.7	1.7	2.0	3.6	6.3	8.6
Tarf 83	765.0	152	9.6	6.8	50.0	0.6	0.6	6.4	0.6	1.6	0.3	1.3	1.6	8.7	8.4
Tarf 84	785.0	150	14.6	13.6	18.0	0.7	2.0	9.6	1.7	0.3	0.3	1.0	1.3	16.3	12.6
Tarf 85	805.0	141	27.0	11.3	7.7	0.6	0.3	9.3	2.6	0.6	2.9	3.2	6.1	9.6	15.8
Tarf 86	825.0	139	15.3	8.8	5.5	4.9	0.3	12.7	2.3	1.3	1.6	8.8	10.4	6.2	17.2

continued next page

Table B.1: *continued*

sample name	depth/cm	greyscale	*Biscutum ellipticum*	*Eiffellithus turriseiffelii*	*Eprolithus floralis*	*Helicolithus turonicus*	*Lithraphidites carniolensis*	*Prediscophaera* spp.	*Sollasites horticus*	*Staurolithites laffittei*	*Tranolithus minimus*	*Tranolithus orionatus*	*Tranolithus* summed	*Watznaueria barnesae*	*Zeugrhabdotus* spp.
Tarf 87	845.0	118	18.4	12.1	12.0	0.3	1.3	11.8	3.0	0.7	2.0	3.6	5.6	8.9	21.6
Tarf 88	865.0	114	19.0	14.0	6.7	0.3	0.3	9.0	6.3	0.7	3.7	2.0	5.7	9.0	20.3
Tarf 89	885.0	119	15.1	10.9	13.0	0.6	0.6	10.6	3.2	0.3	1.3	6.7	8.0	14.1	13.5
Tarf 90	905.0	136	17.5	11.9	8.6	1.0	0.7	17.8	5.3	0.7	1.0	4.6	5.6	8.6	12.5
Tarf 91	925.0	156	15.3	11.5	16.0	0.0	3.2	6.7	2.6	0.3	2.9	4.2	7.0	13.4	16.6
Tarf 92	945.0	113	8.6	8.6	31.0	0.3	0.3	5.6	3.7	2.5	4.9	9.0	13.9	5.6	13.9
Tarf 93	965.0	103	8.3	9.0	39.0	0.3	1.3	4.2	5.4	1.6	6.1	9.3	15.4	3.2	8.0
Tarf 94	985.0	126	16.7	13.0	17.0	0.3	1.3	7.7	2.0	1.3	5.0	7.7	12.7	6.7	11.3
Tarf 95	992.0	127	20.3	11.8	23.0	0.0	1.0	8.8	2.9	1.0	1.0	2.6	3.6	6.9	13.4

B.3 Nannofossil diversity statistics

Table B.2: Statistics resulting from the nannofossil light microscope counts.

sample name	H(S)	E	Average nannofossil density	NIP
retarf5	2.3	0.52	12.1	0.63
retarf6	2.33	0.49	15.5	0.84
retarf7	2.44	0.55	12.3	0.12
retarf8	2.57	0.57	15.6	0.14
retarf9	2.46	0.56	20.2	0.30
retarf10	2.58	0.57	15.6	0.13
Tarf 11	2.54	0.53	16.9	-0.36
Tarf 12	2.22	0.54	6.67	0.35
Tarf 13	2.45	0.55	14.7	-0.11
Tarf 14	2.44	0.54	16.9	-0.62
Tarf 15	2.54	0.61	10.7	-0.24
Tarf 16	2.52	0.62	11.6	-0.79
Tarf 17	2.46	0.59	13.1	-0.89
Tarf 18	2.55	0.61	12.8	-0.80
Tarf 19	2.48	0.6	14.3	-0.61
Tarf 20	2.42	0.59	15.8	-0.89
Tarf 21	2.46	0.53	18.6	-0.60
Tarf 22	2.41	0.65	22.5	-0.18
Tarf 23	2.48	0.57	13	-0.38

continued next page

Table B.2: *continued*

sample name	H(S)	E	Average nannofossil density	NIP
Tarf 24	2.49	0.6	34.4	0.14
Tarf 25	2.13	0.4	34	1.07
Tarf 26	2.07	0.44	27.1	1.05
Tarf 27	2.19	0.39	24.3	0.83
Tarf 28	2.24	0.49	27.9	0.71
Tarf 29	1.69	0.36	17.8	1.30
Tarf 30	1.83	0.41	18.8	1.49
Tarf 31	1.99	0.41	27.5	1.22
Tarf 32	2.12	0.4	16.4	0.91
Tarf 33	2	0.31	31.2	0.99
Tarf 34	2.22	0.37	31.1	1.02
Tarf 35	2.16	0.43	23.1	0.92
Tarf 36	2.24	0.39	16.4	1.15
Tarf 37	1.17	0.19	18.9	1.75
Tarf 38	2.05	0.35	39.4	1.31
Tarf 39	1.99	0.41	20.5	1.58
Tarf 40	2.12	0.49	24.1	1.09
Tarf 41	2.37	0.51	20.4	0.74
Tarf 42	2.33	0.52	26.4	0.32
Tarf 45	2.28	0.47	19.2	0.47
Tarf 46	2.37	0.47	11.7	0.46
Tarf 47	2.16	0.39	19.2	1.08

continued next page

Table B.2: *continued*

sample name	H(S)	E	Average nannofossil density	NIP
Tarf48	2.3	0.45	20.3	0.82
Tarf 49	2.31	0.5	8.47	0.05
Tarf 50	2.32	0.51	16.9	0.33
Tarf 51	2.06	0.46	20.9	1.19
Tarf 56	2.26	0.5	10.2	1.22
Tarf 57	2.25	0.45	12.6	0.19
Tarf 58	2.29	0.52	15.9	-0.65
Tarf 59	2.35	0.58	10.6	-0.95
Tarf 60	2.44	0.61	8.97	-0.09
Tarf 61	2.34	0.52	13.4	0.17
Tarf 62	2.43	0.57	13.1	-0.19
Tarf 63	2.33	0.49	18.8	0.02
Tarf 64	1.79	0.3	34.3	0.52
Tarf 65	2.21	0.51	31.2	0.72
Tarf 66	2.26	0.53	27	0.91
Tarf 67	2.24	0.45	33.7	0.73
Tarf 68	2.38	0.51	31.8	0.30
Tarf 70	2.54	0.55	24.7	-0.30
Tarf 71	2.28	0.57	23.6	0.49
Tarf 72	1.82	0.34	18.3	1.15
Tarf 73	2.44	0.55	27.3	-0.02
Tarf 74	2.4	0.48	21.8	0.44

continued next page

Table B.2: *continued*

sample name	H(S)	E	Average nannofossil density	NIP
Tarf 75	1.91	0.38	34	0.78
Tarf 76	1.99	0.43	10.2	0.98
Tarf 77	2.36	0.48	27.1	0.40
Tarf 78	2.51	0.59	9.09	-0.01
Tarf 79	2.43	0.6	17.3	0.34
Tarf 80	2.39	0.6	12.8	-0.07
Tarf 81	2.44	0.6	13.6	0.26
Tarf 82	1.85	0.33	27.5	1.09
Tarf 83	1.82	0.34	14.1	1.41
Tarf 84	2.32	0.46	7.72	0.83
Tarf 85	2.33	0.47	18.3	0.12
Tarf 86	2.57	0.65	11.8	-0.30
Tarf 87	2.23	0.51	11.7	0.28
Tarf 88	2.31	0.53	21.4	-0.10
Tarf 89	2.47	0.54	16.4	0.10
Tarf 90	2.42	0.56	20.2	-0.06
Tarf 91	2.32	0.6	24.1	0.37
Tarf 92	2.26	0.48	24.9	0.40
Tarf 93	2.14	0.45	16.4	0.42
Tarf 94	2.47	0.54	18.8	0.25
Tarf 95	2.23	0.52	14.6	0.61

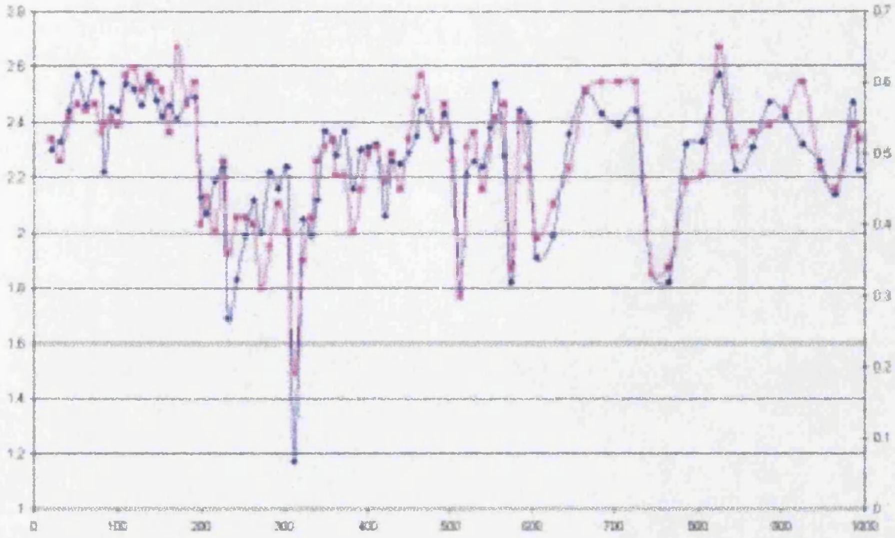

Figure B.1: Variation in the Shannon Weaver diversity index (H(S)) and Equatability (E) throughout the Tarfaya quarry core. Primary y axis - H(S) (blue), Secondary y axis - E (pink), x axis - depth/cm from top.

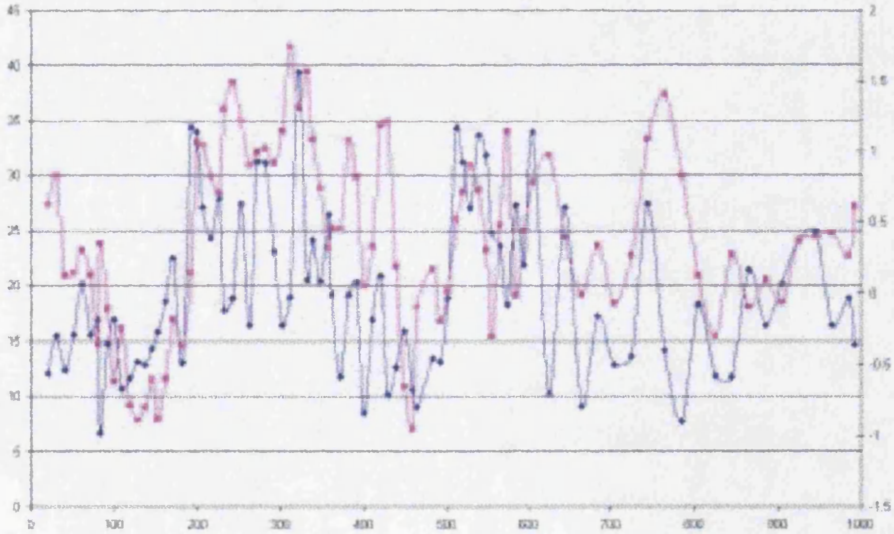

Figure B.2: Variation in Nannofossil index of productivity (NIP) and average nannofossil density throughout the Tarfaya quarry core. Primary y axis - average nannofossil density (blue), Secondary y axis - NIP (pink), x axis - depth/cm from top.

C

Appendix C - Rock images

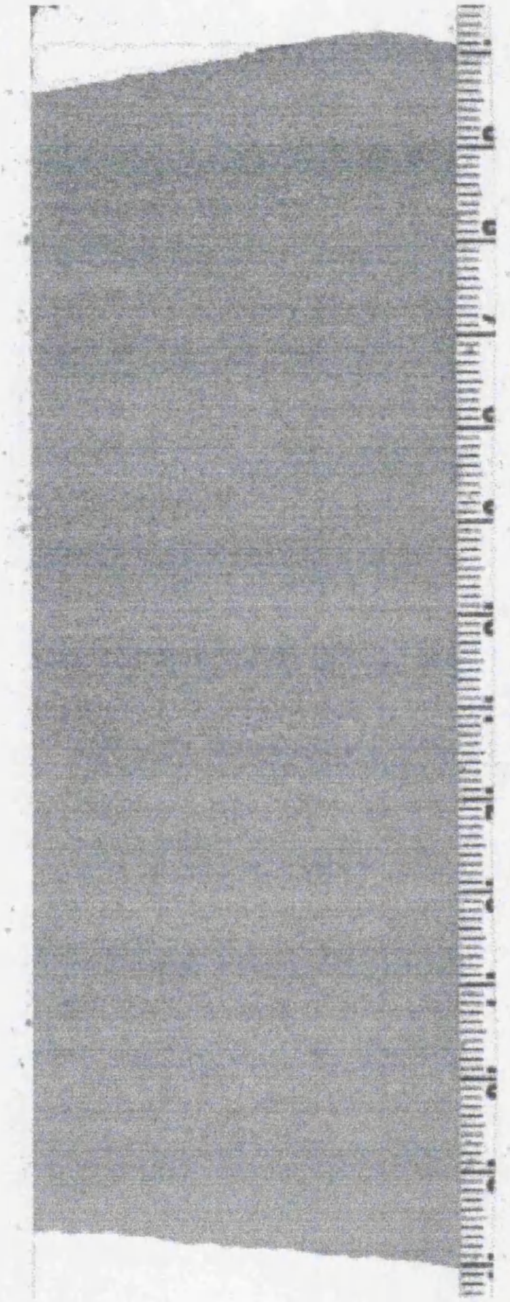

Figure C.1: Section 5C, mm scale along the edge

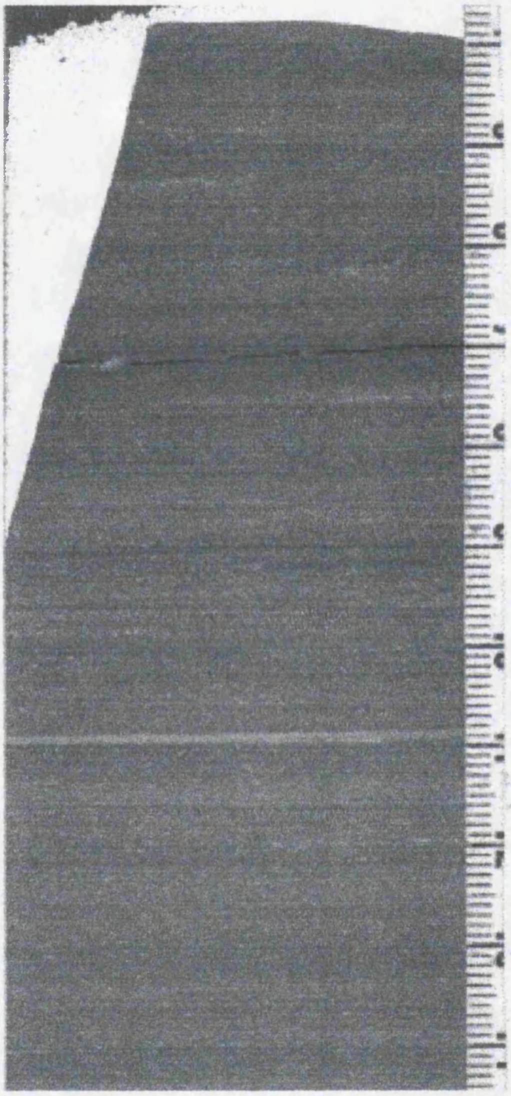

Figure C.2: Section 9A2/C, mm scale along the edge

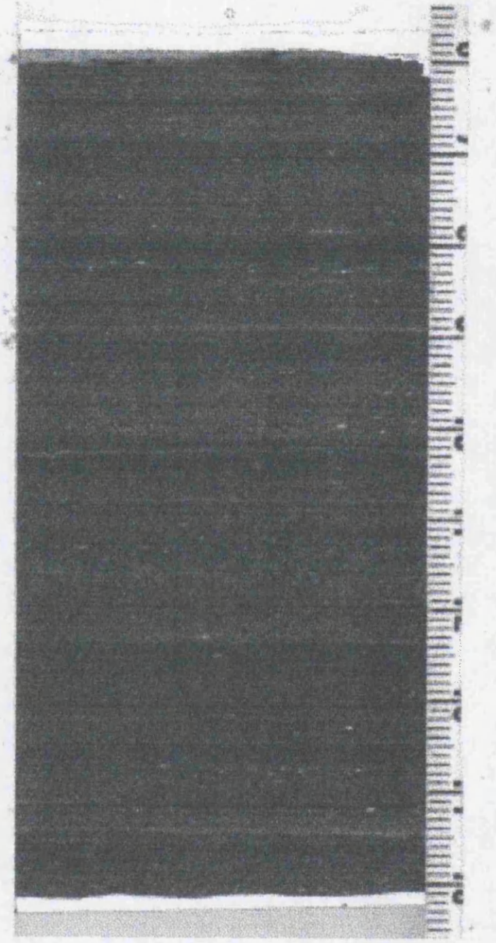

Figure C.3: Section 11F, mm scale along the edge

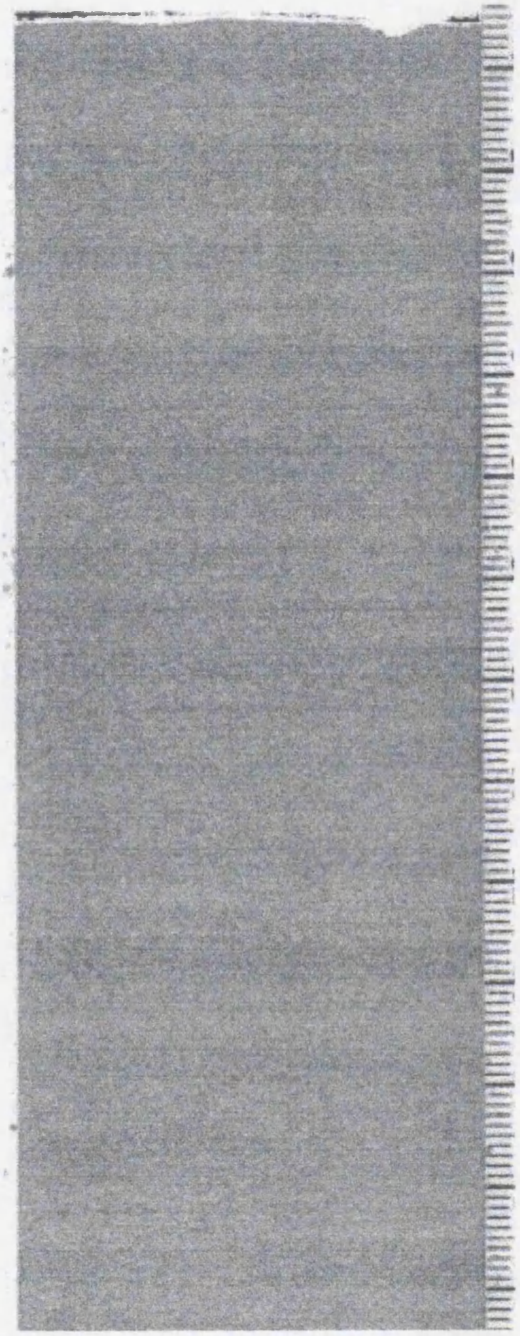

Figure C.4: Section 4C/D, mm scale along the edge

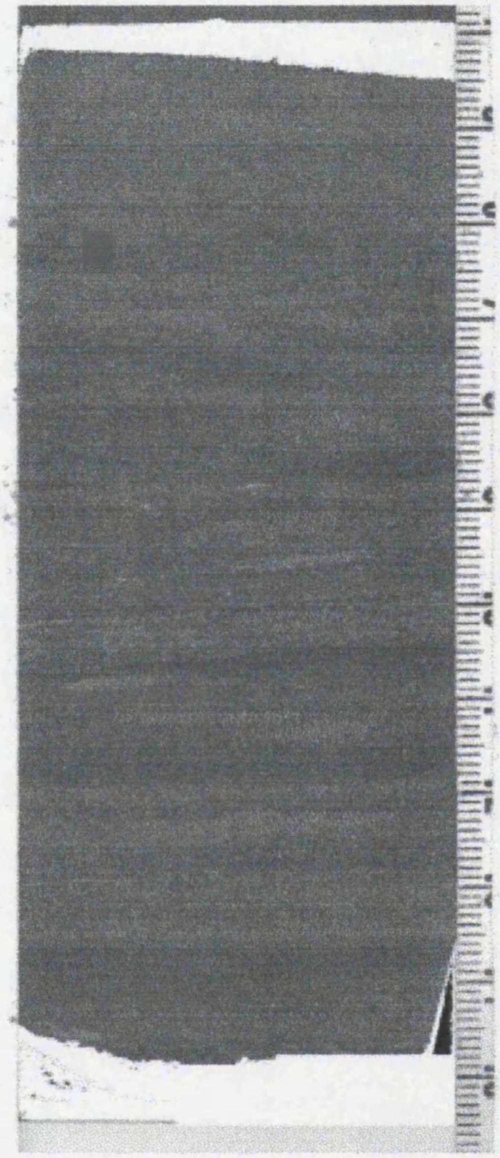

Figure C.5: Section 9D1/2, an example of a bioturbated area, mm scale along the edge

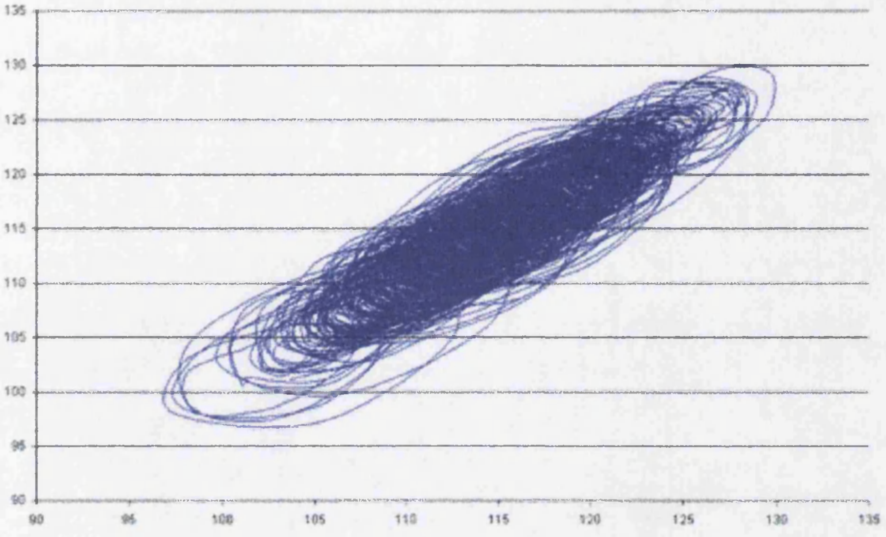

Figure C.6: Phase diagram of light sediment greyscale with one offset. Both axes are greyscale values with higher values being darker colours.

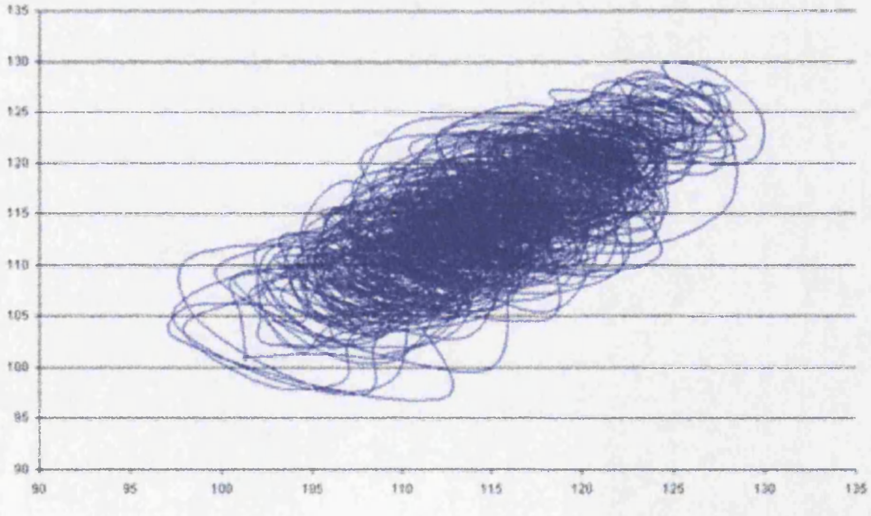

Figure C.7: Phase diagram of light sediment greyscale with two offsets. Both axes are greyscale values with higher values being darker colours.

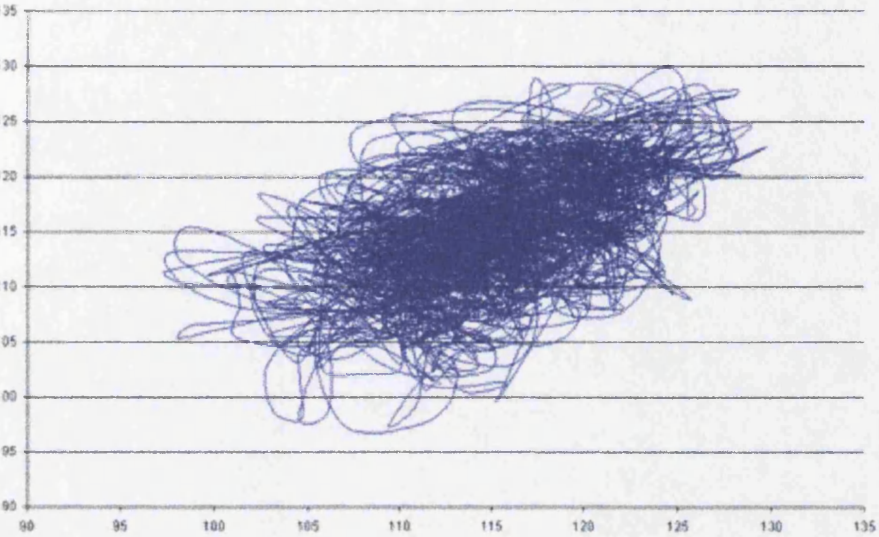

Figure C.8: Phase diagram of light sediment greyscale with ten offsets. Both axes are greyscale values with higher values being darker colours.

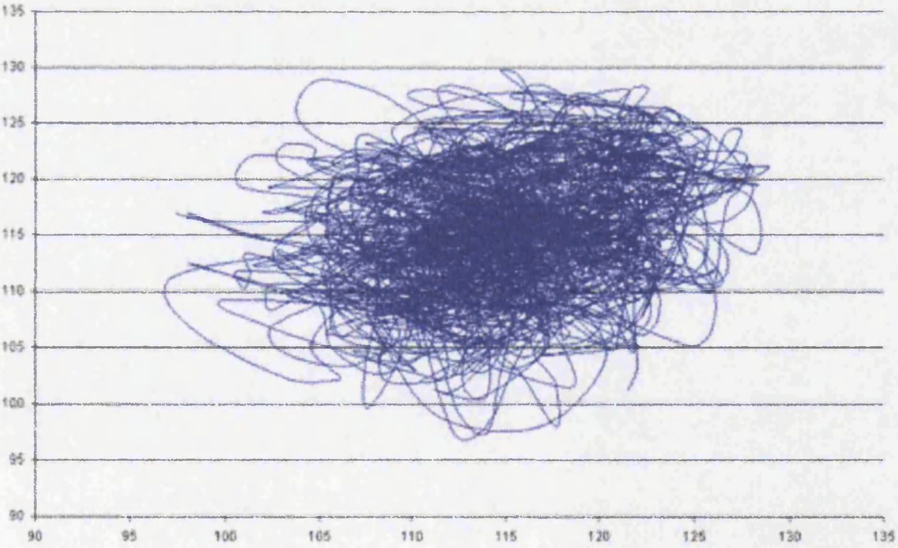

Figure C.9: Phase diagram of light sediment greyscale with one hundred offsets. Both axes are greyscale values with higher values being darker colours.

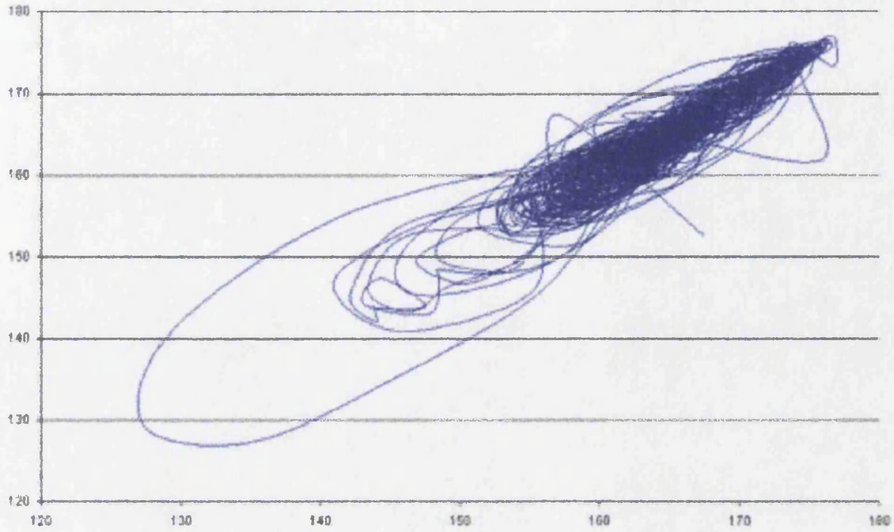

Figure C.10: Phase diagram of dark sediment greyscale with one offset. Both axes are greyscale values with higher values being darker colours.

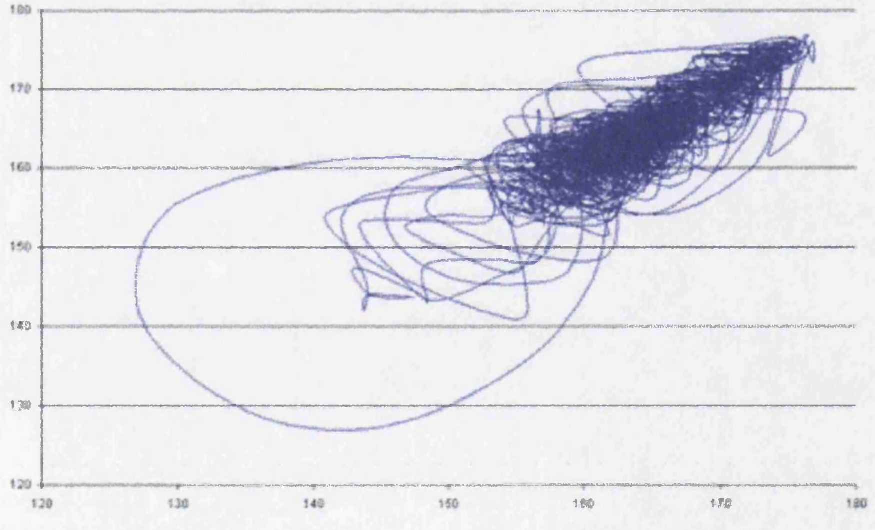

Figure C.11: Phase diagram of dark sediment greyscale with two offsets. Both axes are greyscale values with higher values being darker colours.

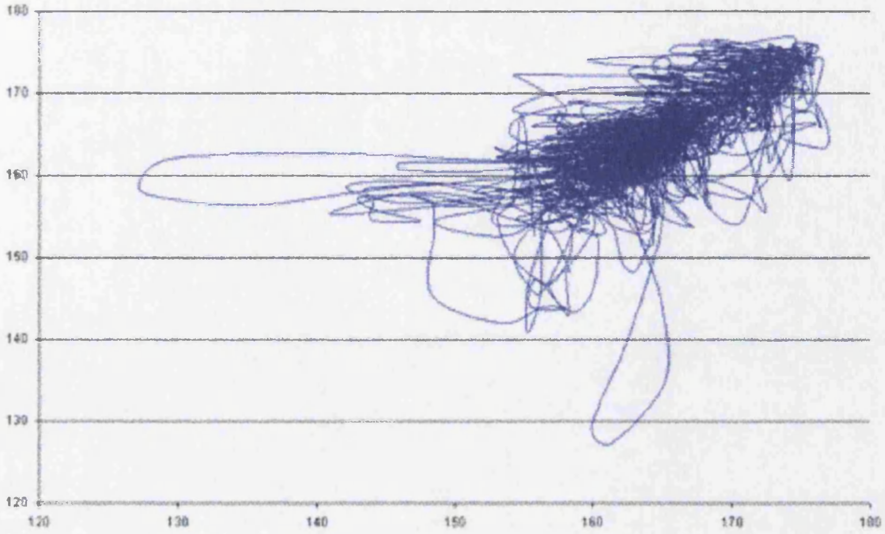

Figure C.12: Phase diagram of dark sediment greyscale with ten offsets. Both axes are greyscale values with higher values being darker colours.

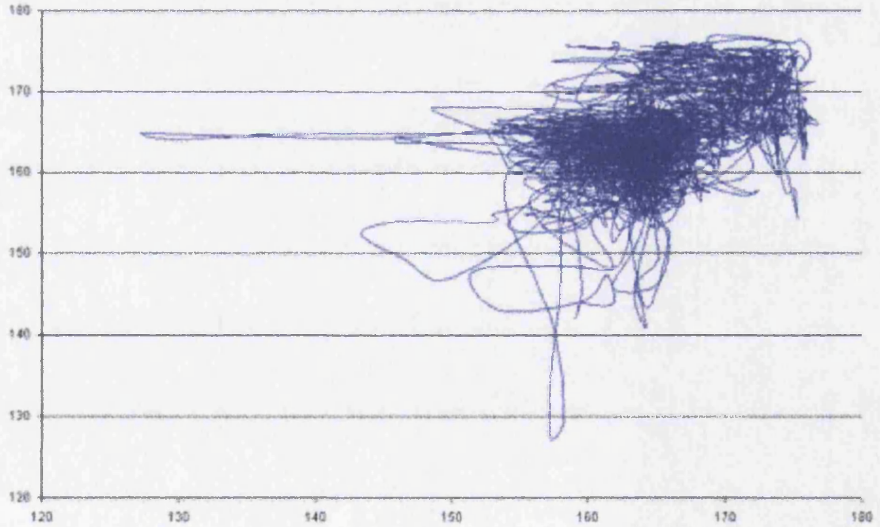

Figure C.13: Phase diagram of dark sediment greyscale with one hundred offsets. Both axes are greyscale values with higher values being darker colours.

Appendix D - MATLAB programmes

The MATLAB programs used on the Tarfaya data and referred to in section 5.4 are reproduced below. First is the program to calculate the periodogram of a time series and second is the program to plot a contour plot.

D.1 Periodogram programme

```
function v = pdg(x, len, DelT)
%v = pdg(x, len, DelT)
%Function to calculate the periodogram (unsmoothed
%variance spectrum) of a time series x(t)
%len is the length to be analyzed -- it can be equal to
%or less than the length of x (N), and it need not be a power of 2;
%or it can be the next power of 2 larger than N.
%DelT is the sampling interval
%Written by Gerry Middleton, November 1996 and adapted by Kate
%Ravilious October 2001.
N = length(x); N2 = floor(N/2); grey = x(:,2); mg = grey -
mean(grey); s2 = cov(x); g = 1 - exp((log(0.95) -
log(N2))/(N2-1));
```

```
%formula for 95% confidence interval
Yn = fft(mg, len);
%Fast Fourier Transform of the data
len2 = len/2; Pyy = (Yn).*conj(Yn)/(len*len); f =
(0:len2)/(len2*2*DelT);
%determination of variance (power) components
p = f'; A = [p, real(2*Pyy(1:len2+1))]; save fft.dat A -ascii
%saves data to a file
figure; plot(f,real(2*Pyy(1:len2+1)),'r'); title('Periodogram --
arithmetic variance scale'); xlabel(['Frequency per cm']);
ylabel('Variance'); hold on; plot([f(1) f(len2)], [2*s2*g
2*s2*g],':'); hold off;
%plots the periodogram
va = real(2*Pyy(2:len2-764)) ; ja = (f(2:len2-764)); ma = (va)';
vb = real(2*Pyy(260:len2+1)) ; jb = (f(260:len2+1)); mb = (vb)';
pa = polyfit(log(ja),log(ma), 1) ma = pa(1) ca = exp(pa(2)) da =
log(ca); ypa = ca*((ja).^ma); pb = polyfit(log(jb),log(mb), 1) mb
= pb(1) cb = exp(pb(2)) db = log(cb); ypb = cb*((jb).^mb);
%computes lines of best fit
figure; loglog(f(2:len2+1),real(2*Pyy(2:len2+1)),'r');
title('Periodogram -- logarithmic scale'); xlabel([' Frequency
per cm']); ylabel('Variance'); hold on; plot(ja,ypa,'b'); hold on;
plot(jb,ypb,'g'); hold off;
%plots a periodogram with a logarithmic scale and lines of best fit.
```

D.2 Contour plot programme

```
function [k] = congraph(x)
%plots a coloured contour plot
%Written by Kate Ravilious, November 2001.
colormap(hot); pcolor(x) shading flat title('Coloured contour plot
of Tarf1 to Tarf29'); xlabel(['File number, Tarf 1 to Tarf 29']);
ylabel('Frequency - see separate key for explanation');
```

D.3 Periodogram statistics

Table D.2: Table of gradients from the logarithmic periodograms of intervals of 8.7cm in length.

File name	average greyscale	ma	mb
mat1a	151.5	0.92	3.44
mat1b	151.4	0.92	4.27
mat1c	148.6	1.2	3.79
mat1d	146.8	1.01	3.99
mat2a	147	0.94	4.36
mat2b	143.8	1	3.87
mat2c	143.3	0.92	3.01
mat2d	141.6	0.97	2.82
mat3a	132.3	1.1	2.94
mat3b	143.8	0.84	3.73
mat3c	143	0.99	4.38
mat3d	132.9	0.78	3.99
mat4a	129.2	0.59	4.62
mat4b	125.7	0.81	4.12
mat4c	116.4	0.6	4.78
mat4d	117.4	0.65	4.49
mat5a	112.8	0.54	5.35
mat5b	115.9	0.8	5.1
mat5c	115.9	0.72	5.54
mat5d	117.7	0.93	5.46
mat6a	125.3	0.81	3.16
mat6b	135.9	0.84	3.54
mat6c	136.1	1.03	4.42
mat6d	133.5	1.06	3.98
mat7a	135.7	0.97	2.75

continued next page

Table D.2: *continued*

File name	average greyscale	ma	mb
mat7b	136	1.01	3.86
mat7c	139.9	0.92	4.66
mat7d	150.4	0.78	5.22
mat8a	150.8	0.6	4.44
mat8b	153.5	1.29	4.27
mat8c	147.5	1.07	3.81
mat8d	158.4	0.95	3.63
mat9a	154.3	0.87	3.41
mat9b	158.2	1.37	3.34
mat9c	167.2	1.37	2.7
mat9d	166.3	1.04	4.52
mat10a	164.3	1.14	3.43
mat10b	146.5	1.38	3.31
mat10c	153.8	1.07	3.19
mat10d	161.4	1.13	3.8
mat11a	143.3	0.9	3.71
mat11b	147.1	1	3.42
mat11c	143.9	1.14	3.5
mat11d	148.4	0.95	3.49
mat12a	138.4	1.16	3.84
mat12b	142.6	1.15	3.61
mat12c	136.2	0.8	4.37
mat12d	138.5	1.25	3.5
mat13a	143.8	0.75	3.51
mat13b	143	0.81	4.48
mat13c	131.8	0.96	3.85
mat13d	135.3	0.63	3.16
mat14a	140.3	0.76	4

continued next page

Table D.2: *continued*

File name	average greyscale	ma	mb
mat14b	129.1	0.9	3.9
mat14c	121.5	0.91	3.13
mat14d	131.1	1.09	3.15
mat15a	144	0.86	3.76
mat15b	130.3	1.08	3.66
mat15c	134.9	0.97	3.29
mat15d	129.3	1.06	3.21
mat16a	141.5	1.01	3.12
mat16b	126.6	1.03	4.7
mat16c	116	0.56	3.46
mat16d	126.9	0.7	4.17
mat17a	133.2	0.83	6.09
mat17b	135.7	0.95	4.51
mat17c	136.9	0.89	3.63
mat17d	133.6	1.2	3.73
mat18a	142.2	1.03	4.46
mat18b	146.8	0.75	4.56
mat18c	147.5	0.89	3.99
mat18d	145.1	0.97	3.98
mat19a	132.3	1.05	4.41
mat19b	142.2	0.98	4.22
mat19c	116.8	1.03	3.59
mat19d	115.4	0.58	4.1
mat20a	117.1	0.44	3.06
mat20b	106.9	0.89	2.91
mat20c	102.1	0.61	3.34
mat20d	92.3	0.82	3.38
mat21a	94.2	0.44	3.39

continued next page

Table D.2: *continued*

File name	average greyscale	ma	mb
mat21b	96.9	0.53	3.55
mat21c	89.6	0.79	4.16
mat21d	85.7	0.42	4.43
mat22a	95.9	0.88	4.19
mat22b	96.3	1.01	5.33
mat22c	110.9	1.09	3.84
mat22d	125	1.27	3.37
mat23a	128.1	1.06	3.39
mat23b	111.4	0.99	3.88
mat23c	130.5	1.35	3.27
mat23d	150.3	0.98	3.18
mat24a	153.1	0.92	3.45
mat24b	143.6	1.2	3.29
mat24c	133.8	1.32	4.39
mat24d	134.8	0.98	4.16
mat25a	124.5	1.04	5.42
mat25b	131.1	1.03	3.81
mat25c	135.3	1.1	3.52
mat25d	133.5	1.05	3.72
mat26a	118.5	0.94	2.79
mat26b	128.8	0.89	3.61
mat26c	118.7	1.1	3.91
mat26d	121.5	1.06	3.78
mat27a	127.1	0.94	2.76
mat27b	136.8	0.99	3.49
mat27c	136.5	1.05	3.62
mat27d	134.9	0.91	3.12
mat28a	142.1	0.92	3.18

continued next page

Table D.2: *continued*

File name	average greyscale	ma	mb
mat28b	152.2	0.87	2.86
mat28c	133.2	1.22	3.14
mat28d	101.9	0.85	3.41
mat29a	100.2	0.73	3.39
mat29b	99.4	0.64	5.13
mat29c	107	0.77	5.45
mat29d	130.3	1.09	3.25
mat30a	129.2	1.13	3.91

File name	average greyscale	ma	mb
Mat1	149.6	1.08	4.04
mat2	143.9	0.95	3.26
mat3	138	0.95	3.71
mat4	122.1	0.77	4.43
mat5	115.6	0.77	5.49
mat6	132.7	0.93	3.65
mat7	140.5	1.01	3.7
mat8	152.5	1.12	4.14
mat9	161.5	1.12	3.33
mat10	156.5	1.12	3.55
mat11	145.7	0.95	3.57
mat12	138.9	1.06	3.9
mat13	138.5	0.85	3.74
mat14	130.5	0.96	3.53
mat15	134.6	0.95	3.49
mat16	127.7	0.96	3.62
mat17	134.8	0.95	4.18
mat18	145.4	0.95	4.16
mat19	126.7	0.98	4.21
mat20	104.6	0.82	3.24
mat21	91.6	0.63	3.94
mat22	107	1.12	3.9
mat23	130	1.06	3.56
mat24	141.3	1.1	4.1
mat25	131.1	1.02	4.04
mat26	121.9	1	3.52
mat27	133.8	1.02	3.19
mat28	132.4	0.99	3.17
mat29	109.2	0.99	3.67

Table D.1: Table of gradients from the logarithmic periodograms of intervals of 34.7cm in length.

References

[1] F. Abrantes, H. Meggers, S. Nave, J. Bollmann, S. Palma, C. Sprengel, J. Henderiks, A. Spies, E. Salgueiro, T. Moita and S. Neuer, Deep Sea Research II, (in press)

[2] D. V. Agar, Proceedings of the Geologists Association, **85**, 23, (1974)

[3] D. M. Anderson, in *Upwelling in the Ocean Modern Processes and Ancient Records*, edited by C. P. Summerhayes, K. C. Emeis, M. V. Angel, R. L. Smith and B. Zeitzschel, John Wiley & Sons, (1995)

[4] H. Andruleit, Marine Micropaleontology, **31**, 45, (1997)

[5] M. A. Arthur, S. O. Schlanger and H. C. Jenkyns, in *Marine Petroleum Source Rocks*, edited by J. Brooks and A. J. Fleet, Geological Society Special Publication, **26**, 401, (1987)

[6] M. A. Arthur, W. E. Dean, L. M. Pratt, Nature, **335**, 714, (1988)

[7] J. Backman and N. J. Shackleton, Marine Micropaleontology, **8**, 141, (1983)

[8] R. J. Bailey, Terra Nova, **10**, 222, (1998)

[9] P. Bak, The Devil's Staircase, Physics Today, December, 38, (1986)

[10] E. J. Barron, Earth Science Reviews, **19**, 305, (1983)

[11] R. G. Barry and R. J. Chorley, Atmosphere, Weather and Climate, Methuen & Co Ltd, (1977)

[12] H. A. Bauch and J. P. Helmke, International Journal of Earth Sciences, **88(2)**, 325, (1999)

[13] K. H. Baumann, M. Cepek, and H. Kinkel, in *Use of proxies in Paleoceanography*, edited by G. Fischer and G. Wefer, Springer, (1999)

[14] G. Bearman, Ocean Chemistry and Deep Sea Sediments, Pergamon Press in association with The Open university, (1989)

[15] W. H. Berger, in *Chemical Oceanography*, **5**, edited by J. P. Riley and R. Chester, Academic Press, London, (1976)

[16] W. H. Berger, C. B. Lange, and A. Weinheimer, Geology, **25(7)**, 619, (1997)

[17] R. A. Berner, A. C. Lasaga and R. M. Garrels, American Journal of Science, **283**, 641, (1983)

[18] R. A. Berner, Nature, **358**, 114, (1992)

[19] P. Bertrand, G. Shimmield, P. Martinez, F. Grousset, F. Jorissen, M. Paterne, C. Pujòl, I. Bouloubassi, P. Buat Menard, J. P. Peypouquet, L. Beaufort, M. A. Sicre, E. Lallier-Verges, J. M. Foster, Y. Ternois, and the Other Participants of the Sedorqua Program, Marine Geology, **130**, 1, (1996)

[20] K. D. Bidle and F. Azam, Nature, **397**, 508, (1999)

[21] G. R. Bigg, The Oceans and Climate, Cambridge University Press, (1996)

[22] H. M. Bolli and I. Premoli-Silva, in *Initial Reports of DSDP 15*, edited by N. J. Edgar and J. B. Saunders, US Government Printing Office, Washington (1973)

[23] P. R. Bown, Calcareous Nannofossil Biostratigraphy, British Micropaleontology Society Series, Kluwer Academic, (1998)

[24] T. J. Bralower, Paleoceanography, **3(3)**, 275, (1988)

[25] T. J. Bralower and H. R. Thierstein, Geology, **12**, 614, (1984)

[26] M. D. Brasier, Microfossils, George Allen & Unwin (Publishers) Ltd., (1980)

[27] J. A. Burnett, in *Calcareous Nannofossil Biostratigraphy* edited by P. R. Bown, British Micropaleontology Society Series, Kluwer Academic, (1998)

[28] W. J. Burroughs, Weather Cycles, Real or Imaginary?, Cambridge University Press, (1994)

[29] D. E. Canfield, Deep Sea Research, **36**, 121, (1989)

[30] P. Cepek, Palaeogeography, Palaeoclimatology, Palaeoecology, **174**, 181, (2001)

[31] M. R. Chapman and N. J. Shackleton, Earth and Planetary Science Letters, **159**, 57, (1998)

[32] G. Choubert, A. Faure Muret and L. Hottinger, Notes Mem. Serv. Geol. Maroc, **175(1)**, 9, (1966)

[33] J. Q. Christensen and S. Björck, Journal of Paleolimnology, **25(4)**, 531, (2001)

[34] CLIMAP Project members, Science, **191**, 1131, (1976)

[35] M. C. Cooper, Journal of Paleolimnology, **19(1)**, 33, (1998)

[36] M. K. E. Cooper, in *Nannofossils and their applications*, edited by J. A. Crux and S. E. van Heck, Proceedings of the International Nannofossil Association Conference, London, (1987)

[37] C. Covey, Scientific American, **250**, 421, (1984)

[38] J. C. Davis, Statistics and Data Analysis in Geology, John Wiley & Sons, New York, (1986)

[39] J. M. Dean, A. E. S. Kemp and R. B. Pearce, Marine Geology, **174**, 139, (2001)

[40] G. J. Demaison and G. T. Moore, The American Association of Petroleum Geologists Bulletin, **64(8)**, 1179, (1980)

[41] J. M. Dennison, and W. W. Hay, Journal of Paleontology, **41(3)**, 706, (1967)

[42] G. Einsele and J. Wiedmann, in *Geology of the Northwest African Continental Margin*, edited by U. von Rad, K. Hinz, M. Samethein and E. Seibold, Springer-Verglag, Berlin, Heidelberg, New York, (1982)

[43] G. Einsele, W. Ricken and A. Seilacher, Cycles and Events in Stratigraphy, Springer-Verlag, (1991)

[44] A. El Albani, D. Vachard, W. Kuhnt and H. Chellai, Comptes Rendus de l'Academie des Sciences - Series IIA Earth and Planetary Science, **326(6)**, 397, (1999)

[45] E. Erba, D. Castradori, G. Guasti, and M. Ripepe, Palaeogeography, Palaeoclimatology, Palaeoecology, **93**, 47, (1992)

[46] J. Erbacher, B. T. Huber, R. D. Norris and M. Markey, Nature, **409**, 325, (2001)

[47] Y. Eshet, A. Almogi-Labin, and A. Bein, Marine Micropaleontology, **23**, 231, (1994)

[48] Y. Eshet and A. Almogi-Labin, Marine Micropaleontology, **29**, 37, (1996)

[49] R. F. File, Weather Facts, Oxford University Press, (1996)

[50] A. G. Fischer and L. T. Roberts, Journal of Sedimentary Petrology, **61(7)**, 1146, (1991)

[51] C. G. Fisher and W. W. Hay, Geological Society of America Special Paper, **332**, 161, (1999)

[52] J. A. Flores, in 4th International Conference of Paleoceanography, Kiel, Programs and Abstracts (1992)

[53] J. A. Flores, F. J. Sierro, G. Frances, A. Vazquez and I. Zamarreño, Marine Micropaleontology, **29**, 351, (1997)

[54] P. Francus, Sedimentary Geology, **121(3-4)**, 289, (1998)

[55] T. Freudenthal, H. Meggers, J. Henderiks, H. Kuhlmann, A. Moreno and G. Wefer, Deep Sea Research II, (in press)

[56] D. K. Fütterer, in *Coastal Upwelling*, edited by J. Thiede and E. Suess, Plenum Press, New York and London, (1983)

[57] A. S. Gale, J. R. Young, N. J. Shackleton, S. J. Crowhurst and D. S. Wray, in *Astronomical (Milankovitch) calibration of the geological time-scale*, Philosophical Transactions of the Royal Society, **357(1757)**, 1815, (1999)

[58] A. S. Gale, A. B. Smith, N. E. A. Monks, J. A. Young, A. Howard, D. S. Wray and J. M. Huggett, Journal of the Geological Society, **157**, 745, (2000)

[59] A. S. Gale, Workshop on Cretaceous Climate and Ocean Dynamics, July 14-17, Florissant, Colorado, USA, (2002)

[60] G. Gard, in *Nannofossils and their applications*, edited by J. A. Crux and S. E. van Heck, Proceedings of the International Nannofossil Association Conference, London, (1987)

[61] G. K. Gilbert, Journal of Geology, **3**, 121, (1895)

[62] F. Gradstein, F. P. Agterberg, J. G. Ogg, J. Hardenbol, P. van Veen, J. Thierry and Z. Huang, Journal of Geophysical Research, **99/B12**, 24051, (1994)

[63] F. Gradstein, F. P. Agterberg, J. G. Ogg, J. Hardenbol, P. van Veen, J. Thierry and Z. Huang, in *Geochronology, time scales and global stratigraphic correlation*, edited by W. A. Berggren, D. V. Kent, M. P. Aubry and J. Hardenbol, SEPM Special Publication **54**, 95, (1995)

[64] G. Grimmett and D. Welsh, Probability An Introduction, Oxford University Press, (1994)

[65] E. A. Hailwood, Geological Society of London Special Report, **19** (1989)

[66] W. W. Hay, R. DeConto, C. N. Wold, K. M. Wilson, S. Voigt, M. Schulz, A. Wold-ROssby, W. C. Dullo, A. B. Ronov, A. N. Balukhovsky and E. Soeding, Alternative Global Cretaceous Paleogeography in *The evolution of Cretaceous Ocean/Climate Systems*, edited by E. Barrera and C. Johnson, Geological Society of America Special Paper, **332**, 1, (1999)

[67] J. D. Hayes, J. Imbrie, and N. J. Shackleton, Science, **194**, 1121, (1976)

[68] J. Henderiks, T. Freudentahl, H. Meggers, S. Nave, F. Abrantes, J. Bollmann and H. R. Thierstein, Deep Sea Research II, (in press)

[69] S. M. Henrichs and W. S. Reeburgh, Geomicrobiological Journal, **5**, 191, (1987)

[70] , A. S. Henriksson, Cretaceous Research, **17**, 451, (1996)

[71] T. D. Herbert, in *Astronomical (Milankovitch) calibration of the geological time-scale*, Philosophical Transactions of the Royal Society, **357(1757)**, 1891, (1999)

[72] M. A. W. Heyman in *Extensional Tectonics and Stratigraphy of the North Atlantic Margins*, edited by A. J. Tankard and H. R. Balkwill, American Association of Petrolium Geologists Memoir, **46**, (1989)

[73] S. Honjo and H. Okada, Micropaleontology, **20(2)**, 209, (1974)

[74] B. T. Huber, R. D. Norris and K. G. MacLeod, Geology, **30(2)**, 123, (2002)

[75] L. Hutchings, G. C. Pitcher, T. A. Probyn, and G. W. Bailey, in *Upwelling in the Ocean Modern Processes and Ancient Records*, edited by C. P. Summerhayes, K. C. Emeis, M. V. Angel, R. L. Smith and B. Zeitzschel, John Wiley & Sons, (1995)

[76] J. Imbrie and K. Imbrie, Ice Ages: Solving the Mystery, Harvard University Press, Short Hills, (1979)

[77] R. A. Jahnke and G. B. Shimmield, in *Upwelling in the Ocean Modern Processes and Ancient Records*, edited by C. P. Summerhayes, K. C. Emeis, M. V. Angel, R. L. Smith and B. Zeitzschel, John Wiley & Sons, (1995)

[78] H. C. Jenkyns, Journal of the Geological Society of London, **137**, 171, (1980)

[79] H. C. Jenkyns, A. S. Gale and R. M. Corfield, Geology Magazine, **131**, 1, (1994)

[80] J. Johnson and I. Stevens, Deep Sea Research I, **47(5)**, 875, (2000)

[81] K. M. Johnson and K. A. Grimm, Marine Geology, **174**, 159, (2001)

[82] C. E. Jones and H. C. Jenkyns, American Journal of Science, **301(2)**, 112, (2001)

[83] K. Kaiho and S. Saito, Terra Nova, **6(4)**, 376, (1994)

[84] G. Keller, Q. Han, T. Adatte and S. J. Burns, Cretaceous Research, **22(4)**, 391, (2001)

[85] A. C. Kerr, Journal of the Geological Society, London, **155**, 619, (1998)

[86] S. D. Killops and V. J. Killops, An introduction to organic geochemistry, Longman Scientific and Technical, (1993)

[87] T. Kiorboe, C. Lundsgaard, M. Olesen, and J. L. S. Hansen, Journal of Marine Research, **52**, 297, (1994)

[88] P. C. Knutz, W. E. N. Austin and E. J. W. Jones, Paleoceanography, **16(1)**, 53, (2001)

[89] E. Kruijs and E. Barron, in *Deposition of organic facies* edited by A. Y. Huc, AAPG, Studies in Geology, **40**, 195, (1990)

[90] W. Kuhnt et al, Mitt. Geol.Palaont. Inst. Univ. Hamburg SCOPE/UNEP, **60**, 205, (1986)

[91] W. Kuhnt, J. P. Herbin, J. Thurow and J. Weidmann, in *Deposition of Organic Facies*, edited by A. Y. Huc, AAPG Studies in Geology, **30**, 133, (1990)

[92] W. Kuhnt, A. Nederbragt and L. Leine, Cretaceous Research, **18**, 587, (1997)

[93] W. Kuhnt, E. Chellai, A. Holbourn, F. Luderer, J. Thurow, T. Wagner, A. El Albani, B. Beckmann, J. Herbin, H. Kawamura, S. Kolonic, A. Nederbraght, C. Street, and K. Ravilious, EOS Transactions, American Geophysical Union, **82(33)**, 361, (2001)

[94] M. M. M. Kuypers, R. D. Pancost and J. S. S. Damste, Nature, **399(6734)**, 342, (1999)

[95] M. A. Lamolda, A. Gorostidi and C. R. C. Paul, Cretaceous Research, **15**, 143, (1994)

[96] M. A. Lamolda and S. Mao, Palaeogeography, Palaeoclimatology, Palaeoecology, **150**, 65, (1999)

[97] R. L. Larson, Geology, **19**, 963, (1991)

[98] R. M. Leckie, H. Sigurdsson, G. D. Acton and G. Draper (Eds), Proceedings of the ODP Scientific Results, 165: College Station, TX(Ocean Drilling Program), (2000)

[99] L. Leine, Geologie en Mijnbouw, **65**, 57, (1986)

[100] A. Leventer, E. W. Domack, S. E. Ishman, S. Brachfeld, C. E. McClennen and P. Manley, GSA Bulletin, **108(12)**, 1626, (1996)

[101] J. Lewis, J. D. Dodge and A. J. Powell, in *Proceedings of ODP Scientific Results* **112**, edited by E. R. Suess et. al., 323, (1990)

[102] G. Lindenberg and B. Ringberg, GFF, **121**, 182, (1999)

[103] G. Longo, B. D'Argenio, V. Ferreri and M. Iorio, Special Publications of the International Association of Sedimentologists, **19**, 77, (1994)

[104] F. Luderer and W. Kuhnt, Ann. Soc. Geol Nord, **5(3)**, 199, (1997)

[105] F. Luderer, Das Cenoman/Turon Grenzereignis im Tarfaya-Becken (SW Marokko), PhD Thesis, University of Kiel, (1999)

[106] K. G. MacLeod, B. T. Huber, T. Pletsch, U. Röhl, and M. Kucera, Paleoceanography, **16(2)**, 133, (2001)

[107] S. Manabe and K. Bryan, Journal of Geophysical Research - Oceans, **90(NC6)**, 1689, (1985)

[108] R. McIlveen, Fundamentals of Weather and Climate, Chapman and Hall, (1995)

[109] A. McIntyre, Science, **158**, 1314, (1967)

[110] M. R. McQuoid, M/ J. Whitcar, S. E. Calvert and T. F. Pedersen, Marine Geology, **174**, 273, (2001)

[111] G. V. Middleton, Nonlinear Dynamics, Chaos and Fractals, with Applications to Geological Systems, Geologists Association of Canada, Short Course notes 9, (1991)

[112] G. V. Middleton, Data Analysis in the Earth Sciences, using MATLAB, Prentice-Hall, (2000)

[113] M. Milankovitch, Kanon der Erdbestahlung und seine Anwendung auf das Eiszeitproblem, **133** Akad. R. Serbe, (1941)

[114] B. Molfino and A. McIntyre, Science, **249(4970)**, 766, (1990)

[115] S. Moshkovitz, A. Ehrlich and D. Soudri, Cretaceous Research, **4**, 173, (1983)

[116] T. Mullin, The nature of Chaos, Oxford Science Publications, (1993)

[117] J. Mutterlose in *Nannofossils and their applications*, edited by J. A. Crux and S. E. van Heck, Proceedings of the International Nannofossil Association Conference, London, (1987)

[118] A. J. Nederbragt, R. N. Erlich, B. W. Fouke and G. M. Ganssen, Palaeogeography, Palaeoclimatology, Palaeoecology, **144**, 115, (1998)

[119] A. J. Nederbragt and J. W. Thurow, Marine Geology, **174(1)**, 95, (2001)

[120] A. Negri, Paleopelagos, **3**, 305, (1993)

[121] R. D. Norris and P. A. Wilson, Geology, **26(9)**, 823, (1998)

[122] R. D. Norris, K. L. Bice, E. A. Magno and P. A. Wilson, Geology, **30(4)**, 299, (2002)

[123] L. Nykjaer and L. Van Camp, Journal of Geophysical Research, **99(C7)**, 14197, (1994)

[124] J. D. Obradovich in *Evolution of the Western Interior Basin*, edited by W. G. E. Caldwell, Geological Association of Canada, Special Paper **39**, 379, (1993)

[125] http://www.odsn.de/odsn/services/paleomap

[126] P. E. Olsen and D. V. Kent, in *Astronomical (Milankovitch) calibration of the geological time-scale*, Philosophical Transactions of the Royal Society, **357(1757)**, 1761, (1999)

[127] G. Parilla, S. Neuer, P. Y. Le Traon and E. Fernandez, Deep Sea Research II, (in press)

[128] C. R. C. Paul, M. A. Lamolda, S. F. Mitchell, M. R. Vaziri, A. Gorostidi, and J. D. Marshall, Palaeogeography, Palaeoclimatology, Palaeoecology, **150**, 83, (1999)

[129] T. F. Pedersen and S. E. Calvert, The American Association of Petroleum Geologists Bulletin, **74(4)**, 454, (1990)

[130] J. D. Pelletier, Earth and Planetary Science Letters, **158**, 157, (1998)

[131] G. Petterson, B. V. Odgaard and I. Renberg, Journal of Paleolimnology, **22(4)**, 443, (1999)

[132] J. Pike and A. E. S. Kemp, Paleoceanography, **12(2)**, 227, (1997)

[133] C. H. Pilskaln, and J. Pike, Paleoceanography, **16(1)**, 1, (2001)

[134] C. J. Poulsen, E. J. Barron, M. A. Arthur and W. H. Peterson, Paleoceanography, **16(6)**, 576, (2001)

[135] A. J. Powell, J. D. Dodge and J. Lewis, in *Proceedings of ODP Scientific Results* **112**, edited by E. R. Suess et. al., 297, (1990)

[136] I. Premoli Silva, E. Erba, G. Salvini, C. Locatelli and D. Verga, Journal of Foraminiferal Research, **29(4)**, 352, (1999)

[137] U. Ranke, U. vonRad, and G. Wissmann, in *Geology of the Northwest African Continental Margin*, edited by U. von Rad, K. Hinz, M. Samethein and E. Seibold, Springer-Verglag, Berlin, Heidelberg, New York, (1982)

[138] D. Rind, Quaternary Science Reviews, **14**, 381, (2000)

[139] D. Rind, J. Lerner and C. McLinden, Journal of Geophysical Research - Atmospheres, **106(D22)**, 28061, (2001)

[140] D. Rio, I. Raffi and G. Villa, Proceedings of the Ocean Drilling Program Scientific Results, **107**, 513, (1990)

[141] M. Ripepe, L. T. Roberts and A. G. Fischer, Journal of Sedimentary Petrology, **61(7)**, 1155, (1991)

[142] H. J. Röhl, A. Schmid-Röhl, W. Oschmann, A. Frimmel, and L. Schwark, Palaeogeography, Palaeoclimatology, Palaeoecology, **165**, 27, (2001)

[143] E. A. Romankervich, Geochemistry of Organic Matter in the Ocean, Springer Verlag Berlin, (1984)

[144] D. A. Ross, Introduction to Oceanography, Harper Collins College Publishers, (1995)

[145] P. H. Roth, in Initial Reports of the Deep Sea Drilling Project, **17**, U.S. Government Printing Office, Washington D.C., 695, (1973)

[146] P. H. Roth, in *Initial Reports of the Deep Sea Drilling Project* **75**, edited by W. W. Hay et. al., U.S. Government Printing Office, Washington D.C. 651, (1984)

[147] P. H. Roth and J. L. Bowdler, in Tulsa, Society of Economic Paleontologist and Mineralogists, Special Publication **32**, 517, (1981)

[148] P. H. Roth and K. R. Krumbach, Marine Micropaleontology, **10**, 235, (1986)

[149] P. H. Roth and H. R. Thierstein, in Initial Reports of the Deep Sea Drilling Project, **24**, U.S. Government Printing Office, Washington, D.C., 421 (1972)

[150] W. F. Ruddiman and A. McIntyre, in *Investigation of Late Quaternary Paleoceanography and Paleoclimatology*, Geological Society of America Memoir, **145**, edited by R. M. Cline and J. D. Hays (1976)

[151] D. B. Ryves, S. Juggins, S. C. Fritz and R. W. Battarbee, Palaeogeography, Palaeoclimatology, Palaeoecology, **172**, 99, (2001)

[152] C. Samtleben and A. Schröder Marine Micropaleontology, **19**, 333, (1992)

[153] M. Sarnthein, J. Thiede, U. Pflaumann, H. Erlenkeuser, D. Fütterer, B. Koopmann, H. Lange and E. Seibold in *Geology of the Northwest African Continental Margin*, edited by U. von Rad, K. Hinz, M. Samethein and E. Seibold, Springer-Verglag, Berlin, Heidelberg, New York, (1982)

[154] A. A. Scarparo Cunha and E. A. M. Koutsoukos, Palaeogeography, Palaeoclimatology, Palaeoecology, **142**, 175, (1998)

[155] M. Schaaf and J. Thurow, Sedimentary Geology, **94(1-2)**, 1, (1994)

[156] M. Schaaf, PhD Thesis, University of Bochum, Germany, (1995)

[157] M. Schaaf and J. Thurow, Journal of the Geological Society, **154**, 613, (1997)

[158] S. O. Schlanger and H. C. Jenkyns, Geologie en Mijnbouw, **55**, 179, (1976)

[159] W. Schwarzacher, Special Publications of the International Association of Sedimentologists, **19**, 87, (1994)

[160] W. Schwarzacher, Earth Science Reviews, **50**, 51, (2000)

[161] C. T. Scrutton, Palaeontology, **7**, 552, (1964)

[162] N. J. Shackleton and N. D. Opdyke, Quaternary Research, **3**, 39, (1973)

[163] N. J. Shackleton, S. J. Crowhurst, G. P. Weedon and J. Laskar in *Astronomical (Milankovitch) calibration of the geological time-scale*, Philosophical Transactions of the Royal Society, **357(1757)**, 1907, (1999)

[164] C. E. Shannon and W. Weaver, The Mathematical Theory of Communication, University of Illinois Press, Urbana, (1949)

[165] D. G. Smith, Special Publications International Association of Sedimentologist, **19**, 531, (1994)

[166] R. L. Smith, in *Upwelling in the Ocean Modern Processes and Ancient Records*, edited by C. P. Summerhayes, K. C. Emeis, M. V. Angel, R. L. Smith and B. Zeitzschel, John Wiley & Sons, (1995)

[167] C. Sprengel, K. H. Baumann and S. Neuer, marine Micropaleontology, **39**, 157, (2000)

[168] C. Sprengel, K. H. Baumann, J. Henderiks, R. Henrich and S. Neuer, Deep Sea Research II, (in press)

[169] R. Stein, Accumulation of Organic Carbon in Marine Sediments, Lecture Notes in Earth Sciences, **34**, Springer-Verlag, (1991)

[170] C. Street and P. R. Bown, Marine Micropaleontology, **39 (1-4)**, 265, (2000)

[171] M. A. Storms, Marine Geophysical Researches, **12**, 109, (1990)

[172] E. Suess, Nature, **288**, 260, (1980)

[173] C. P. Summerhayes, in *Coastal Upwelling*, edited by J. Thiede and E. Suess, Plenum Press, New York and London, (1983)

[174] C. P. Summerhayes, D. Kroon, A. Rosell-Mele, R. W. Jordan, H. J. Schrader, R. Hearn, J. Villanueva, J. O. Grimalt and G. Eglinton, Prog. Oceanog, **35**, 207, (1995)

[175] H. R. Thierstein, Marine Micropaleontology, **1**, 325, (1976)

[176] H. R. Thierstein, in Tulsa, Society of Economic Paleontologist and Mineralogists, Special Publication **32**, 335, (1981)

[177] E. Thomsen, Geology, **17**, 715, (1989)

[178] E. Thomsen, Marine Micropaleontology, **15**, 123, (1989)

[179] M. E. Torres-Padron, M. D. Gelado-Caballero, C. Collado-Sanchez, V. F. Siruela-Matos, P. J. Cardona-Castellano and J. J. Hernandez-Brito, Deep Sea Research II, (in press)

[180] R. V. Tyson, Sedimentary Organic Matter, Organic facies and palynofacies, Chapman & Hall, (1995)

[181] L. Van Camp, L. Nykjaer, E. Mittelstaedt and P. Schlittenhardt, Progress in Oceanography, **26**, 357, (1991)

[182] O. Varol, Newsletters on Stratigraphy, **27(3)**, 93, (1992)

[183] E. L.a Venrick, Ecological Monographs, **52(2)**, 129, (1982)

[184] C. Viotti, Notes Mem. Serv. Geol. Maroc, **175(1)**, 225, (1966)

[185] U. von Rad, K. Hinz, M. Sarnthein and E. Seibold, Geology of the Northwest African Continental Margin, Springer-Verlag, (1982)

[186] P. Wassmann, J. E. Ypma, A. Tselepides, Progress in Oceanography, **46**, 241, (2000)

[187] D. K. Watkins, Palaegeography, Palaeoclimatology, Palaeoceology, **74**, 75, (1989)

[188] P. P. E. Weaver and P. J. Schultheiss, Marine Geophysical Researches, **12**, 85, (1990)

[189] G. P. Weedon, Journal of the Geological Society, **146**, 133, (1989)

[190] G. P. Weedon and H. C. Jenkins, Journal of the Geological Society London, **147**, 915, (1990)

[191] G. P. Weedon, H. C. Jenkyns, A. L. Coe and S. P. Hesselbo in *Astronomical (Milankovitch) calibration of the geological time-scale*, Philosophical Transactions of the Royal Society, **357(1757)**, 1787, (1999)

[192] J. W. Wells, Nature, **197**, 948, (1962)

[193] J. Wiedmann, A. Butt, and G. Einsele, in *Geology of the Northwest African Continental Margin*, edited by U. von Rad, K. Hinz, M. Samethein and E. Seibold, Springer-Verglag, Berlin, Heidelberg, New York, (1982)

[194] P. A. Wilson and R. D. Norris, Nature, **412**, 425, (2001)

[195] P. A. Wilson, R. D. Norris and M. J. Cooper, Geology, **30(7)**, 607, (2002)

[196] A. Winter and W. G. Siesser, Coccolithophores, Cambridge University Press, (1994)

[197] J. R. Young, in *Functions of Coccoliths*, edited by A. Winter and W. G. Siesser, Cambridge Academic Press, Cambridge, (1994)